We are pleased to inform you that the Co-Editor report for the following manuscript is now available:

Journal: ACP
Title: Dynamics and composition of the Asian summer monsoon anticyclone
Author(s): Klaus-Dirk Gottschaldt et al.
MS No.: acp-2017-420
MS Type: Research article
Iteration: Minor Revision
Special Issue: The Modular Earth Submodel System (MESSy) (ACP/GMD inter-journal SI)

The Co-Editor has decided that minor revisions are necessary before the manuscript can be accepted. Please find the Co-Editor Report at https://editor.copernicus.org/ACP/ms_records/acp-2017-420.

We kindly ask you to revise your manuscript accordingly and to upload the revised files, a point-by-point reply to the comments, and a marked-up manuscript version showing the changes made in your File Manager no later than 17 Feb 2018: https://editor.copernicus.org/ACP/file_manager/acp-2017-420. Please find all information on manuscript submission under https://www.atmospheric-chemistry-and-physics.net/for_authors/submit_your_manuscript.html.

Your revised manuscript will be reviewed by the Co-Editor and you will be informed about the outcome by separate email.

Besides adjustments requested by the Co-Editor or Referees, please check your manuscript carefully for typos, missing co-authors and their affiliations, terminology, updates of data in tables, or updates of variables in equations. All these have to be clarified with the Co-Editor and therefore have to be included before you submit your revised manuscript. Should your manuscript be finally accepted it will not be possible to include such rather substantial changes anymore when your manuscript is in final production (proofreading).

Co-Editor Decision: Publish subject to minor revisions (review by editor) (07 Feb 2018) by Marc von Hobe
Comments to the Author:
Generally, the structure of the main text is quite good. The storyline through the sections and subsections appears logical, the main findings are nicely summarized in Section 7, and some lengthy "side excursions" have been removed.

We thank the Co-Editor for his review and helpful comments. Our changes to the manuscript are highlighted in the markup version, with color coding according to Fig. 1. Please note that newly inserted references and modified figure numbers are not always highlighted (for technical reasons). Table 1 summarizes the renumbering of figures instead. Changes to citations are noted in our responses to your comments below.

However, the paper is still moving on the edge of being "information overload", especially with the large amount of cross referencing to the Appendices and Supplement. Some of this extra material is important and well justified, but in some cases, I'm not sure if it is really necessary and if the placement in an Appendix/Supplement is the correct choice. Please consider the following specific remarks and suggestions in that respect:

Appendix A: from the title of the Appendix, this is not different from Section 6.1, and some of the extra discussion of processing inside the ASMA could be blended into that Section in the main text. But much of the material, such as the comparison to CARIBIC and Satellite observations and the model sensitivity studies seem more appropriate in the supplement (some of the figures are

already there, e.g. Figure S10) to convince those readers who have doubts about the model lighting NOx.

Done.

Appendix B: I think this could be shortened a bit and added to the main text. Figures B1 and B3 can be added to Figures 4 and 3, and the discussion added to Sections 4, 5 and 6, maybe by adding subsections. I don't see that NOy is so much less important than the other material discussed in the main text, and I don't think it will disrupt the main text too much. You mention all tracer-tracer relations in the first sentence of Section 4.1 and state that some are shown in that Section and others in the Appendix. But a reasoning why the NOx relations are not discussed in the main text is not given.

Done.

Appendix C: does this "primer" contain any information that is not available in the literature? I don't think it is really needed and suggest referring to one or a few papers (or even books) where tracer relations are introduced in some detail.

We found no basic text-book description, just applications of the method in papers. Moved to the supplement and added two references.

With respect to the supplementary figures, some of them are referred to and discussed in the main text in just the same way as normal figures (e.g. page 11, line 26, page 15, line 20, and quite a few others), and I don't see any harm including some of them in the main part of the paper. Extra figures typically don't disrupt the story line, and there is not an official limit with respect to the number of Figures in a paper. I'm thinking that especially Figures S1, S11 and S16 would be nice to have in the main part of the paper: they are very interesting and highly relevant and do not just provide extra documentation and reproducibility.

We agree. Figures S1, S11 and S16 are now part of the main text.

For the multi-year information, data comparisons and model sensitivities, these are indeed appropriately placed in the supplement if you do want to show all of them. Maybe you can add a bit of discussion in the actual supplement, e.g. move some of the material from Appendix A into the supplement, so it becomes a little more independent and rounds up all "extra topics". In fact, you may want to consider giving the supplement a bit of structure, e.g. model comparison to satellite data, inter-annual variability, process sensitivities in the model. In that case, the referencing in the main text to this "extra material" becomes much clearer.

This is a good idea, the supplement is structured now.

Besides considering the suggested rearrangements into main text and supplements, the following technical corrections need to be made prior to final publication:

The in-text referencing of the figures is not in the correct order (e.g. Figure 2 should be referred to earlier than Figure 7). In particular, Figures discussed in detail later are referred to in quite random order in Section 3. Please either renumber your figures, or adjust the text so that the referring is in the correct order.

The order of figures was intended to reflect the storyline. Now they are ordered according to first referral in the text (Table 1).

On the same note, Section 5 discusses in detail what is seen in Figure 4, but the subsections 5.1 to 5.4 correspond to e/f, c/d, a/b and g/h respectively. I suggest changing the order of the gases

shown in the Figure according to the Section ordering, i.e. O3 on top, then CO, then HCl and then NOx.

Done.

Page 6, line 4: I don't understand the word "enhanced" here. If you refer to the vertical gradients in O3 itself, then please delete "Enhanced". If you mean something else, then please explain.

Reformulated.

Page 6, lines 13 and 16: please add some literature references that HCl is a good tracer for stratospheric O3 entrainments and that daytime NO is a good proxy for NOx.

HCl: The reference to Marcy et al. (2004) was intended for the whole sentence, but placing it at the end might indeed be misleading. We moved the reference to Marcy et al. to the first part of the sentence and added the reference to Park et al (2008), who used HCl as stratospheric tracer in the ASMA.

NOx: We restricted the statement to the UT, where daytime NO/NO2 is about 12 (Seinfeld & Pandis, 2006).

Page 9, line 20: the circled area looks more like 300 to 500 hPa below the TP rather than 200 to 300 hPa. Please check this and correct or clarify!

Corrected.

Page 13, line 14: should be ("2" in Fig. 6) instead of ("2" in Fig. 4)

Corrected.

Caption Figure 3: it should be (b,e) and (c/f) in lines 4 and 6

Corrected.

Caption Figure 4: please remove the #+ in front of the Figure numbering

Done, also in the footnote on page 12.

Caption Figure 6, line 9: between 200 and 700 ppb NOx seems incredibly high. Please check and correct this!

Corrected to pmol mol^{-1}. We also changed "mol/mol" to "mol mol^{-1}" throughout.

old	**new**	**old**	**new**	**old**	**new**	**old**	**new**
1	2	A1	10	S2	S4	S10	S2
2	4	A2	S3	S3	S5	S11	11
3	8	A3	S12	S4	S6	S12	S14
4abcdef 4gh	5efcdab 6ab	A4	S13	S5	S7	S13	S15
5	7	B1abcd	6cdef	S6	S8	S14	S10
6	12	B2	S11	S7	S9	S15	S17
7	3	B3	9	S8	S16	S16	13
8	14	S1	1	S9	S1	S17	S18

Table 1: Figure numbering; old = manuscript version 20171222, new = 20180221

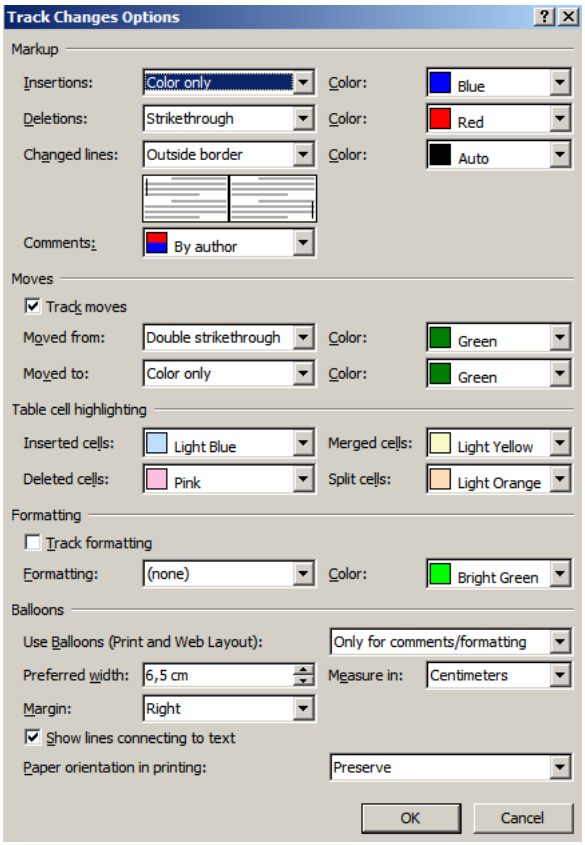

Figure 1: Markup for changes in the manuscript.

Dynamics and composition of the Asian summer monsoon anticyclone

Klaus-D. Gottschaldt[1], Hans Schlager[1], Robert Baumann[1], Duy S. Cai[1], Veronika Eyring[1], Phoebe Graf[1], Volker Grewe[1,2], Patrick Jöckel[1], Tina Jurkat-Witschas[1], Christiane Voigt[1,3], Andreas Zahn[4] and Helmut Ziereis[1]

[1]Deutsches Zentrum für Luft- und Raumfahrt (DLR), Institut für Physik der Atmosphäre, Oberpfaffenhofen, Germany
[2]Delft University of Technology, Aerospace Engineering, Delft, The Netherlands
[3]Johannes Gutenberg-Universität, Institut für Physik der Atmosphäre, Mainz, Germany
[4]Karlsruher Institut für Technologie (KIT), Institut für Meteorologie und Klimaforschung, Karlsruhe, Germany

Correspondence to: Klaus-D. Gottschaldt (klaus-dirk.gottschaldt@dlr.de)

Abstract. This study places HALO research aircraft observations in the upper-tropospheric Asian summer monsoon anticyclone (ASMA) obtained during the Earth System Model Validation (ESMVal) campaign in September 2012 into the context of regional, intra-annual variability by hindcasts with the ECHAM/MESSy Atmospheric Chemistry (EMAC) model. Observed and simulated tracer-tracer relations reflect photochemical O_3 production, as well as in-mixing from the lower troposphere and the tropopause layer. The simulations demonstrate that tropospheric trace gas profiles in the monsoon season are distinct from the rest of the year, and the measurements reflect the main processes acting throughout the monsoon season. Net photochemical O_3 production is significantly enhanced in the ASMA, where uplifted precursors meet increased NO_x, mainly produced by lightning. An analysis of multiple monsoon seasons in the simulation shows that stratospherically influenced tropopause layer air is regularly entrained at the eastern ASMA flank, and then transported in the southern fringe around the interior region. Radial transport barriers of the circulation are effectively overcome by subseasonal dynamical instabilities of the anticyclone, which occur quite frequently, and are of paramount importance for the trace gas composition of the ASMA. Both, the isentropic entrainment of O_3-rich air and the photochemical conversion of uplifted O_3-poor air tend to increase O_3 in the ASMA outflow.

1 Introduction

The Asian monsoon system is one of the largest and dominating atmospheric features on Earth. It is stronger than other monsoon systems because of the topography of the region, which insulates warm, moist air over South Asia from the cold and dry extratropics (Boos and Kuang, 2010). This leads to a global maximum of surface moist static energy at the south-western flank of the Himalayas (Boos and Hurley, 2013), which drives deep convective updrafts during northern hemispheric summer. Elevated surface heating over the Tibetan plateau (Flohn, 1960; Fu et al., 2006), predominantly northward surface winds plus orographic uplifting at the southern/southwestern slopes of the Himalayas (Li et al., 2005; Liu

et al., 2009b), and deep convection over the Bay of Bengal (Park et al., 2009; Nützel et al., 2016) - all additionally contribute to an overall ascending air current. This drives an anticyclonic circulation, centred at 200 to 100 hPa (Dunkerton, 1995; Randel and Park, 2006; Garny and Randel, 2015).

Location, shape and strength of the ASMA strongly vary on intra-seasonal, inter-annual and longer timescales (Dunkerton, 1995; Lin et al., 2008; Kunze et al., 2010; Pokhrel et al., 2012), which is subject to ongoing discussion (Pan et al., 2016; Nützel et al., 2016). An elliptical vortex is intrinsically unstable (Hsu and Plumb, 2001; Popovic and Plumb, 2001), thus prone to splitting up and eddy shedding to the west and east (Dethof et al., 1999; Vogel et al., 2014). Variable forcing by convection (Randel and Park, 2006; Garny and Randel, 2013), sub-seasonal oscillations (Lin et al., 2008; Goswami, 2012), the interaction with Rossby waves or mid-latitude synoptic disturbances (Dethof et al., 1999) add further complexity. The overall upwelling in the eastern ASM region is accompanied by large-scale subsidence in the western part (Rodwell and Hoskins, 1996), making the Arabian Peninsula one of the warmest and driest regions on Earth. The heat low associated with the hot desert conditions in summer supports itself an anticyclone (Lelieveld et al., 2009), which interacts with the ASMA.

The interplay of the above dynamical ingredients makes the Asian summer monsoon a switch yard and mixing vessel for air masses of different origin and with different composition, including the exchange between troposphere and stratosphere. Monsoon air is received by regions around the globe (Rauthe-Schöch et al., 2016), and was for instance shown to affect the tropospheric chemical composition in the Mediterranean (Lelieveld et al., 2001; Lelieveld et al., 2002; Scheeren et al., 2003). A mid-tropospheric (400-500 hPa) summertime O_3 maximum over the eastern Mediterranean / Middle East region (Li et al., 2001; Lelieveld et al., 2009; Schuck et al., 2010; Akritidis et al., 2016) is enhanced by Asian monsoon outflow (Liu et al., 2009b; Richards et al., 2013; Barret et al., 2016)., but it is not clear, if O_3 in the ASMA plume is generally enhanced or depleted (Lawrence and Lelieveld, 2010).

In the following “TL” refers to the mixing zone at the tropopause, where cross-tropopause exchange of air masses on average creates a gradient between stratospheric to tropospheric trace gas signatures. The TL is also denoted ExTL in the extratropics and TTL in the tropics, reflecting that the dominating physical processes change at about the 30° circles of latitude. There are no rigid boundaries, but rather stratospheric influence decreases towards the troposphere over a range of several kilometres (Gettelman et al., 2011). In contrast, “upper troposphere” (UT) is used here to describe the altitude region that is dominated by the ASMA. Despite its importance for redistributing trace gases between boundary layer, troposphere and lower stratosphere, the highly variable composition of the ASMA and the processes behind it are not well understood yet (Randel et al., 2016).

In situ measurements were conducted in the ASMA during the ESMVal field experiment with the High Altitude and LOng Range (HALO) research aircraft in September 2012. A sudden enhancement of measured O_3 when HALO entered the ASMA from the south triggered the accompanying paper (Gottschaldt et al., 2017), since those measurements contrast the presumption of decreased O_3 in the ASMA. It was shown that the ASMA filament(s) encountered during that flight were associated with entrainments of lower-/mid-tropospheric air at the eastern ASMA flank, as well as with stratospherically influenced TL air.

Here we put the specific situation observed during the HALO ESMVal campaign into a regional, seasonal and multi-annual perspective, which is provided by global chemistry climate simulations with the EMAC model.

Recent papers discussed climatological trace gas distributions in the monsoon region (Santee et al., 2017), CO distributions in the context of daily ASMA dynamics (Pan et al., 2016), and monthly budgets of CO and O_3 (Barret et al., 2016). Building on the ASMA observations during the HALO-ESMVal campaign, the second objective of our study is to complement these papers by considering additional tracers on a 10-hourly scale to characterise key processes relevant for the O_3 distribution in the monsoon region.

We first briefly summarize the data used here, then discuss the EMAC-simulated intra-annual variability of selected tracers in the ASMA region for the year of the HALO ESMVal campaign, put observed tracer-tracer relations in the context of simulated ones, discuss the interplay of the processes that contributed to the observed trace gas signatures, and also show in the context of multiple monsoon seasons that the specific situation observed during the HALO ESMVal campaign was not exceptional. For brevity the main text provides only summarizing statements about lightning NO_x ($LiNO_x$) and reactive nitrogen (NO_y) in the ASMA, and we refer to two appendices for details. Additional figures in the supplement are provided for documentation and reproducibility.

2 Data

We focus on the analyses of O_3, CO, hydrogen chloride (HCl) and reactive nitrogen (NO, NO_x, NO_y), as those tracers reflect the processes most relevant for the interpretation of in situ measurements in the ASMA during the ESMVal flight from Male (Maldives) to Larnaca (Cyprus) on 18 September 2012. All in situ measurements used here are based on a data set with 10 s time resolution, which is available from the HALO database (https://halo-db.pa.op.dlr.de). The corresponding measurement techniques are described in the accompanying paper, and in more detail in publications about the individual instruments: CO (Hoor et al., 2004; Schiller et al., 2008; Müller et al., 2016), HCl (Jurkat et al., 2014; Voigt et al., 2014), NO/NO_y (Ziereis et al., 2000), O_3 (Zahn et al., 2012). Among those tracers, only HCl mixing ratios were at the instrument's detection limit during the considered flight (Jurkat et al., 2016).

The transport pathways of air parcels before being encountered by HALO were calculated with the Lagrangian HYSPLIT model (Draxler and Hess, 1998; Draxler and Rolph, 2015). Although published in the accompanying paper, those analyses are a basis for this study.

In the following all simulation data stem from global chemistry climate simulations with the EMAC model (Jöckel et al., 2010), performed within the ESCiMo (Earth System Chemistry integrated Modelling) project (Jöckel et al., 2016) and the DLR-internal ESMVal project. Our reference simulation has been described and generally evaluated as RC1SD-base-10a by Jöckel et al. (2016). Its set-up is designed for best possible comparability to observations by nudging of the dynamics to ECMWF ERA-Interim (Dee et al., 2011) reanalysis data and covers the period 1980 – 2013 (excluding spin-up). Convection is not resolved in the simulation, but its effects are captured by a parameterisation in EMAC. $LiNO_x$ emissions are

parameterized on top of the convection parameterization. Given the above uncertainties, simulated lightning activity compares acceptably to satellite observations (Supplement~~Appendix A~~).

NO_x background mixing ratios are crucial for O_3 photochemistry, as will be discussed in more detail in section 6.3. In ~~-~~situ measurements are the most accurate in the UT. We have shown in the accompanying paper that this simulation reproduces the measured trace gas mixing ratios along the HALO flight track of 18 September 2012 reasonably well, but this comparison is rather limited spatially and temporally. Therefore we compare simulated NO and NO_y to one of the most comprehensive observational datasets available for reactive nitrogen in the UT (Stratmann et al., 2016): IAGOS-CARIBIC (In-service Aircraft for a Global Observing System - Civil Aircraft for the Regular Investigation of the atmosphere Based on an Instrument Container; Brenninkmeijer et al. (2007), www.caribic-atmospheric.com). Our comparisons are based on the output of the EMAC S4D submodel (Jöckel et al., 2010), i.e. along the given IAGOS-CARIBIC flight tracks each model time step (Δt = 12 min). The agreement between simulated NO and corresponding IAGOS-CARIBIC observations is remarkable, particularly in the ASMA region (Appendix B). Further comparisons between the EMAC RC1SD-base-10a simulation and IAGOS-CARIBIC are shown by Jöckel et al. (2016) for O_3, CO and others, based on 10-hourly simulation output.

Ten-year averages of simulated O_3 reproduce the low-O_3 ASMA interior of satellite climatologies (Santee et al., 2017), as well as increased O_3 found by HALO ESMVal at slightly lower potential temperatures (~~supplement, Fig.~~ Fig. 1).

Additional EMAC simulations were performed in quasi chemistry transport model mode (Deckert et al., 2011; Gottschaldt et al., 2013) to test the impact of $LiNO_x$. Those are described in the supplement~~Appendix A and referred to always by their acronyms~~. "Simulation" without further specification refers to RC1SD-base-10a in the following.

3 The ASMA region

As noted in the introduction, the ASMA is driven by a large scale updraft originating from the south-western flank of the Himalayas on the one ~~hand,~~hand and by smaller scale tropical deep convection events on the other hand. The latter correlates with a maximum of Outgoing Longwave Radiation (OLR), which expands from the Bay of Bengal towards the Tibetan plateau and back in the course of a monsoon season (Nützel et al., 2016). In contrast, the large scale updraft is tied to geographical features (maximum of moist static energy in the Indo-Gangeatic plain, heating of the Tibetan plateau, orographic forcing of the Himalayas). The inland thermodynamic conditions of the Arabian Peninsula support the mid tropospheric anticyclone in the west. It may intermittently merge with the ASMA, but we presume that the composition of the UT in the west is determined mainly by the air transported in the eastern-driven circulation. We denote the western and eastern parts "Iranian" and "Tibetan", respectively. "ASMA" unspecifically refers to the whole system.

The regions' delimitations (Fig. 2) for separate analyses of the different parts were chosen by eye, considering the following: (i) For putting the measurements into perspective, the regions shall capture the synoptic situation during the HALO ESMVal

campaign; (ii) Both parts shall be equally sized; (iii) The variability of the ASMA's location and extent shall be covered. The chosen meridional range of 15°N to 35°N covers the simulated ASMA ridgeline for most of the monsoon season (shown in Fig. 3b). The zonal ranges are 30°E to 65°E and 65°E to 100°E for Iranian and Tibetan regions, respectively. For comparison, Yan et al. (2011) classified anticyclonic centres between 50°E and 67.5°E as Iranian mode, and between 80°E and 92.5°E as Tibetan mode.

We decided not to adapt the regions dynamically to the actual ASMA, because the boundary definitions we are aware of (Ploeger et al., 2015; Barret et al., 2016; Pan et al., 2016) emphasise the concept of a closed ASMA volume or transport barriers on monthly or seasonal timescales. However, the ASMA boundaries are not always well defined, particularly during transitions between different dynamical modes. Our pre-fixed regions allow an unbiased view on the effects of complex, 10-hourly dynamics. This comes at the price that features from outside the ASMA might contribute to the analyses occasionally. We can not rule out that concurrent but geographically distinct features feign correlations between different species, but monsoon-related features should mostly dominate the lateral averages in the chosen regions. Our approach detects differences between Iranian and Tibetan parts, because the corresponding circulation is tied to geographical features of the respective regions. Enhanced CO is considered to be a chemical characteristic of the ASMA (Pan et al., 2016), and increased geopotential height (GPH) is a dynamical proxy (Barret et al., 2016). Simulated seasonal mean distributions of both proxies indicate that our regions well capture the ASMA of 2012 (Fig. 2).

Large scale transport occurs mainly on isentropes, unlike convective transport. Pressure and isentropic vertical coordinates are similar in the UTLS in the tropics of the Tibetan region (Fig. 4a). In the EMAC simulation the TP has been diagnosed by a potential vorticity of 3.5 PVU in the extratropics and by the WMO definition between 30°N and 30°S (Jöckel et al., 2006). It is almost parallel to one isentrope in the tropics and to a lower one in the extratropics, but intersects isentropes around 360 K almost perpendicularly in the transition region at about 30°N. This facilitates isentropic inmixing from the lower stratosphere or the TL, but only in combination with southward wind components. If winds follow the TP (e.g. subtropical jet), it is still a transport barrier. The latter aspect is relevant for stratosphere-to-troposphere trace gas gradients and captured by coordinates relative to the TP (used for Figs. 5, 6, 7). The barrier effect of the TP is also relevant for convective transport (TP following coordinates also used for Fig. 7). Isentropic coordinates account for the seasonal evolution of potential temperature (θ, Fig. 4b), and best capture isentropic transport (used for Fig. 3, but also for the supplementary 5-year-equivalents to Figs. 5, 6, 7).

4 Tracer-tracer relations in September 2012

The distribution of points in a tracer-tracer diagram provides hints on the origin and evolution of air masses. A short primer for the interpretation of such diagrams is provided in the supplementary material~~Appendix C~~.

4.1 Selected tracers

Here we focus on CO versus O_3 and HCl versus O_3 (Fig. 8), ~~while~~ as well as on NO_x versus O_3 and NO_x versus ~~NO_y~~ NO_y ~~are shown in Appendix B~~ (Fig. 9).

~~Enhanced~~ O_3 mixing ratios in the TL exhibit a strong vertical gradient, increasing from the troposphere to the stratosphere. Given a chemical lifetime in the order of weeks, this reflects the degree of mixing between O_3-poor UT air and O_3-rich air from the lowermost stratosphere (Sprung and Zahn, 2010). That general picture might not hold in the ASMA though, where –depending on the availability of precursors- enhanced photochemical O_3 production is superimposed on isentropic inmixing from the stratosphere.

Enhanced CO is a tracer of boundary layer pollution and an O_3 precursor in the troposphere. Oxidation with the hydroxyl radical (OH) prevails under stratospheric conditions, and CO mixing ratios decrease by about an order of magnitude across the tropopause (Hoor et al., 2002).

As tracer for stratospheric air we use HCl (Marcy et al., 2004; Park et al., 2008), which in the UT has no significant photochemical sources and a lifetime similar to O_3–. Wet scavenging in clouds effectively prevents convective transport of HCl to the UT, and no injections of HCl from volcanic activity affected the ESMVal flight from Male to Larnaca. Together this makes HCl a viable tracer of stratospheric O_3 entrainments, until it is selectively removed by wet scavenging.

NO_x (NO + NO_2) is an O_3 precursor and part of NO_y ~~(see Appendix B for details)~~. NO_x primarily characterises fresh emissions. Only NO was measured during the HALO ESMVal campaign, but daytime NO is a good proxy for NO_x in the UT (Seinfeld and Pandis, 2006). In the UTLS, enhanced NO_y originates both from tropospheric and from stratospheric sources. Thus it is not a viable tracer for stratospheric air on its own. In the lower troposphere odd nitrogen species are co-emitted with carbon monoxide in combustion processes, lightning and aircraft emissions are sources in the UT. Photolysis of N_2O peaks at about 30 km and is the principal source of NO_x in the stratosphere, resulting in increasing mixing ratios of NO_x and NO_y above the TP (Seinfeld and Pandis, 2006).

4.2 Ranges covered by observed and simulated tracer-tracer distributions

In order to place the observed tracer-tracer relations into context, we plot the measured samples together with grid-cell samples from the EMAC simulation. Simulation output along the flight track is too sparse for a meaningful comparison (10 s resolution of measurements versus 12 min for the simulation). Therefore 5000 simulated samples per panel are chosen randomly, from the entire month of September 2012 and from throughout the ASMA region (Fig. 2: Tibetan plus Iranian parts). Plotting all corresponding samples form the EMAC simulation would impair the visibility of clustering. Two different vertical ranges are chosen. The range from 50 hPa above to 100 hPa below the actual EMAC tropopause (Figs. 8ad) provides a zoom-out view of possible tropospheric and stratospheric tracer mixing ratios and tracer-tracer relations for the time of year and region of the measurements. Zooming-in to the altitude range of measurements, we choose tropospheric tracers

from the pressure altitude range 200 hPa to 100 hPa (Figs. 8be). The observations from the entire flight without ascend and descent are shown in (Figs. 8cf).

Measurements south of the ASMA are marked by dark blue dots in Figs. 8cf and are clearly distinct from the measurements in the ASMA filament (orange boxes). The ranges covered by the measurements are also given in the corresponding panels with simulated data, but are adjusted for model biases there. Those biases were estimated according to comparisons by eye, of measured versus simulated trace gas mixing ratios along the flight track in the ASMA filament (shown in the accompanying paper). All measured ranges fit into the simulated monthly averages for September 2012 in the ASMA region, thus the simulation captures this aspect well and the measurements are unlikely to represent an exceptional situation. We also note that all measurements clearly fall into the tropospheric regions of the respective simulated tracer-tracer spaces. This is no surprise: all HALO ESMVal measurements considered here were taken well within the troposphere.

Simulated O_3 and NO_x increase in the stratosphere with a higher O_3/NO_x ratio than in the troposphere (Fig. 9a). However, since the range covered by the HALO ESMVal measurements is just at the intersection of stratospheric and tropospheric branch (orange box in Fig. 9a), this does not help distinguishing stratospheric influence from tropospheric in situ production.

4.3 In situ photochemistry, tropospheric and TL contributions

The colour code of the observations (Figs. 8cf) corresponds to measurement time. Similar colours indicate spatial and temporal proximity, a prerequisite for mixing lines. Schematic lines L1-L5 (Figs. 8be) and their parallels indicate special, hypothetical cases for the evolution of air masses, which are discussed next.

CO versus O_3 (Figs. 8abc): O_3 and CO display opposite gradients across the tropopause, and globally have lifetimes of several months in the UT (IPCC, 2013). Thus mixing lines in a CO versus O_3 scatter plot are generally suited to identify stirring and mixing processes in the UT that occur on timescales of days to weeks, including cross-tropopause mixing (Fischer et al., 2000). The well known L-shape (Hoor et al., 2002; Pan et al., 2004; Müller et al., 2016) is reproduced by the simulation in the CO vs. O_3 diagram for the UTLS (Fig. 8a), consisting of a CO-poor & O_3-rich stratospheric branch, connected by UTLS mixing lines to a CO-rich & O_3-poor tropospheric branch.

However, the above studies (Hoor et al., 2002; Pan et al., 2004; Müller et al., 2016) focused on the extratropics. The ASMA is mostly situated in the tropics, where trace gas mixing ratios are controlled by different processes (Gettelman et al., 2011). The ASMA in particular constitutes a special atmospheric situation, because a continuous resupply of rapidly uplifted lower tropospheric air impedes UT photochemical equilibrium there. O_3 is photochemically produced in the ASMA at a net rate of almost 4 nmol ~~/~~mol^{-1} ~~/~~day^{-1} (Barret et al. (2016); and Fig. 7b, which will be discussed in section 6). Only 2 weeks are needed to increase O_3 mixing ratios by 50 nmol ~~/~~mol^{-1}, i.e. to produce the O_3 enhancement observed at the southern ASMA edge. This is not much longer than the advection timescale (~10 days) discussed in the context of the HALO ESMVal campaign. Thus photochemical production needs to be considered as an alternative to stratospheric in-mixing for explaining enhanced O_3 in the ASMA. Photochemical ageing increases O_3 and depletes CO here.

Mixing lines with negative slopes in CO vs. O_3 space dominate the UT observations (black dotted in Fig. 8c). Such mixing lines in the troposphere could result from one or a combination of the following: (i) mixing between stratospherically and tropospherically influenced air masses; (ii) mixing between photochemically aged and freshly uplifted lower tropospheric air; (iii) an O_3 depleting photochemical regime (Baker et al., 2011). While the latter is unlikely in the ASMA (Fig. 7b), we need to consider additional tracers to disentangle stratospheric influence and photochemical ageing.

HCl versus O_3 (Figs. 8def): HCl is a proxy for stratospheric entrainment and CO marks tropospheric influence. Consider the hypothetical case of constant HCl (lines L1 and parallels in Figs. 8be): increasing O_3 corresponds to increasing CO then. The trace gas gradients along that hypothetical line reflect a gradient in net O_3 production rather than differences with respect to stratospheric influence between two reservoirs. Now consider the opposite case, i.e. constant CO (lines L2): increasing O_3 corresponds to increasing HCl, indicating a gradient of stratospheric influence. CO mixing ratios decrease for increasing HCl in the special case of constant O_3 and different HCl mixing ratios (lines L3). This indicates mixing between a tropospheric and a stratospheric reservoir, where two opposite effects lead to almost constant O_3 mixing ratios: increased net O_3 production in air with decreased HCl, versus both increased O_3 and HCl in the more stratospheric components. In intermediate cases the trace gas gradients in the tracer-tracer plots reflect a combination of gradients of in-mixing as well as in situ photochemistry. Spatial gradients of photochemical O_3 production dominate over gradients of stratospheric influence (i.e. in-mixing from the TL or stratosphere) within the sampled air mass, if increasing O_3 correlates with increasing CO and decreasing HCl (lines L4). In contrast, gradients of stratospheric or TL in-mixing dominate, if increasing O_3 correlates with increasing HCl and decreasing CO (lines L5).

The measurements (Figs. 8cf) mostly – but not exclusively - show the latter case (L5): neighbouring points form negatively sloped lines in CO vs. O_3 space (black dotted in Fig. 8c), corresponding to horizontal to positively sloped lines in HCl vs. O_3 space (black dotted lines in Fig. 8f). Thus, observed trace gas gradients are mostly due to gradients of stratospheric influence on some well mixed UT background. This could either be entrainment of tropospheric air into a more stratospheric background, or entrainment of TL air into a more tropospheric background. There are also a few almost vertical mixing lines in Fig. 8f, indicating case L3 described above. Systematic HCl gradients – like across the tropopause - are not expected in convectively uplifted air. O_3 variability in such air masses is at least partly due to different amounts of in situ produced O_3. However, mixing between aged and young tropospheric air alone cannot explain the observations.

We further note that mixing lines in Fig. 8f cover similar ranges of HCl, but are separated by different levels of O_3. The corresponding background air had seen similar amounts of stratospheric influence, but different O_3 production. As long as all points of an individual mixing line are subject to similar O_3 production, the entire line will be shifted to different O_3 levels. The O_3 ranges covered by individual mixing lines are similar to the offsets between different lines. Individual mixing lines in the measurements cover timescales of about 20 minutes (Fig. 8c), corresponding to 300 km at typical HALO speeds. The flight track in the ASMA filament altogether covers more than 3000 km and multiple mixing lines were found on that scale.

Summarizing, our observations of O_3, HCl and CO in an ASMA filament show that: (i) Both, photochemical production and TL/stratospheric in-mixing contribute to increased O_3 in the observed ASMA filament; (ii) small-scale gradients of stratospheric influence are superimposed on background regions that are rather homogeneous on small scales (hundreds of kilometres), but differ in their amounts of photochemically produced O_3 on larger scales (thousands of kilometres).

NO_x versus O_3 (Figs. 9abc): Similar HCl mixing ratios are simulated throughout the ranges of measured NO_x and O_3 (orange box in Fig. 9b). Measurements of increased NO_x in combination with increased O_3 (upper right corner of the orange boxes in Fig. 9) are compatible with both, increased in situ O_3 production and influence from the stratospheric branch. Consequently, NOx and O_3 are well correlated on the scale of our ASMA measurements (Fig. 9c).

NO_x versus NO_y (Figs. 9def): There are three distinct regions in Fig. 9d: a blueish stratospheric branch, a dark TL branch, and a reddish UT region. As a consequence of the local NO_y minimum directly above the tropopause (Fig. 6d; examples of individual profiles in the supplement), the most decreased NO_y mixing ratios in Fig. 9d also show up in samples taken from near the tropopause. Measured NO and NO_y values in the ASMA filament are well correlated (Fig. 9f), which is consistent with almost constant NO_x/NO_y ratios in the UT (Figs. 6ef). The narrow, linear distribution of the ASMA measurements in Figs. 9cf can be explained by different amounts of lightning NO_x of approximately the same age.

5 Simulated intra-annual variability of trace gas dynamics in the monsoon region

In this section we discuss the evolution of simulated trace gas profiles throughout the year 2012, separately for lateral averages over the western (Iranian) and eastern (Tibetan) ASMA regions (Fig. 2).

5.1 Ozone

Steep vertical gradients across the tropopause dominate O_3 profiles in the monsoon regions (Figs. 5ab), but the profiles also show temporal fluctuations of various timescales. Note that our lateral averaging regions are rather large and smaller-scale structures get smoothed out, e.g. when an O_3-poor interior is combined with an O_3-rich fringe.

There is increased influx from the stratosphere in spring, enhancing O_3 in the UT. This is in accordance with the study of Cristofanelli et al. (2010), but in contrast to their study there are non-negligible O_3 enhancements connected to the stratosphere during the monsoon season (Fig. 5b, circled). In this respect our simulation is however consistent with trace gas budget considerations for the ASMA (Barret et al., 2016) and the TTL (Konopka et al., 2010). Entrainment from the TL rather than deep from the stratosphere could reconcile the different findings. No other stratospheric contributions were found for the stratospherically influenced trace gas signatures in the HALO ESMVal ASMA observations.

Enhanced O_3 prints through in the averaged profiles of the eastern ASMA part only from the tropopause to about 200 hPa below the tropopause, while the mid-troposphere in the Tibetan part is dominated by particularly O_3 poor air during the monsoon season (Fig. 5b). The latter is consistent with the findings of Safieddine et al. (2016). O_3 depletion in the mid-troposphere of the eastern part is contrasted by enhanced O_3 in the mid-troposphere during the monsoon season in the western part (Fig. 5a, circled), marking the well known summertime O_3 maximum there.

5.2 Carbon monoxide

This is reflected in the evolution of CO profiles in the ASMA region in 2012 (Figs. 5cd). CO-poor air dominates in the UT during spring, consistent with the stratospheric influx indicated by O_3.

CO-rich air rises throughout the troposphere of the eastern part during the monsoon season (Fig. 5d, circled). On the western side there is a conspicuous CO depleted zone ~~2~~300 to ~~3~~500 hPa below the tropopause during the monsoon season (Fig. 5c, circled), while CO is episodically enhanced in the UT. Uplifted air with enhanced CO mixing ratios hardly reaches higher than to 450 hPa below the tropopause in summer.

This difference between CO profiles in the Tibetan and the Iranian parts is consistent to the findings of Pan et al. (2016). Occasional horizontal transport in the UT from the eastern to the western part of the ASMA is an explanation for spatio-temporal evolution of CO mixing ratios, indicating that trace gas signatures in the Iranian part are dominated by the UT outflow of the Tibetan part of the ASMA.

5.3 Hydrochloric acid

As expected for a stratospheric tracer, the simulated HCl profiles (Figs. 5ef) show a strong anti-correlation with CO in the UT, with increased HCl in times of stratospheric influx (e.g. Fig. 5f, blue circle), and decreased HCl in the monsoon season. Stratosphere-to-troposphere exchange is pronounced during spring, consistent with the seasonality of the Brewer-Dobson circulation (Holton et al., 1995).

HCl plumes in the Iranian part rise to about 400 hPa below the tropopause in summer (Fig. 5e, circled), just like CO. Predominantly dry conditions in the western part prevent HCl from being washed out. However, CO and HCl are temporally anti-correlated in the mid-troposphere. Since HCl is emitted by the sea, we attribute this to alternating marine and continental origins in the uplifted air (Figs. 5ce).

Some HCl is descending from the tropopause into the mid-troposphere, as indicated by tilted patterns of enhanced HCl, which start at the tropopause and propagate downward (marked by an arrow in Fig. 5e). Similar tell-tale signs of descent also print through in other species in the Iranian part during summer.

There is almost no HCl in the Tibetan part throughout the monsoon season (Fig. 5f, black circle), except for the UT. Convection and thunderstorms are galore during the monsoon season in South Asia (Fig. 7d). Washing out does not affect CO, but effectively prevents transport of HCl to higher altitudes. Predominantly continental origins also contribute to an increased CO/HCl ratio in the rising plumes of the eastern part.

5.4 Reactive nitrogen

Simulated NO_x- and NO_y-profiles in the ASMA region from April to September differ to the rest of the year (Figs. 6abcd). E- and C-shaped NO_y-profiles dominate the Tibetan and Iranian parts, respectively (Figs. 6cd; examples of individual profiles in the supplement).

~~Both, NO_x and NO_y increase with altitude above the tropopause. Recycling of stratospheric NO_y additionally increases NO_x in the troposphere. Stratospheric influx contributes to increased NO_x mixing ratios in the UT in spring (blue circles in Figs. 4bh), but enhanced UT NO_x during the monsoon (Figs. 4gh, black circles) is rather due to lightning NO_x emissions in the Tibetan part than to stratospheric entrainments (compare Figs. 4bh).~~

NO_x and NO_y from boundary layer sources is uplifted, accompanied by conversion of some NO_x into NO_y. Solvable NO_y-components (e.g. HNO_3) become increasingly washed out (Fig. 6d), leading to a minimum of reactive nitrogen in the mid-troposphere in the Tibetan part in summer ~~The conversion of non solvable NO_x into solvable NO_y componentsFig. 5d facilitates subsequent loss by washing out.~~

~~There is less NO_x in the mid troposphere than in the UT or in the lower troposphere~~(Figs. 6bd). ~~, and little NO_x rises to the UT~~ Uplift from the lower troposphere is less important for UT NO_x and NO_y than $LiNO_x$ and stratospheric entrainments. The dependence of detrainment on altitude hardly affects trace gas profiles in the mid troposphere, as indicated by the corresponding CO profiles (Fig. 5d, circled). ~~in both parts and throughout the year.~~

Both, NO_x and NO_y gradually increase above the tropopause due to stratospheric photochemistry. Stratospheric influx contributes to increased NO_x mixing ratios in the UT in spring (blue circles in Figs. 5f, 6b), but enhanced UT NO_x during the monsoon (Fig. 6b, black circle) is rather due to lightning NO_x emissions in the Tibetan part than to stratospheric entrainments (Supplement).

NO_y can rise to about 400 hPa below the tropopause in the heat low over the Arabian Peninsula (circled in Fig. 6c). Downward transport (as indicated by anti-clockwise tilted signals, one example marked by an arrow in Fig. 6c) dominates above that altitude, preventing further uplift. With little in situ production of lightning NO_x over the Arabian Peninsula in summer (Figs. 7c and 10), UT NO_y in the Iranian part is dominated by the outflow of the Tibetan part.

As a combination of the different processes affecting NO_x and NO_y, the NO_x/NO_y ratio maintains a broad maximum in the TL throughout the year (Figs. 6ef). During the monsoon, the NO_x/NO_y ratio in the UTLS is larger in the western than in the eastern ASMA part (Figs. 6ef, circles). This indicates preferential export of high-NO_x air from the Tibetan part, or is an artefact of the possible dominance of a single source of $LiNO_x$ in the Iranian region (Fig. 10).

6 Processes and their interplay in the ASMA

In this section the observed and simulated trace gas signatures are related to simulated photochemical, transport and mixing properties of the ASMA. The term “interplay” is thereby used in a neutral sense regarding the direction of feedbacks

between different processes: It subsumes mostly one-way interactions (e.g. emissions affecting O_3 production, dynamics affecting trace gas distributions) here. We note upfront that the intra-annual variability of trace gas dynamics in the Tibetan and Iranian ASMA regions as discussed for the year 2012 in section 5 is largely similar in the other considered years (2010 – 2014, shown in the supplement~~, Figs. S2–S7 include the parameters shown in Figs. 4, 5~~).

6.1 Lightning NO_x

In our EMAC simulations, $LiNO_x$ is released based on a parameterisation that links flash frequency to updraft velocity in - also parameterised - convection. It is difficult to narrow down $LiNO_x$ emissions (Schumann and Huntrieser, 2007), and both parameterizations are a notorious source of uncertainty in global models. The parameterizations for convection (Tiedtke, 1989; Nordeng, 1994; Tost, 2006) and lightning (Grewe et al., 2001) used in our simulations have been tested in several studies (Tost et al., 2007; Grewe, 2009; Lopez, 2016) and appear to be state of the art. EMAC-simulated lightning activity matches the corresponding TRMM-LIS/OTD observations (Cecil, 2006) reasonably well, spatially and temporally ~~and spatially~~ (Supplement~~Appendix A~~). Simulated and observed NO along the HALO ESMVal flight track agree remarkably well within the ASMA region (accompanying paper). The same is true for comparisons of IAGOS-CARIBIC measurements of NO and our simulation's output along the IAGOS-CARIBIC flight tracks, where the agreement is particularly noticeable for the monsoon season in the ASMA region (Supplement~~Appendix A~~). There is no proof that EMAC is right for the right reasons, and a dedicated comparison to other models is desirable. For the current study, however, the above comparisons provide some confidence that $LiNO_x$ emissions have been captured well by the simulation.

Simulated $LiNO_x$ emission rate profiles for 2012 show prominent maxima for the eastern and western ASMA regions during spring (Figs. 7cd). Overall, $LiNO_x$ emissions are much stronger in the Tibetan part. The emissions reach up to the tropopause throughout the year, implying that $LiNO_x$ is emitted at higher potential temperatures during the monsoon season (Fig. 4b). Despite higher emission rates in the laterally averaged profiles (Fig. 4d), lightning activity in the Tibetan part is more sporadic and localized in spring than in summer (Figs. 10de). During the monsoon season, $LiNO_x$ is constantly replenished in the ASMA throughout the region (Figs. 10ghi). Sensitivity simulations show that UT NO_x (Fig. 6b) is mainly $LiNO_x$ during the monsoon season (Supplement~~Appendix A~~).

6.2 Entrainment of lower tropospheric air

The uplift of lower tropospheric air to the UT is a well known characteristic of the ASMA (Pan et al., 2016). Simulated CO profiles in the Tibetan region show episodes of such uplift not only for 2012 (Fig. 5d), but for every monsoon season 2010 – 2014 (S~~s~~upplement). This is consistent with the HALO ESMVal measurements, since the trace gas gradients observed in the ASMA can be explained by mixing between lower tropospheric air and stratospherically influenced air.

CO uplift to the UT and $LiNO_x$ emissions are both related to convection and it is remarkable that there is a much stronger correlation between the two in summer than in spring (Figs. 5d, 7d). We attribute this to three effects: (i) The large scale uplift at the south-western flank of the Himalayas is only active during the monsoon season and not exclusively driven by

deep convection (see sections 1, 3). It has been suggested as the main transport pathway of pollutants to the UT (Bergman et al., 2013; Pan et al., 2016), which is supported by our simulation (Fig. 11) and the location of maximum moist static energy (Boos and Hurley, 2013). Back-trajectory calculations in the accompanying paper identified this pathway as the source of enhanced CO in some of the HALO ESMVal measurements, despite that the underlying reanalysis does not account for (small scale) convection; (ii) In the UT the ASMA is an – although leaky - transport barrier, allowing some accumulation of the uplifted pollutants (Pan et al., 2016). There is no such transport barrier in spring; (iii) The spatial and temporal match of deep convection and increased CO at different altitudes reflects the potential for entrainment and subsequent convective transport of CO (Figs. 7gh). It is clearly increased in summer. More detailed analyses (Ssupplement) show that convection is localized over the coastal regions of Western Bengal and Bangladesh in April 2012. In contrast, during August 2012 convection is ubiquitous throughout the Tibetan region. It is most persistent at the south-western flank of the Himalayas and over the Tibetan plateau. This coincides with the highest CO mixing ratios, which are accumulated there by the prevalent south-westerly winds during the monsoon season. Consequently, more CO is transported through the troposphere in the Tibetan region during summer.

6.3 Photochemical O_3 production and ageing

The net photochemical O_3 production rate (Figs. 7ab) is derived from the difference of EMAC simulated diagnostic tracers $ProdO_3$ and $LossO_3$ (Jöckel et al., 2016). Here we take into account effective O_3 production and loss terms following (Crutzen and Schmailzl, 1983) and extended by Grewe et al. (2017, see their supplement). There are known high-O_3 biases in the simulation (Jöckel et al., 2016), and uncertainties in the chemical mechanism (Gottschaldt et al., 2013) also impose uncertainties onto O_3 photochemistry. Nevertheless our simulated net O_3 production rates in the ASMA (Fig. 7b) agree remarkably well with the independent estimate of Barret et al. (2016).

O_3 photochemistry is dominated by catalytic cycles in the troposphere and affected by a variety of parameters, e.g. ambient mixing ratios of H_2O, O_3, CO and NO_x (Ehhalt and Rohrer, 1994; Grooß et al., 1998; Jaeglé et al., 1998; Seinfeld and Pandis, 1998). We focus on NO_x and CO for illustration (Fig. 12). Photochemical O_3 production[1] ($ProdO_3$) non-linearly depends on ambient NO_x mixing ratios: It increases proportional to NO_x in the NO_x-limited regime, is almost independent of NO_x variations at higher NO_x mixing ratios, and a further increase of NO_x even leads to decreasing $ProdO_3$ (NO_x-saturated regime). Increasing CO increases $ProdO_3$ and shifts the point of maximum $ProdO_3$ to higher NO_x. Increasing H_2O impacts $ProdO_3$ qualitatively similar as increasing CO. Decreasing O_3 leads to higher $ProdO_3$, but NO_x at the point of maximum $ProdO_3$ is lowest for medium O_3 mixing ratios.

The simulation shows the superposition of the above effects, amongst others within the full complexity of the chemical mechanism. As a result, a net O_3 producing photochemistry prevails in the ASMA throughout the monsoon season (circled in Figs. 7ab). This is accompanied by net O_3 destruction during the monsoon season 300 hPa below the tropopause and lower.

[1] Net O_3 production in the UT is determined rather by $ProdO_3$ than by $LossO_3$ (Ssupplement, Figs. #+S6, #+S9, #+S17), so it is sufficient to analyze $ProdO_3$ in this context.

At the tropopause and slightly above, there is a local minimum of net O_3 production, followed by increased net O_3 production in the stratosphere. Net O_3 production is at maximum in the altitude range, where uplifted young air (enriched in CO and co-emitted volatile, organic O_3 precursors) mixes with NO_x-rich UT air (Figs. 5d, 6b, 7b).

$ProdO_3$ per NO_x shows a strong gradient at the altitude of maximum net O_3 production (circled in Figs. 7bf). This indicates the transition from the NO_x-limited to the NO_x-saturated regime (Fig. 12), but is superimposed by gradients of CO and other O_3 precursors. The maximum corresponds to about 300 pmol ~~/~~mol^{-1} NO_x (circled in Fig. 8h), and variations of NO_x in that region have a relatively little effect on net O_3 production ("2" in Fig. 12).

Going down from the TP in the ASMA, NO_x and O_3 generally decrease, while CO and H_2O increase (Figs. 5, 6; H_2O not shown). It's a multi-dimensional problem. CO (among others) determines the curve in the NO_x-vs-$ProdO_3$ diagram, and NO_x determines the operating point on the curve. Considering typical ranges of CO and NO_x in different parts of the ASMA, an area on the surface in $ProdO_3$-NO_x-CO space is termed "operating mode of the chemical system" in the following. Different chemical regimes (e.g. NO_x-limited or NO_x-saturated) are allowed within one operating mode. The non-linear dependence of $ProdO_3$ on ambient trace gas mixing ratios leads to the simulated maximum within the opposite gradients of those trace gases (NO_x decreases below the TP, while CO increases) in the UT ASMA. Going down from the TP, the chemical system goes from operating mode "3" to "2" to "1" (Fig. 12). In principle, all those operating modes could be in the NO_x-limited regime and still lead to a maximum of net O_3 production in the UT. However, our simulations also show the NO_x-saturated regime (S~~s~~upplement).

Periods of enhanced lightning NO_x in spring (circled in Fig. 7d) correspond to increased net O_3 production (Fig. 7b), but despite higher $LiNO_x$ emissions in spring, net O_3 production is at maximum in the ASMA. The main differences between the seasons are that there is less CO in the UT during spring (Fig. 5d) and lightning NO_x is available only locally (section 6.1. and Supplement~~Appendix A~~). More CO in the UTLS in summer increases $ProdO_3$ and the maximum possible O_3 production (Fig. 12). Too high NO_x in spring does not help $ProdO_3$ – or even pushes the system into the NO_x-saturated regime ("3" in Fig. 12). NO_x close to maximum $ProdO_3$ conditions ("2" in Fig. 12) throughout the region in summer leads to higher $ProdO_3$ in the lateral average.

Both, NO_x and other precursors are more abundant in the Tibetan part UT, resulting in larger photochemical O_3 production than in the Iranian part (Figs. 7ab). This is consistent to other studies (Liu et al., 2009a; Barret et al., 2016), which also found such an asymmetry. O_3 depleting conditions prevail in the mid-troposphere over the Arabian Peninsula throughout the summer (Fig. 7a, circled). Thus increased O_3 there (Fig. 5a) must be due to transport.

Confinement in the ASMA circulation allows the mixed air to age, i.e. to produce O_3. CO is being depleted in the process of ageing, and NO_x is transferred to NO_y. The other source of aged air is entrainment from the TL, which is however enriched in HCl (at least within the photochemical lifetime of HCl). O_3 is produced in the ASMA at a net rate of about 4 nmol mol^{-1} day^{-1} (Fig. 7b), and simulated O_3 mixing ratios in the UT of the ASMA region vary by about 120 nmol ~~/~~mol^{-1} (Fig. 8b). It would take 30 days to cover that range by photochemical O_3 production alone. The observed values in the ASMA filament cover a range of about 48 nmol ~~/~~mol^{-1} (Fig. 8c), corresponding to 12 days of photochemical O_3 production. According to the

trajectory calculations in the accompanying paper, this is about the time needed to circle the ASMA. The above O_3 variability of course includes different amounts of O_3 from the TL, and O_3 productivity varies too. Neglecting these uncertainties, it takes one or two rotations of the ASMA to transform O_3-depleted, freshly uplifted air into aged, O_3-enhanced air. O_3-depletion in the ASMA relative to the regional average can only be maintained by frequent replenishment of young air.

6.4 Entrainment of tropopause layer air

Here we focus on the less well known entrainment of stratospheric or TL air into the free troposphere, which is supported by the unique thermodynamic conditions over the Tibetan plateau in summer (Fig. 2). The prevailing northerly winds (Kunze et al., 2010) of the eastern ASMA flank (Fig. 2) tend to transport high-PV (stratospheric or TL, Fig. 4c) air along the isentropic surfaces into the troposphere (Ren et al., 2014; Kunz et al., 2015). This effect was also detected by Konopka et al. (2010) as enhanced horizontal transport of O_3-rich air from the extratropics into the TTL. Such transport from the TL or even the extratropical lower stratosphere into the free tropical troposphere may not leave a tell-tale signature of increased potential temperature in the corresponding air masses in the tropics. This includes the 350 K – 370 K isentropes that were encountered during the HALO ESMVal campaign in the tropics (Fig. 4; θ estimates for the measurements are shown in the supplement). Additional stratospheric or TL contributions at the outer ASMA edge other than at the eastern flank are also plausible. The eastern Mediterranean and Central Asian region is a global hot spot of tropopause folding activity (Tyrlis et al., 2014), which is related to ASMA dynamics and generates enhanced O_3 levels through stratosphere-troposphere exchange (Akritidis et al., 2016). If the ASMA circulation encompasses that tropopause folding hotspot, it may pick up stratospheric entrainments.

A stratospheric influence is manifested in our measurements by increased HCl mixing ratios in combination with other tracers (section 4.3).

Did the HALO ESMVal campaign encounter an exceptional situation, or does TL entrainment at the eastern ASMA flank occur more often? The synoptic situation in question is characterized by a filament of enhanced HCl that is carried along the south-eastern ASMA flank, around ~~a~~an HCl-depleted ASMA interior. Here we analyse the evolution of simulated HCl mixing ratios at θ = 355 K, on a meridional (N-S) transect at 90°E, throughout the monsoon seasons of 2010 to 2014. The transition between eastward and westward winds indicates the location of the ASMA centre on the meridional transect, which wobbles around 30°N (white "ridgeline" in Fig. 3b). Enhanced tropospheric HCl mixing ratios south of the ridgeline serve as an indicator of TL entrainment (Fig. 3c). Caution with this interpretation is only needed at times when the ASMA is shifted to the West (compare Fig. 3a), because the transect in Fig. 3c may then be too far within the eastern ASMA flank. Episodes of increased HCl in the southern or eastern ASMA flank cover at least half of the time axis, showing that entrainment of TL air into the ASMA circulation is quite a common process. One horizontal slice from each analysed month is shown in the supplement, indicating that filaments of enhanced HCl often protrude from a TP trough of a Rossby wave at the eastern ASMA flank. The association of this mixing process with planetary wave breaking events is a topic of ongoing research (Lubis and Nakamura, 2017).

6.5 Radial stratification and patchy trace gas distributions

Deep convection from the lower troposphere discharges more towards the ASMA interior, as shown by studies that report relatively young air there (Li et al., 2005; Randel and Park, 2006; Park et al., 2008; Liu et al., 2009b; Kunze et al., 2010; Liu et al., 2011; Santee et al., 2017) and also by our simulation (section 6.4). In contrast, trace gas signatures in a belt of outer streamlines are dominated by a combination of photochemically aged lower tropospheric air and entrainments of UT air surrounding the ASMA. In this schematic of an undisturbed anticyclone, interior trace gas signatures are generally characterised by lower O_3 mixing ratios than fringe signatures then. Such radial zoning in the ASMA is an expression of almost closed circulation, and was observed in IAGOS-CARIBIC in situ data of flights between Chennai, India and Frankfurt, Germany (Baker et al., 2011; Rauthe-Schöch et al., 2016). Increased O_3 mixing ratios were found in the northern part of the ASMA, and decreased levels towards the southern end of the flights.

Radial stratification is counteracted by the general on-off nature of TL entrainment, upwellings from the lower troposphere and lightning. Still considering only undisturbed ASMA circulation, all those effects lead to patches of air with different trace gas signatures. Each of these patches might again receive contributions from any of the above sources. In principle all sorts of combinations are possible, generating heterogeneity. In contrast, mixing and photochemical ageing are homogenizing effects. In combination with closed streamlines the preferential positions of the different sources might still print through as radial stratification in the ASMA, or show up in individual situations (section 6.4).

However, neither the HALO ESMVal measurements, nor ~~various~~ sequences of simulated snapshots (S~~s~~upplement) show a clear stratification. The idealised picture that the ASMA circulation is dominated by stationary, closed streamlines is certainly not realistic - at least not on the timescales of the homogenizing effects.

6.6 Splitting-up and stirring

Transient streamlines, particularly eddy shedding or splitting of the ASMA, effectively overcome radial transport barriers. Whether stratified or patchy – any trace gas distribution in the ASMA might be subject to effective stirring then. There is an ongoing discussion about different dynamical modes of the ASMA (Nützel et al., 2016; Pan et al., 2016).

A splitting-up event occurred just during the HALO ESMVal campaign, corresponding to the transition from a longitudinally elongated phase to a double centre phase in the nomenclature of Pan et al. (2016). A sequence of simulated streamlines and tracer distributions shows that fringing parts of the elongated anticyclone become part of the interiors of both resulting anticyclones after the splitting, and interior parts are diverted into the fringes (~~supplement,~~ Fig. 13). Even if not all possible cases are covered by the example, it is easily conceivable that fringing parts may also stay in the fringes and interior parts in the interiors. For a given location and timing of eddy shedding or splitting, the final trace gas distribution simply depends on the initial distribution of different patches. The redistribution of different parts of the anticyclone guarantees a high variability for outflow and interior, whenever the closed circulation breaks down.

How often does this happen? Splitting and eddy shedding mainly occur in zonal (E-W) direction, where the transition from northward wind in the west to southward wind in the east indicates the centre of an anticyclone or eddy. We analyse the evolution of meridional winds at θ = 355 K, on a wide (15°N – 35°N) zonal transect, throughout the monsoon seasons of 2010 to 2014 (Fig. 3a).

The pattern at the given altitude is consistent with one dominating anticyclone, centred at about 90°E. While the northerly winds east of 90°E are relatively persistent, episodes of entirely southerly winds in the western part of the one-piece ASMA alternate with episodes of smaller, secondary anticyclones. Smaller anticyclones also occur regularly east of the Tibetan anticyclone, corresponding to eddy shedding to the East. The splitting event that occurred during the HALO ESMVal campaign is clearly visible in Fig. 3a, too. Such instabilities occur approximately twice a month. This coincidentally corresponds to the timescale needed to photochemically erase O_3-depleted signatures in young air masses.

7 Summary

This study complements a detailed analysis of in situ trace gas measurements in the ASMA, obtained during the ESMVal campaign with the research aircraft HALO in September 2012 (Gottschaldt et al., 2017). The measurements are put in the context of the EMAC simulated annual evolution of trace gas profiles in the ASMA region and simulated tracer-tracer relations. This led to the following qualitative understanding of the interplay of processes that determine the trace gas distributions in the ASMA and its outflow (Fig. 14):

Air from the steeply inclined TL is entrained by outer ASMA streamlines at the eastern and possibly northern ASMA flank, defining a fringing zone. Tropopause troughs facilitate the entrainment.

Stratospherically enhanced tracers like HCl and O_3 print through in the entrained air. Thus the fringe is not just a transport barrier, separating the ASMA interior from the respectively surrounding UT. It has a distinct genesis, resulting in air masses with distinct trace gas signatures that may be transported relatively unperturbed over long distances. Deep convection and a conduit of upwelling air over the Tibetan plateau (Bergman et al., 2013) inject lower tropospheric air mainly into the Tibetan part of the ASMA. Enhanced CO is an indicator for this process. Convection is accompanied by in situ production of lightning NO_x, mainly determining mixing ratios of this O_3 precursor in the ASMA.

In the idealised case of one intact anticyclone (Fig. 14a) the interior would then be dominated by photochemical ageing of those O_3-poor injections. Net O_3 production dominates in the ASMA, and is particularly enhanced where lower tropospheric O_3 precursors (VOCs) meet UT precursors (NO_x). The preferential positions of convective versus TL entrainments facilitate radial stratification in the ASMA. The intermittent nature of the entrainments, combined with the varying position of the anticyclone lead to patches of air that have different origins and are in different stages of ageing. Mixing and ageing act homogenizing, but each of these patches might again receive fresh entrainments from the TL or by convection plus lightning. Eddy shedding or transitions between other dynamical modes of the ASMA effectively overcome radial transport barriers (Fig. 14b, summarizing ~~supplemental~~ Fig. 13 and supplemental Fig. S18). Whether stratified or patchy – any trace gas

distribution in the ASMA is subject to effective stirring then. Fringe air can be diverted into the interiors of both anticyclones, and likewise interior air is redistributed throughout the UT in the monsoon region. Remnants of earlier such events gradually lose memory of their origins, leading to a mixed "background" (grey in Fig. 14b).

We found that the processes that led to the curious combination of both enhanced lower tropospheric and TL tracers in the ASMA filaments encountered by the HALO ESMVal campaign are not exceptional: entrainment of TL air and dynamical instabilities of the ASMA occur quite frequently. Deep convection and thunderstorms are common throughout the monsoon season, accompanied by a net O_3 producing photochemical regime. The alternating interplay of those processes results in highly variable, patchy trace gas distributions in the ASMA. Processes that increase O_3 and its precursors dominate in the Tibetan part of the ASMA. The Iranian part is dynamically dominated by the Tibetan part in the UT. O_3-rich TL entrainments and precursor-rich air, both main ASMA components tend to increase O_3 in the tropospheric ASMA outflow - e.g. over the Arabian Peninsula.

~~**Appendix A: Lightning NO_x in the ASMA**~~

~~The discussion of the evolution of the $LiNO_x$ profile (Fig. 5) is supplemented by the corresponding lateral distribution of monthly mean $LiNO_x$ emission rates at the altitude of the HALO ESMVal measurements (Fig. A1). We note that there are strong, but localised emissions in the Iranian and Tibetan parts in spring (Fig. A1: Apr May). $LiNO_x$ emissions are distributed throughout the Tibetan region in summer (Fig. A1: Jul Sep). The simulated spatio temporal emission patterns are similar for 2013 and 2014 (not shown).~~

~~Given the uncertainties of the parameterizations for convection and lightning in the model, smoothing and limited detection efficiencies in the observations, our simulated spatial temporal distribution of lightning activity compares reasonably well to corresponding observations (supplement, Fig. S10). In particular we note that also the observations over South Asia show stronger lightning activity during spring than during the monsoon season. The observed maximum of lightning activity over the coastal areas of Western Bengal and Bangladesh in April also shows up in the simulation.~~

~~As noted in section 2, we compare simulated NO and NO_y to the corresponding IAGOS CARIBIC observations (Fig. A2). Commercial airliners do not fly as high as HALO and the tracks hardly reach the southern ASMA fringe, but the northern ASMA edge and the center of the monsoon region have been sampled multiple times. We evaluated all 345 IAGOS CARIBIC flights between 19 May 2005 and 9 April 2014, considering the respective latest data versions as of 10 November 2017. In total 86 flights between Frankfurt (IATA code: FRA) and Chennai (MAA) or Guangzhou (CAN) or Bangkok (BKK) transected the ASMA region. 32 of these flights provide NO data there, and 66 flights provide NO_y. Neglecting data below 300 hPa and subsampling to the time resolution of the simulation yields the numbers of comparable data that are given in Figs. A2bd. Given the above uncertainties related to the representation of $LiNO_x$ in the simulation, NO matches the corresponding IAGOS CARIBIC observations surprisingly well (Fig. A2b). This holds also for the more robust (more data)~~

global comparison (Fig. A2a). Increased $LiNO_x$ emissions in the ASMA region in spring are also consistent to IAGOS-CARIBIC, and the simulation might even slightly underestimate those emissions (Fig. A2b: MAM).

In order to link the $LiNO_x$ emissions to the NO_x burden in the ASMA region, a suite of EMAC sensitivity simulations with modified emission factors was conducted (Figs. A3, A4). All EMAC analyses in the main text are based on simulation RC1SD-base-10a (Jöckel et al., 2016), which is given in Fig. A3 just for comparison. The other simulations discussed in the context of Figs. A3 and A4 here are derived from EMAC simulation RC1SD-base-10, which differs in road traffic emissions and optical properties of stratospheric aerosol (Jöckel et al., 2016) from RC1SD-base-10a. Total $LiNO_x$ emissions in RC1SD-base-10 are 4.6 Tg(N) in 2012 (Jöckel et al., 2016), which is in the realistic range of 2 – 8 Tg(N) yr^{-1} (Schumann and Huntrieser, 2007). RC1SD-base-10 and our base simulation for the $LiNO_x$ sensitivity analysis (b01) are both operated in chemistry-climate-model (CCM) mode, i.e. including interactive chemistry with feedback on dynamics. Simulation b01 differs only in the usage of daily (Kaiser et al., 2012) instead of monthly biomass burning emissions and 5 h instead of 10 h output intervals. Feedbacks from chemistry on dynamics in all quasi-chemistry transport model mode (QCTM) (Deckert et al., 2011) simulations are based on identical trace gas time series from b01. The same dynamics incl. convection is simulated in all QCTM simulations. Differences between a QCTM reference simulation (q01) and sensitivity simulations (s*) are thus exclusively due to chemical perturbations. All QCTM simulations cover June – September 2012, but the first 3 months were discarded for spin-up.

Figure A3 shows that RC1SD-base-10a captures observed O_3, CO, NO and NO_y along the HALO-ESMVal flight path slightly better than b01 and q01. We are yet confident that the overall agreement is good enough for the analysis of chemical perturbations. For the QCTM sensitivity analyses it is more important to note that differences between b01 and q01 are negligible.

Figure A4k shows that halving $LiNO_x$ emission factors results in almost halved NO_x in the uppermost troposphere. Doubling of $LiNO_x$ emissions leads to almost doubled NO_x just below the tropopause (Fig. A4m). The biggest relative sensitivity in Fig. A4km almost coincides with the altitude range of the largest NO_x mixing ratios just below the tropopause (Fig. A4j). Thus, in our simulations $LiNO_x$ clearly dominates the NO_x budget from the tropopause to 100 hPa below it. The impact of LiNOx fades out at lower altitude, and almost vanishes at 400 hPa below the tropopause. This is consistent with the profiles of $LiNO_x$ emissions in September 2012, which mainly occur in the Tibetan part of the ASMA (Fig. 5d).

Modifications of NO_x print through on other O_3 precursors mainly via changes to the atmospheric oxidizing capacity (OH: Figs. A4ghi). In response to halved $LiNO_x$, OH decreases 200 hPa below the tropopause and lower, and increases above (Fig. A4h). The effects are reversed for doubled $LiNO_x$ (Fig. A4i). The largest relative effects coincide with largest absolute OH mixing ratios.

CO decreases throughout the shown altitude range for halved $LiNO_x$ (Fig. A4e). Without major production terms in the UT, modifications to CO mixing ratios are dominated by the loss reaction $CO + OH \rightarrow H + CO_2$. The rate coefficient of this reaction is proportional to pressure, and otherwise depends only on constants (supplement to Jöckel et al. (2016)). Laterally averaged CO mixing ratios vary little from 50 to 400 hPa below the tropopause (Fig. A4d), but are affected by decreased and

increased OH (Figs. A4fg). Decreased OH in the lower half of the domain dominates the overall CO response. CO rises through this region with higher pressures before reaching the UT in the Tibetan part of the ASMA (Fig. 4), which obviously outweighs the CO response to increased OH in the UT of Tibetan and Iranian part combined. Increased OH 200 – 500 hPa below the tropopause consequently leads to an overall decrease of CO in response to doubled $LiNO_x$ (Fig. A4f). The O_3 precursors NO_x and CO display opposite trends in response to $\Delta LiNO_x$.

Curiously, HCl shows the opposite response to modified $LiNO_x$ (Figs. A4abc). There is no chemical production of HCl in the UT, and the only loss term in the simulations is $HCl + OH \rightarrow Cl + H_2O$. The rate coefficient of this reaction is 1.7E-12 * EXP(-230/Temperature), see supplement to Jöckel et al. (2016). However, the tropospheric response of HCl to ΔOH is dominated rather by the vertical profile of HCl mixing ratios than by lower temperatures towards the tropopause. Almost all HCl in the UT is of stratospheric origin, and HCl mixing ratios steeply increase across the tropopause. Thus the UT response of HCl is dominated by ΔOH near the tropopause: increased OH for halved $LiNO_x$ increases HCl losses, and vice versa for doubled $LiNO_x$.

The response of UT net O_3 production to $\Delta LiNO_x$ (Figs. A4qrs) has mostly the same sign as ΔNO_x. As noted already in the context of Fig. 4, opposite gradients of O_3 precursors NO_x and CO in the UT lead to a broad altitude range of enhanced net O_3 production in the ASMA, centred about 100 hPa below the tropopause. O_3 production is limited by NO_x in lower altitudes and by CO (and other volatile organic compounds) towards the tropopause. NO_x and CO display opposite trends in response to $\Delta LiNO_x$, but relative changes to NO_x are larger and dominate the overall response of net O_3 production. We note, however, that the largest increase of NO_x at the end of September (circled in Fig. A4m) decreases net O_3 production to zero or even net loss (circled in Fig. A4s), indicative of the NO_x limited photochemical regime.

O_3 mixing ratios respond to $\Delta LiNO_x$ essentially like net O_3 production in the UT (Figs. A4nop). The altitude of maximum relative ΔO_3 is slightly lower than the altitude of maximum absolute changes to net O_3 production. We attribute this effect to upwards increasing absolute O_3 mixing ratios.

Appendix B: Reactive nitrogen in the ASMA

Nitrogen oxides are key parameters in atmospheric chemistry, partly controlling the O_3 production in the troposphere and lower stratosphere. In the UTLS, enhanced NO_y originates both from tropospheric and from stratospheric sources. In the lower troposphere odd nitrogen species are co-emitted with carbon monoxide in combustion processes, resulting in a strong correlation between both species. NO_y is enhanced in the stratosphere (mainly HNO_3), but it also comprises species with tropospheric sources ($LiNO_x$). Thus it is not a viable tracer for stratospheric air on its own.

The simulation matches IAGOS-CARIBIC NO_y almost perfectly on the global scale (Fig. A2e), and only moderately overestimates it during summer in the ASMA region (Fig. A2d: JJA).

Simulated NO_y profiles in the ASMA region from April to September differ to the rest of the year (Figs. B1ab), but the monsoon season is also distinct: during summer there is more NO_y in the UTLS and mid-troposphere in both, the Tibetan

and Iranian regions (Figs. B1ab, 8). Episodes of enhanced NO_y (~1.5 nmol/mol) in the UT are frequent in the Tibetan part during summer, and alternate with periods of decreased NO_y (~1.0 nmol/mol). However, the altitude region just above the tropopause is hardly affected by this UT variability and maintains an average mixing ratio of ~1.2 nmol/mol NO_y (Figs. B1ab). NO_y mixing ratios generally increase with altitude in the lower stratosphere, but reach 1.6 nmol/mol only at about 15 hPa above the tropopause. E shaped NO_y profiles dominate the Tibetan part, with maxima in the lower troposphere, in the UT and in the lower stratosphere (Fig. B2b). Less NO_y is simulated in many profiles for the mid troposphere and just above the tropopause transport barrier (Fig. B3). E shaped NO_y profiles were also reported by the NOXAR measurement campaign in the northern mid latitudes and corresponding modelling studies (Grewe et al., 2001). The E shape in northern mid-latitudes was in part attributed to aviation NO_x emissions (Rogers et al., 2002), but aviation effects are much smaller in the tropics (Gottschaldt et al., 2013). Instead of aviation emissions, in situ production of lightning NO_x in the prevalent thunderstorms of the monsoon season increases NO_y in the UT over South Asia (Fig. 5d, see also Appendix A). Thus a possible explanation for the E shaped NO_y profiles in the eastern ASMA part during the monsoon season is as follows: NO_y from boundary layer sources' pollution is uplifted, and solvable NO_y components (e.g. HNO_3, N_2O_5) become increasingly washed out (Fig. S4a). At about 400 hPa below the tropopause only non solvable components (e.g. NO_x) are left. Episodes of increased NO_y in the UT are well correlated with increased lightning NO_x emissions (Figs. S4a, 5d). NO_y mixing ratios however increase with altitude above the tropopause, due to increased photochemical production of HNO_3 in the stratosphere. With little in situ production and not much transport from above or below, NO_y mixing ratios in the region between the tropopause and 15 hPa above the tropopause are often smaller than in the adjacent altitudes.

Profiles in the western, i.e. Iranian ASMA part (Fig. B1a) have a different history of origins, and with just one minimum in the mid troposphere are mostly C shaped (Fig. B2). During summer the Arabian Peninsula is dry. Convection (as indicated by lightning NO_x emissions in Fig. 5c) is mainly localised near the Bab al Mandab Strait (Fig. A1), i.e. at the edge of the region we defined for calculating profiles of the Iranian part of the ASMA. Washing out is negligible throughout most of the Iranian region (Fig. A1), and therefore NO_y can rise to about 400 hPa below the tropopause (circled in Fig. B1a). Downward transport (as indicated by anti clockwise tilted signals, one example marked by an arrow in Fig. B1a) dominates above that altitude, preventing further uplift. With little in situ production of lightning NO_x over the Arabian Peninsula in summer (Figs. 5c and A1), UT NO_y in the Iranian part is dominated by the outflow of the Tibetan part.

As a combination of the different effects affecting NO_x and NO_y, the NO_x/NO_y ratio maintains a broad maximum in the TL throughout the year (Figs. B1cd). The monsoon season is characterised by particularly little fluctuations of NO_x/NO_y (Figs. B1cd, circles). During the monsoon, the NO_x/NO_y ratio in the UTLS is higher in the western than in the eastern ASMA part. This indicates preferential export of high NO_x air from the Tibetan part, or is an artefact of the possible dominance of a single source of LiNO$_x$ in the Iranian averaging region (Fig. A1).

Simulated O_3 and NO_x increase in the stratosphere with a higher O_3/NO_x ratio than in the troposphere (Fig. B3a). At NO_x mixing ratios of more than 0.7 nmol/mol the corresponding O_3 mixing ratios would allow distinguishing stratospheric influence from tropospheric in situ production, but the range covered by the HALO ESMVal measurements is just at the

intersection of stratospheric and tropospheric branch (orange box in Fig. B3a). Similar HCl mixing ratios are simulated throughout the ranges of measured NO_x and O_3 (orange box in Fig. B3b). Measurements of increased NO_x in combination with increased O_3 (upper right corner of the orange boxes in Fig. B3) are compatible with both, increased in situ O_3 production and influence from the stratospheric branch. Consequently almost all measurements in the ASMA filament are well correlated on the scale of all our ASMA measurements (Fig. B3c). As discussed in the accompanying paper, the positive correlation between NO and O_3 is attributed to enhanced O_3 production due to increased NO, if NO also positively correlates with NO_y.

There are three distinct regions in Fig. B3d: a blueish stratospheric branch, a dark TL branch, and a reddish UT region. As a consequence of the local NO_y minimum directly above the tropopause (Figs. B1b, B2), the most decreased NO_y mixing ratios in Fig. B3d also show up in samples taken from near the tropopause. Measured NO and NO_y values in the ASMA filament are well correlated (Fig. B3f), consistent with almost constant NO_x/NO_y ratios in the UT (Figs B1cd). Furthermore, the simulation shows much more scatter in NO_x vs O_3 space than the observations. The narrow, linear distribution of the ASMA measurements in Figs. B3cf indicates that all parts of the transected filament had similar sources of reactive nitrogen. This is consistent with Appendix A, where lightning is found to be the dominating source of reactive nitrogen in the ASMA. The filament had seen convection at the eastern ASMA flank three to five days before the measurements. Thus the gradients of NO and NO_y in Figs. B3cf can be explained by different amounts of lightning NO_x of approximately the same age.

We attribute some larger scale trace gas gradients in the measurements to different photochemical O_3 production (section 4). There are positive correlations between NO & O_3 and NO & NO_y (Figs. B3cf), but not between CO & O_3 (Fig. 3e). This combination indicates that the measurements show a NO_x limited photochemical regime.

Appendix C: Primer for tracer-tracer diagrams

Tracer tracer diagrams show mixing ratios of two species encountered simultaneously. Sampling of two different air masses that are in the process of mixing is indicated by a mixing line in the tracer tracer diagram. The slope of the mixing line provides additional clues about the origin of the original air parcels ("end members"). If the ratios of the end members remain constant over time, the slope of the mixing line is conserved, as long as the mixing process continues. If the mixing processes stops, the mixing lines converge to a single point in the tracer tracer diagram. If the reservoir of one end member is bigger than the other, points in the tracer tracer diagram will be close to the dominating end member. However, the relative size of the reservoirs does not affect the slope of mixing lines, thus allowing detection of even small entrainments. Slopes change in case of mixing ratio changes over time (e.g. via in situ production or loss) of one or both reservoirs. Different effects may lead to similar tracer tracer relations, resulting in ambiguity when trying to reconstruct end members or disentangling mixing and chemical effects. Furthermore, mixing lines in general exist in a multi dimensional tracer space, and thus lines in a tracer tracer plot need to be considered as projections onto 2d space. They might also be the result of mixing between more than two reservoirs. Additional dimensions (tracers) need to be considered to reduce ambiguities.

Data availability

The simulation results analysed here are archived at the German Climate Computing Center (DKRZ) and are available on request. It is planned to move them to the Climate and Environmental Retrieval and Archive (CERA) database at the German Climate Computing Centre (DKRZ; http://cera-www.dkrz.de/WDCC/ui/Index.jsp). The corresponding digital object identifiers (doi) will be published on the MESSy consortium web page (www.messy-interface.org). The observational data of the HALO ESMVal flight used here are available from the HALO database (doi:10.17616/R39Q0T).

Competing interests

The authors declare that they have no conflict of interest.

Author contributions

K. Gottschaldt analysed the EMAC and final in situ data, conducted the Lagrangian calculations, produced the plots and drafted the paper. H. Schlager conceived the study, led the HALO ESMVal campaign and interpreted EMAC and in situ data. R. Baumann wrote and helped with the code that facilitated the HYSPLIT calculations. P. Jöckel led the ESCiMo project, coordinated the preparation of and conducted the EMAC simulations. D. S. Cai and P. Graf prepared a significant part of the boundary conditions, and V. Grewe was responsible for the $ProdO_3$ and $LossO_3$ diagnostics in the ESCiMo simulations. V. Eyring conceived and led the ESMVal project. T. Jurkat, C. Voigt, A. Zahn, and H. Ziereis supplied in situ measurements. All authors contributed to the text.

Acknowledgements

The authors gratefully thank H. Garny and P. Hoor for valuable comments on the manuscript, A. Baker, B. Barret, B. Brötz, J. Crawford, F. Frank, H. Huntrieser, P. Konopka, R. Müller, M. Nützel, L. Pan, R. Ren, M. Santee, M. Schultz, G. Stiller, B. Vogel for helpful discussions, and the ACAM (Atmospheric Composition and the Asian Monsoon; www2.acom.ucar.edu/acam) activity for providing a forum.

We thank the German Science Foundation DFG for funding within HALO-SPP 1294 under contracts JU 3059/1-1, SCHL 1857/2-2, SCHL 1857/4-1, VO 1504/2-1 and VO 1504/4-1. The HALO ESMVal aircraft campaign was funded by the DLR-project ESMVal. KG and HS appreciate support by the EU project StratoClim (grant no. 603557) and BMBF project Spitfire (grant no. 01LG1205B). CV and TJ thank financing by the Helmholtz Association under contract no. VH-NG-309 and under contract No. W2/W3-60. In addition we thank the flight department of DLR for their great support during the campaign. P.

Hoor and S. Müller contributed to the CO measurements and S. Kaufmann supervised the HCl measurements during the flight.

The EMAC model simulations were performed at the German Climate Computing Centre (DKRZ) through support from the Bundesministerium für Bildung und Forschung (BMBF). DKRZ and its scientific steering committee are gratefully acknowledged for providing the HPC and data archiving resources for the projects 853 (ESCiMo - Earth System Chemistry integrated Modelling) and 854 (ESMVal).

We used the NCAR Command Language (NCL) for data analysis and to create some of the figures of this study. NCL is developed by UCAR/NCAR/CISL/TDD and available on-line: http://dx.doi.org/10.5065/D6WD3XH5.

The article processing charges for this open-access publication were covered by a Research Centre of the Helmholtz Association.

Last but not least we thank the two anonymous reviewers for their insightful comments regarding $LiNO_x$, convective and isentropic transport, which greatly helped to improve the paper.

References

Akritidis, D., Pozzer, A., Zanis, P., Tyrlis, E., Škerlak, B., Sprenger, M., and Lelieveld, J.: On the role of tropopause folds in summertime tropospheric ozone over the eastern Mediterranean and the Middle East, Atmospheric Chemistry and Physics, 16, 14025-14039, 10.5194/acp-16-14025-2016, 2016.

Baker, A. K., Schuck, T. J., Slemr, F., van Velthoven, P., Zahn, A., and Brenninkmeijer, C. A. M.: Characterization of non-methane hydrocarbons in Asian summer monsoon outflow observed by the CARIBIC aircraft, Atmospheric Chemistry and Physics, 11, 503-518, 10.5194/acp-11-503-2011, 2011.

Barret, B., Sauvage, B., Bennouna, Y., and Le Flochmoen, E.: Upper-tropospheric CO and O3 budget during the Asian summer monsoon, Atmospheric Chemistry and Physics, 16, 9129-9147, 10.5194/acp-16-9129-2016, 2016.

Bergman, J. W., Fierli, F., Jensen, E. J., Honomichl, S., and Pan, L. L.: Boundary layer sources for the Asian anticyclone: Regional contributions to a vertical conduit, Journal of Geophysical Research: Atmospheres, 118, 2560-2575, 10.1002/jgrd.50142, 2013.

Boos, W. R., and Kuang, Z.: Dominant control of the South Asian monsoon by orographic insulation versus plateau heating, Nature, 463, 218-222, 10.1038/nature08707, 2010.

Boos, W. R., and Hurley, J. V.: Thermodynamic Bias in the Multimodel Mean Boreal Summer Monsoon, Journal of Climate, 26, 2279-2287, 10.1175/jcli-d-12-00493.1, 2013.

Brenninkmeijer, C. A. M., Crutzen, P. J., Boumard, F., Dauer, T., Dix, B., Ebinghaus, R., Filippi, D., Fischer, H., Franke, H., Frieß, U., Heintzenberg, J., Helleis, F., Hermann, M., Kock, H. H., Koeppel, C., Lelieveld, J., Leuenberger, M., Martinsson, B. G., Miemczyk, S., Moret, H. P., Nguyen, H. N., Nyfeler, P., Oram, D., O'Sullivan, D., Penkett, S. A., Platt, U., Pupek, M., Ramonet, M., Randa, B., Reichelt, M., Rhee, T. S., Rohwer, J., Rosenfeld, K., Scharffe, D., Schlager, H., Schumann, U., Slemr, F., Sprung, D., Stock, P., Thaler, R., Valentino, F., van Velthoven, P., Waibel, A., Wandel, A., Waschitschek, K., Wiedensohler, A., Xuref-Remy, I., Zahn, A., Zech, U., and Ziereis, H.: Civil Aircraft for the regular investigation of the

atmosphere based on an instrumented container: The new CARIBIC system, Atmos. Chem. Phys., 7, 4953-4976, https://doi.org/10.5194/acp-7-4953-2007, 2007.

Cecil, D. J.: LIS/OTD 2.5 Degree Low Resolution Monthly Climatology Time Series (LRMTS): Data set available online from the NASA Global Hydrology Resource Center DAAC, Huntsville, Alabama, U.S.A. doi: http://dx.doi.org/10.5067/LIS/LIS-OTD/DATA311, access: https://lightning.nsstc.nasa.gov/data/data_lis-otd-climatology.htm, 18. September 2017, 2006.

Cristofanelli, P., Bracci, A., Sprenger, M., Marinoni, A., Bonafè, U., Calzolari, F., Duchi, R., Laj, P., Pichon, J. M., Roccato, F., Venzac, H., Vuillermoz, E., and Bonasoni, P.: Tropospheric ozone variations at the Nepal Climate Observatory-Pyramid (Himalayas, 5079 m a.s.l.) and influence of deep stratospheric intrusion events, Atmospheric Chemistry and Physics, 10, 6537-6549, 10.5194/acp-10-6537-2010, 2010.

Crutzen, P. J., and Schmailzl, U.: Chemical budgets of the stratosphere, Planet. Space Sci., 31, 1009-1032, 1983.

Deckert, R., Jöckel, P., Grewe, V., Gottschaldt, K., and Hoor, P.: A quasi chemistry-transport model mode for EMAC, Geoscientific Model Development, 4, 195-206, 10.5194/gmd-4-195-2011, 2011.

Dee, D. P., Uppala, S. M., Simmons, A. J., Berrisford, P., Poli, P., Kobayashi, S., Andrae, U., Balmaseda, M. A., Balsamo, G., Bauer, P., Bechtold, P., Beljaars, A. C. M., van de Berg, L., Bidlot, J., Bormann, N., Delsol, C., Dragani, R., Fuentes, M., Geer, A. J., Haimberger, L., Healy, S. B., Hersbach, H., Hólm, E. V., Isaksen, L., Kållberg, P., Köhler, M., Matricardi, M., McNally, A. P., Monge-Sanz, B. M., Morcrette, J. J., Park, B. K., Peubey, C., de Rosnay, P., Tavolato, C., Thépaut, J. N., and Vitart, F.: The ERA-Interim reanalysis: configuration and performance of the data assimilation system, Quarterly Journal of the Royal Meteorological Society, 137, 553-597, 10.1002/qj.828, 2011.

Dethof, A., O'Neill, A., Slingo, J. M., and Smit, H. G. J.: A mechanism for moistening the lower stratosphere involving the Asian summer monsoon, Quarterly Journal of the Royal Meteorological Society, 125, 1079-1106, 10.1002/qj.1999.49712555602, 1999.

Draxler, R. R., and Hess, G. D.: An overview of the HYSPLIT_4 modelling system for trajectories, dispersion and deposition, Aust. Met. Mag., 47, 295-308, 1998.

Draxler, R. R., and Rolph, G.: HYSPLIT (HYbrid Single-ParticleLagrangian Integrated Trajectory) model: http://www.arl.noaa.gov/ready/hysplit4.html, access: 26 June 2015, 2015.

Dunkerton, T. J.: Evidence of meridional motion in the summer lower stratosphere adjacent to monsoon regions, Journal of Geophysical Research, 100, 16675–16688, 10.1029/95JD01263, 1995.

Ehhalt, D. H., and Rohrer, F.: The impact of commercial aircraft on tropospheric ozone, Proceedings of the 7th BOC Priestley Conference, Lewisburg, Pennsylvania, USA, 1994,

Fischer, H., Wienhold, F. G., Hoor, P., Bujok, O., Schiller, C., Siegmund, P., Ambaum, M., Scheeren, H. A., and Lelieveld, J.: Tracer correlations in the northern high latitude lowermost stratosphere: Influence of cross-tropopause mass exchange, Geophysical Research Letters, 27, 97-100, 10.1029/1999gl010879, 2000.

Flohn, H.: Recent investigation on the mechanism of the "summer monsoon" of southern and eastern Asia, in: Proc. Symp. Monsoon of the World, 1960, 75-88,

Fu, R., Hu, Y., Wright, J. S., Jiang, J. H., Dickinson, R. E., Chen, M., Filipiak, M., Read, W. G., Waters, J. W., and Wu, D. L.: Short circuit of water vapor and polluted air to the global stratosphere by convective transport over the Tibetan Plateau,

Proceedings of the National Academy of Sciences of the United States of America, 103, 5664-5669, 10.1073/pnas.0601584103, 2006.

Garny, H., and Randel, W. J.: Dynamic variability of the Asian monsoon anticyclone observed in potential vorticity and correlations with tracer distributions, Journal of Geophysical Research: Atmospheres, 118, 13,421-413,433, 10.1002/2013jd020908, 2013.

Garny, H., and Randel, W. J.: Transport pathways from the Asian Monsoon Anticyclone to the Stratosphere, Draft for ACPD, 2015.

Gettelman, A., Hoor, P., Pan, L. L., Randel, W. J., Hegglin, M. I., and Birner, T.: The Extratropical Upper Troposphere and Lower Stratosphere, Reviews of Geophysics, 49, 10.1029/2011rg000355, 2011.

Goswami, B. N.: South Asian monsoon, in: Intraseasonal Variability in the Atmosphere-Ocean Climate System, 2nd ed., edited by: Lau, W. K. M., and Waliser, D. E., Springer-Verlag, Berlin, Heidelberg, 21–72, 2012.

Gottschaldt, K., Voigt, C., Jöckel, P., Righi, M., Deckert, R., and Dietmüller, S.: Global sensitivity of aviation NOx effects to the HNO3-forming channel of the HO2 + NO reaction, Atmospheric Chemistry and Physics, 13, 3003-3025, 10.5194/acp-13-3003-2013, 2013.

Gottschaldt, K., Schlager, H., Baumann, R., Bozem, H., Eyring, V., Hoor, P., Jöckel, P., Jurkat, T., Voigt, C., Zahn, A., and Ziereis, H.: Trace gas composition in the Asian summer monsoon anticyclone: a case study based on aircraft observations and model simulations, Atmospheric Chemistry and Physics, 17, 6091-6111, 10.5194/acp-17-6091-2017, 2017.

Grewe, V., Brunner, D., Dameris, M., Grenfell, J. L., Hein, R., Shindell, D., and Staehelin, J.: Origin and variability of upper tropospheric nitrogen oxides and ozone at northern mid-latitudes, Atmospheric Environment, 35, 3421-3433, 2001.

Grewe, V.: Impact of Lightning on Air Chemistry and Climate, in: Lightning: Principles, Instruments and Applications, edited by: Betz, H. D., Schumann, U., and Laroche, P., Springer Science+Business Media B. V., 537-549, 2009.

Grewe, V., Tsati, E., Mertens, M., Frömming, C., and Jöckel, P.: Contribution of emissions to concentrations: The TAGGING 1.0 submodel based on the Modular Earth Submodel System (MESSy 2.52), Geoscientific Model Development Discussions, 1-33, 10.5194/gmd-2016-298, 2017.

Grooß, J. U., Brühl, C., and Peter, T.: Impact of aircraft emissions on tropospheric and stratospheric ozone. Part 1: Chemistry and 2-d model results, Atmospheric Environment, 32, 3171-3184, 1998.

Holton, J. R., Haynes, P. H., McIntyre, M. E., Douglass, A. R., Rood, R. B., and Pfister, L.: Stratosphere-troposphere exchange, Reviews of Geophysics, 33, 403-439, 10.1029/95RG02097, 1995.

Hoor, P., Fischer, H., Lange, L., Lelieveld, J., and Brunner, D.: Seasonal variations of a mixing layer in the lowermost stratosphere as identified by the CO-O3correlation from in situ measurements, Journal of Geophysical Research, 107, 10.1029/2000jd000289, 2002.

Hoor, P., Gurk, C., Brunner, D., Hegglin, M. I., Wernli, H., and Fischer, H.: Seasonality and extent of extratropical TST derived from in-situ CO measurements during SPURT, Atmos. Chem. Phys., 4, 1427-1442, 10.5194/acp-4-1427-2004, 2004.

Hsu, C. J., and Plumb, R. A.: Nonaxisymmetric Thermally Driven Circulations and Upper-Tropospheric Monsoon Dynamics, J. Atmos. Sci., 57, 1255-1276, http://dx.doi.org/10.1175/1520-0469(2000)057<1255:NTDCAU>2.0.CO;2 2001.

IPCC: Climate Change 2013: The Physical Science Basis. Contribution of Working Group I to the Fifth Assessment Report of the Intergovernmental Panel on Climate Change, edited by: Stocker, T. F., Qin, D., Plattner, G.-K., Tignor, M., Allen, S. K., Boschung, J., Nauels, A., Xia, Y., Bex, V., and Midgley, P. M., Cambridge University Press, Cambridge, United Kingdom and New York, NY, USA,, 1535 pp., 2013.

Jaeglé, L., Jacob, D. J., Brune, W. H., Tan, D., Faloona, I. C., Weinheimer, A. J., Ridley, B. A., Campos, T. L., and Sachse, G. W.: Sources of HOxand production of ozone in the upper troposphere over the United States, Geophysical Research Letters, 25, 1709-1712, 10.1029/98gl00041, 1998.

Jöckel, P., Tost, H., Pozzer, A., Brühl, C., Buchholz, J., Ganzeveld, L., Hoor, P., Kerkweg, A., Lawrence, M., Sander, R., Steil, B., Stiller, G., Tanarhte, M., Taraborrelli, D., van Aardenne, J., and Lelieveld, J.: The atmospheric chemistry general circulation model ECHAM5/MESSy1: consistent simulation of ozone from the surface to the mesosphere, Atmos. Chem. Phys., 6, 5067-5104, 2006.

Jöckel, P., Kerkweg, A., Pozzer, A., Sander, R., Tost, H., Riede, H., Baumgaertner, A., Gromov, S., and Kern, B.: Development cycle 2 of the Modular Earth Submodel System (MESSy2), Geoscientific Model Development, 3, 717-752, 10.5194/gmd-3-717-2010, 2010.

Jöckel, P., Tost, H., Pozzer, A., Kunze, M., Kirner, O., Brenninkmeijer, C. A. M., Brinkop, S., Cai, D. S., Dyroff, C., Eckstein, J., Frank, F., Garny, H., Gottschaldt, K.-D., Graf, P., Grewe, V., Kerkweg, A., Kern, B., Matthes, S., Mertens, M., Meul, S., Neumaier, M., Nützel, M., Oberländer-Hayn, S., Ruhnke, R., Runde, T., Sander, R., Scharffe, D., and Zahn, A.: Earth System Chemistry integrated Modelling (ESCiMo) with the Modular Earth Submodel System (MESSy) version 2.51, Geoscientific Model Development, 9, 1153-1200, 10.5194/gmd-9-1153-2016, 2016.

Jurkat, T., Voigt, C., Kaufmann, S., Zahn, A., Sprenger, M., Hoor, P., Bozem, H., Müller, S., Dörnbrack, A., Schlager, H., Bönisch, H., and Engel, A.: A quantitative analysis of stratospheric HCl, HNO3, and O3in the tropopause region near the subtropical jet, Geophysical Research Letters, 41, 3315-3321, 10.1002/2013gl059159, 2014.

Jurkat, T., Kaufmann, S., Voigt, C., Schäuble, D., Jeßberger, P., and Ziereis, H.: The airborne mass spectrometer AIMS – Part 2: Measurements of trace gases with stratospheric or tropospheric origin in the UTLS, Atmospheric Measurement Techniques, 9, 1907-1923, 10.5194/amt-9-1907-2016, 2016.

Kaiser, J. W., Heil, A., Andreae, M. O., Benedetti, A., Chubarova, N., Jones, L., Morcrette, J. J., Razinger, M., Schultz, M. G., Suttie, M., and van der Werf, G. R.: Biomass burning emissions estimated with a global fire assimilation system based on observed fire radiative power, Biogeosciences, 9, 527-554, 10.5194/bg-9-527-2012, 2012.

Konopka, P., Grooß, J.-U., Günther, G., Ploeger, F., Pommrich, R., Müller, R., and Livesey, N.: Annual cycle of ozone at and above the tropical tropopause: observations versus simulations with the Chemical Lagrangian Model of the Stratosphere (CLaMS), Atmos. Chem. Phys., 10, 121-132, 10.5194/acp-10-121-2010, 2010.

Kunz, A., Sprenger, M., and Wernli, H.: Climatology of potential vorticity streamers and associated isentropic transport pathways across PV gradient barriers, Journal of Geophysical Research: Atmospheres, 120, 3802-3821, 10.1002/2014jd022615, 2015.

Kunze, M., Braesicke, P., Langematz, U., Stiller, G., Bekki, S., Brühl, C., Chipperfield, M., Dameris, M., Garcia, R., and Giorgetta, M.: Influences of the Indian Summer Monsoon on Water Vapor and Ozone Concentrations in the UTLS as Simulated by Chemistry–Climate Models, Journal of Climate, 23, 3525-3544, 10.1175/2010jcli3280.1, 2010.

Lawrence, M. G., and Lelieveld, J.: Atmospheric pollutant outflow from southern Asia: a review, Atmospheric Chemistry and Physics, 10, 11017-11096, 10.5194/acp-10-11017-2010, 2010.

Lelieveld, J., Crutzen, P. J., Ramanathan, V., Andreae, M. O., Brenninkmeijer, C. A. M., Campos, T., Cass, G. R., Dickerson, R. R., Fischer, H., de Gouw, J. A., Hansel, A., Jefferson, A., Kley, D., de Laat, A. T. J., Lal, S., Lawrence, M. G., Lobert, J. M., Mayol-Bracero, O. L., Mitra, A. P., Novakov, T., Oltmans, S. J., Prather, K. A., Reiner, T., Rodhe, H., Scheeren, H. A., Sikka, D., and Williams, J.: The Indian Ocean Experiment: Widespread Air Pollution from South and Southeast Asia, Science, 291, 1031-1036, 10.1126/science.1057103, 2001.

Lelieveld, J., Berresheim, H., Borrmann, S., Crutzen, P. J., Dentener, F. J., Fischer, H., Feichter, J., Flatau, P. J., Heland, J., Holzinger, R., Korrmann, R., Lawrence, M. G., Levin, Z., Markowicz, K. M., Mihalopoulos, N., Minikin, A., Ramanathan, V., de Reus, M., Roelofs, G. J., Scheeren, H. A., Sciare, J., Schlager, H., Schultz, M., Siegmund, P., Steil, B., Stephanou, E. G., Stier, P., Traub, M., Warneke, C., Williams, J., and Ziereis, H.: Global Air Pollution Crossroads over the Mediterranean, Science, 298, 794-799, 10.1126/science.1075457, 2002.

Lelieveld, J., Hoor, P., Jöckel, P., Pozzer, A., Hadjinicolaou, P., Cammas, J.-P., and Beirle, S.: Severe ozone air pollution in the Persian Gulf region, Atmos. Chem. Phys., 9, 1393-1406, 2009.

Li, Q., Jacob, D. J., Logan, J. A., Bey, I., Yantosca, R. M., Liu, H., Martin, R. V., Fiore, A. M., Field, B. D., Duncan, B. N., and Thouret, V.: A Tropospheric Ozone Maximum Over the Middle East, Geophysical Research Letters, 28, 3235-3238, 10.1029/2001gl013134
10.1029/2001GL013134, 2001.

Li, Q., Jiang, J. H., Wu, D. L., Read, W. G., Livesey, N. J., Waters, J. W., Zhang, Y., Wang, B., Filipiak, M. J., Davis, C. P., Turquety, S., Wu, S., Park, R. J., Yantosca, R. M., and Jacob, D. J.: Convective outflow of South Asian pollution: A global CTM simulation compared with EOS MLS observations, Geophysical Research Letters, 32, L14826, 10.1029/2005gl022762, 2005.

Lin, J.-L., Weickman, K. M., Kiladis, G. N., Mapes, B. E., Schubert, S. D., Suarez, M. J., Bacmeister, J. T., and Lee, M.-I.: Subseasonal Variability Associated with Asian Summer Monsoon Simulated by 14 IPCC AR4 Coupled GCMs, Journal of Climate, 21, 4541-4567, 10.1175/2008jcli1816.1, 2008.

Liu, J. J., Jones, D. B. A., Worden, J. R., Noone, D., Parrington, M., and Kar, J.: Analysis of the summertime buildup of tropospheric ozone abundances over the Middle East and North Africa as observed by the Tropospheric Emission Spectrometer instrument, Journal of Geophysical Research, 114, 10.1029/2008jd010993, 2009a.

Liu, J. J., Jones, D. B. A., Zhang, S., and Kar, J.: Influence of interannual variations in transport on summertime abundances of ozone over the Middle East, Journal of Geophysical Research, 116, 10.1029/2011jd016188, 2011.

Liu, Y., Wang, Y., Liu, X., Cai, Z., and Chance, K.: Tibetan middle tropospheric ozone minimum in June discovered from GOME observations, Geophysical Research Letters, 36, 10.1029/2008gl037056, 2009b.

Lopez, P.: A Lightning Parameterization for the ECMWF Integrated Forecasting System, Monthly Weather Review, 144, 3057-3075, 10.1175/mwr-d-16-0026.1, 2016.

Lubis, S. W., and Nakamura, N.: Stratospheric Influence on Summer Monsoon and Associated Planetary Wave Breaking and Mixing in the Subtropical Tropopause Region, AGU Fall Meeting, A51N-05, New Orleans, LA, 15 Dec., 2017.

Marcy, T. P., Fahey, D. W., Gao, R. S., Popp, P. J., Richard, E. C., Thompson, T. L., Rosenlof, K. H., Ray, E. A., Salawitch, R. J., Atherton, C. S., Bergmann, D. J., Ridley, B. A., Weinheimer, A. J., Loewenstein, M., Weinstock, E. M., and Mahoney, M. J.: Quantifying Stratospheric Ozone in the Upper Troposphere with in Situ Measurements of HCl, Science, 304, 261-265, 10.1126/science.1093418, 2004.

Müller, S., Hoor, P., Bozem, H., Gute, E., Vogel, B., Zahn, A., Bönisch, H., Keber, T., Krämer, M., Rolf, C., Riese, M., Schlager, H., and Engel, A.: Impact of the Asian monsoon on the extratropical lower stratosphere: trace gas observations during TACTS over Europe 2012, Atmospheric Chemistry and Physics, 16, 10573-10589, 10.5194/acp-16-10573-2016, 2016.

Nützel, M., Dameris, M., and Garny, H.: Movement, drivers and bimodality of the South Asian High, Atmospheric Chemistry and Physics, 16, 14755-14774, 10.5194/acp-16-14755-2016, 2016.

Pan, L. L., Randel, W. J., Gary, B. L., Mahoney, M. J., and Hintsa, E. J.: Definitions and sharpness of the extratropical tropopause: A trace gas perspective, Journal of Geophysical Research: Atmospheres, 109, n/a-n/a, 10.1029/2004jd004982, 2004.

Pan, L. L., Honomichl, S. B., Kinnison, D., Abalos, M., Randel, W. J., Bergman, J. W., and Bian, J.: Transport of chemical tracers from the boundary layer to stratosphere associated with the dynamics of the Asian summer monsoon, Journal of Geophysical Research: Atmospheres, 121, 1-16, 10.1002/2016JD025616, 2016.

Park, M., Randel, W. J., Emmons, L. K., Bernath, P. F., Walker, K. A., and Boone, C. D.: Chemical isolation in the Asian monsoon anticyclone observed in Atmospheric Chemistry Experiment (ACE-FTS) data, Atmos. Chem. Phys., 8, 757-764, 10.5194/acp-8-757-2008, 2008.

Park, M., Randel, W. J., Emmons, L. K., and Livesey, N. J.: Transport pathways of carbon monoxide in the Asian summer monsoon diagnosed from Model of Ozone and Related Tracers (MOZART), Journal of Geophysical Research, 114, D08303, 10.1029/2008jd010621, 2009.

Ploeger, F., Gottschling, C., Griessbach, S., Grooß, J. U., Guenther, G., Konopka, P., Müller, R., Riese, M., Stroh, F., Tao, M., Ungermann, J., Vogel, B., and von Hobe, M.: A potential vorticity-based determination of the transport barrier in the Asian summer monsoon anticyclone, Atmospheric Chemistry and Physics, 15, 13145-13159, 10.5194/acp-15-13145-2015, 2015.

Pokhrel, S., Chaudhari, H. S., Saha, S. K., Dhakate, A., Yadav, R. K., Salunke, K., Mahapatra, S., and Rao, S. A.: ENSO, IOD and Indian Summer Monsoon in NCEP climate forecast system, Climate Dynamics, 39, 2143-2165, 10.1007/s00382-012-1349-5, 2012.

Popovic, J. M., and Plumb, R. A.: Eddy Shedding from the Upper-Tropospheric Asian Monsoon Anticyclone, Journal of the Atmospheric Sciences, 58, 93-104, 10.1175/1520-0469(2001)058<0093:ESFTUT>2.0.CO;2, 2001.

Randel, W. J., and Park, M.: Deep convective influence on the Asian summer monsoon anticyclone and associated tracer variability observed with Atmospheric Infrared Sounder (AIRS), Journal of Geophysical Research, 111, D12314, 10.1029/2005jd006490, 2006.

Randel, W. J., Pan, L. L., and Bian, J.: Workshop on dynamics, transport and chemistry of the UTLS Asian Monsoon, Advances in Atmospheric Sciences, 33, 1096-1098, 10.1007/s00376-016-6169-9, 2016.

Rauthe-Schöch, A., Baker, A. K., Schuck, T. J., Brenninkmeijer, C. A. M., Zahn, A., Hermann, M., Stratmann, G., Ziereis, H., van Velthoven, P. F. J., and Lelieveld, J.: Trapping, chemistry, and export of trace gases in the South Asian summer monsoon observed during CARIBIC flights in 2008, Atmospheric Chemistry and Physics, 16, 3609-3629, 10.5194/acp-16-3609-2016, 2016.

Ren, R., Wu, G., Cai, M., Sun, S., Liu, X., and Li, W.: Progress in Research of Stratosphere-Troposphere Interactions: Application of Isentropic Potential Vorticity Dynamics and the Effects of the Tibetan Plateau, J. Meteor. Res., 28, 714-731, 10.1007 /s13351-014-4026-2, 2014.

Richards, N. A. D., Arnold, S. R., Chipperfield, M. P., Miles, G., Rap, A., Siddans, R., Monks, S. A., and Hollaway, M. J.: The Mediterranean summertime ozone maximum: global emission sensitivities and radiative impacts, Atmospheric Chemistry and Physics, 13, 2331-2345, 10.5194/acp-13-2331-2013, 2013.

Rodwell, M. J., and Hoskins, B. A.: Monsoons and the dynamics of deserts, Q. J. R. Meteorol. Soc., 122, 1385-1404, 10.1002/qj.49712253408, 1996.

Rogers, H., Teyssedre, H., Pitari, G., Grewe, V., van Velthoven, P., and Sundet, J.: Model intercomparison of the transport of aircraft-like emissions from sub- and supersonic aircraft, Meteorologische Zeitschrift, 11, 151-159, 10.1127/0941-2948/2002/0011-0151, 2002.

Safieddine, S., Boynard, A., Hao, N., Huang, F., Wang, L., Ji, D., Barret, B., Ghude, S. D., Coheur, P.-F., Hurtmans, D., and Clerbaux, C.: Tropospheric ozone variability during the East Asian summer monsoon as observed by satellite (IASI), aircraft (MOZAIC) and ground stations, Atmospheric Chemistry and Physics, 16, 10489-10500, 10.5194/acp-16-10489-2016, 2016.

Santee, M. L., Manney, G. L., Livesey, N. J., Schwartz, M. J., Neu, J. L., and Read, W. G.: A comprehensive overview of the climatological composition of the Asian summer monsoon anticyclone based on 10 years of Aura Microwave Limb Sounder measurements, Journal of Geophysical Research: Atmospheres, 122, 5491-5514, 10.1002/2016jd026408, 2017.

Scheeren, H. A., Lelieveld, J., Roelofs, G. J., Williams, J., Fischer, H., de Reus, M., de Gouw, J. A., Warneke, C., Holzinger, R., Schlager, H., Klüpfel, T., Bolder, M., van der Veen, C., and Lawrence, M.: The impact of monsoon outflow from India and Southeast Asia in the upper troposphere over the eastern Mediterranean, Atmos. Chem. Phys., 3, 1589-1608, 2003.

Schiller, C. L., Bozem, H., Gurk, C., Parchatka, U., Königstedt, R., Harris, G. W., Lelieveld, J., and Fischer, H.: Applications of quantum cascade lasers for sensitive trace gas measurements of CO, CH4, N2O and HCHO, Applied Physics B, 92, 419-430, 10.1007/s00340-008-3125-0, 2008.

Schuck, T. J., Brenninkmeijer, C. A. M., Baker, A. K., Slemr, F., von Velthoven, P. F. J., and Zahn, A.: Greenhouse gas relationships in the Indian summer monsoon plume measured by the CARIBIC passenger aircraft, Atmos. Chem. Phys., 10, 3965-3984, 2010.

Schumann, U., and Huntrieser, H.: The global lightning-induced nitrogen oxides source, Atmos. Chem. Phys., 7, 3823-3907, 2007.

Seinfeld, J. H., and Pandis, S. N.: Relative roles of VOC and NOx in ozone formation, in: Atmospheric Chemistry and Physics, John Wiley & Sons, New York, 209-303, 1998.

Seinfeld, J. H., and Pandis, S. N.: Atmospheric chemistry and physics : from air pollution to climate change, 2nd edition ed., John Wiley & Sons, Inc., Hoboken, New Jersey, 2006.

Sprung, D., and Zahn, A.: Acetone in the upper troposphere/lowermost stratosphere measured by the CARIBIC passenger aircraft: Distribution, seasonal cycle, and variability, Journal of Geophysical Research, 115, 10.1029/2009jd012099, 2010.

Stratmann, G., Ziereis, H., Stock, P., Brenninkmeijer, C. A. M., Zahn, A., Rauthe-Schöch, A., Velthoven, P. V., Schlager, H., and Volz-Thomas, A.: NO and NOy in the upper troposphere: Nine years of CARIBIC measurements onboard a passenger aircraft, Atmospheric Environment, 133, 93-111, 10.1016/j.atmosenv.2016.02.035, 2016.

Tiedtke, M.: A comprehensive mass flux scheme for cumulus parameterization in large-scale models, Mon. Weather. Rev., 117, 1179-1800, 1989.

Tost, H.: Global Modelling of Cloud, Convection and Precipitation Influences on Trace Gases and Aerosols, PhD, University Bonn, Bonn, 2006.

Tost, H., Jöckel, P., and Lelieveld, J.: Lightning and convection parameterisations – uncertainties in global modelling, Atmos. Chem. Phys., 7, 4553-4568, 2007.

Tyrlis, E., Škerlak, B., Sprenger, M., Wernli, H., Zittis, G., and Lelieveld, J.: On the linkage between the Asian summer monsoon and tropopause fold activity over the eastern Mediterranean and the Middle East, Journal of Geophysical Research: Atmospheres, 119, 3202-3221, 10.1002/2013jd021113, 2014.

Vogel, B., Günther, G., Müller, R., Grooß, J. U., Hoor, P., Krämer, M., Müller, S., Zahn, A., and Riese, M.: Fast transport from Southeast Asia boundary layer sources to northern Europe: rapid uplift in typhoons and eastward eddy shedding of the Asian monsoon anticyclone, Atmospheric Chemistry and Physics, 14, 12745-12762, 10.5194/acp-14-12745-2014, 2014.

Voigt, C., Jessberger, P., Jurkat, T., Kaufmann, S., Baumann, R., Schlager, H., Bobrowski, N., Giuffrida, G., and Salerno, G.: Evolution of CO2, SO2, HCl, and HNO3 in the volcanic plumes from Etna, Geophysical Research Letters, 41, 2196–2203, 10.1002/2013GL058974, 2014.

Yan, R.-C., Bian, J.-C., and Fan, Q.-J.: The Impact of the South Asia High Bimodality on the Chemical Composition of the Upper Troposphere and Lower Stratosphere, Atmospheric and Oceanic Science Letters, 4, 229-234, 2011.

Zahn, A., Weppner, J., Widmann, H., Schlote-Holubek, K., Burger, B., Kühner, T., and Franke, H.: A fast and precise chemiluminescence ozone detector for eddy flux and airborne application, Atmospheric Measurement Techniques, 5, 363-375, 10.5194/amt-5-363-2012, 2012.

Ziereis, H., Schlager, H., and Schulte, P.: Distributions of NO, NOx, and NOy in the upper troposphere and lower stratosphere between 28° and 61°N during POLINAT 2, Journal of Geophysical Research, 105, 3653-3664, 10.1029/1999JD900870, 2000.

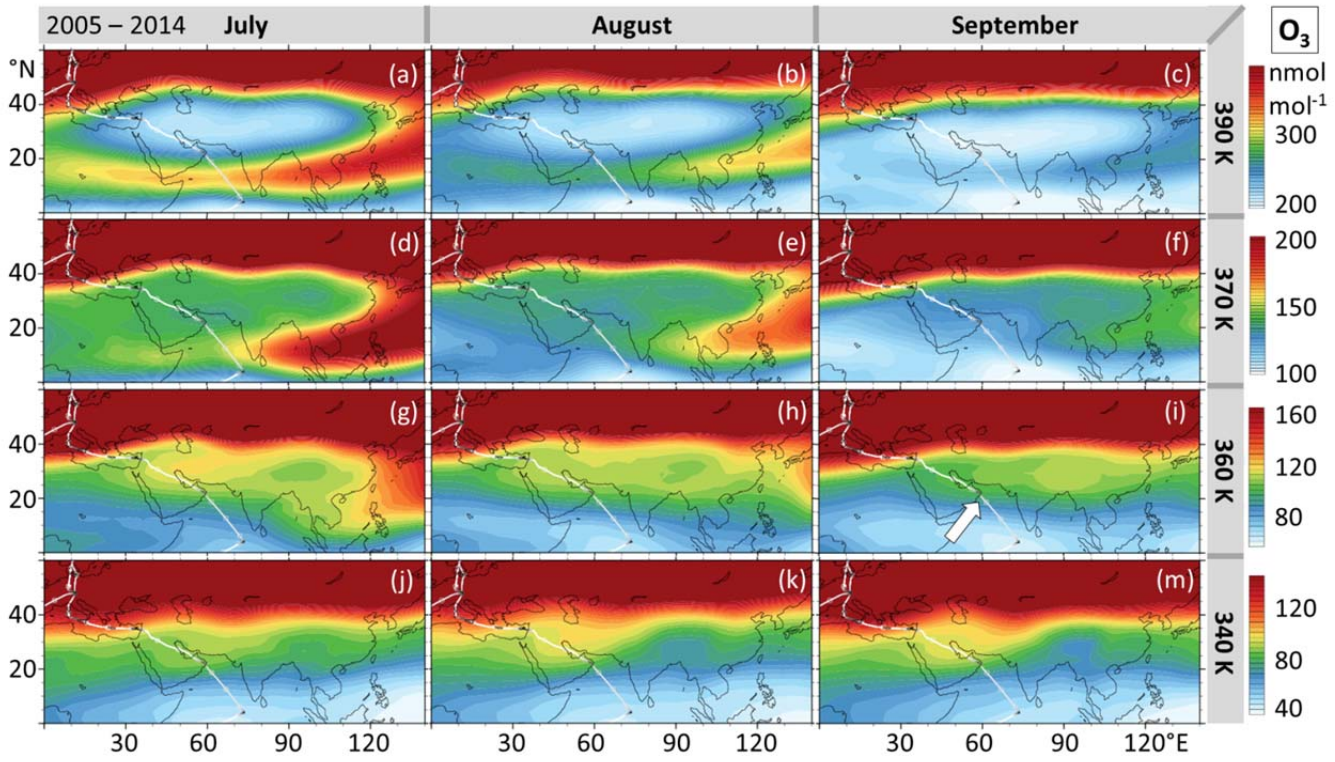

Figure 1. **EMAC simulated O_3 at different isentropic surfaces. Multi-annual monthly averages are calculated for the same period as in Santee et al. (2017) and agree well with their figures (370 K, 390 K). However, at the level corresponding to the HALO flight altitude (360 K), O_3 is enhanced in the ASMA in September (Panel i) and the observed sudden increase at the southern ASMA edge over Oman is also reproduced (arrow).**

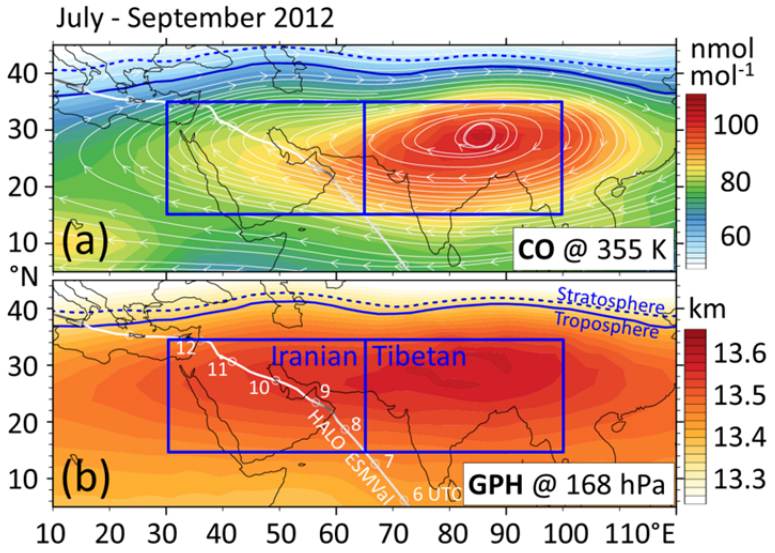

Figure 2. CO mixing ratios and geopotential height (GPH) as simulated by EMAC for the monsoon months of 2012. Enhanced CO is considered to be a chemical characteristic of the ASMA, and increased GPH is a dynamical proxy to delimit the ASMA. The Iranian and Tibetan domains are used throughout the paper to discuss differences between the convectively driven eastern part and the western part that is mainly controlled by UT transport. The Iranian region was traversed by the HALO ESMVal campaign during a flight from Male (Maldives) to Larnaca (Cyprus) on 18 September 2012. Beads show the HALO positions at full UTC hours, and the chosen isentropic (a) or pressure (b) levels roughly correspond to UT flight sections.

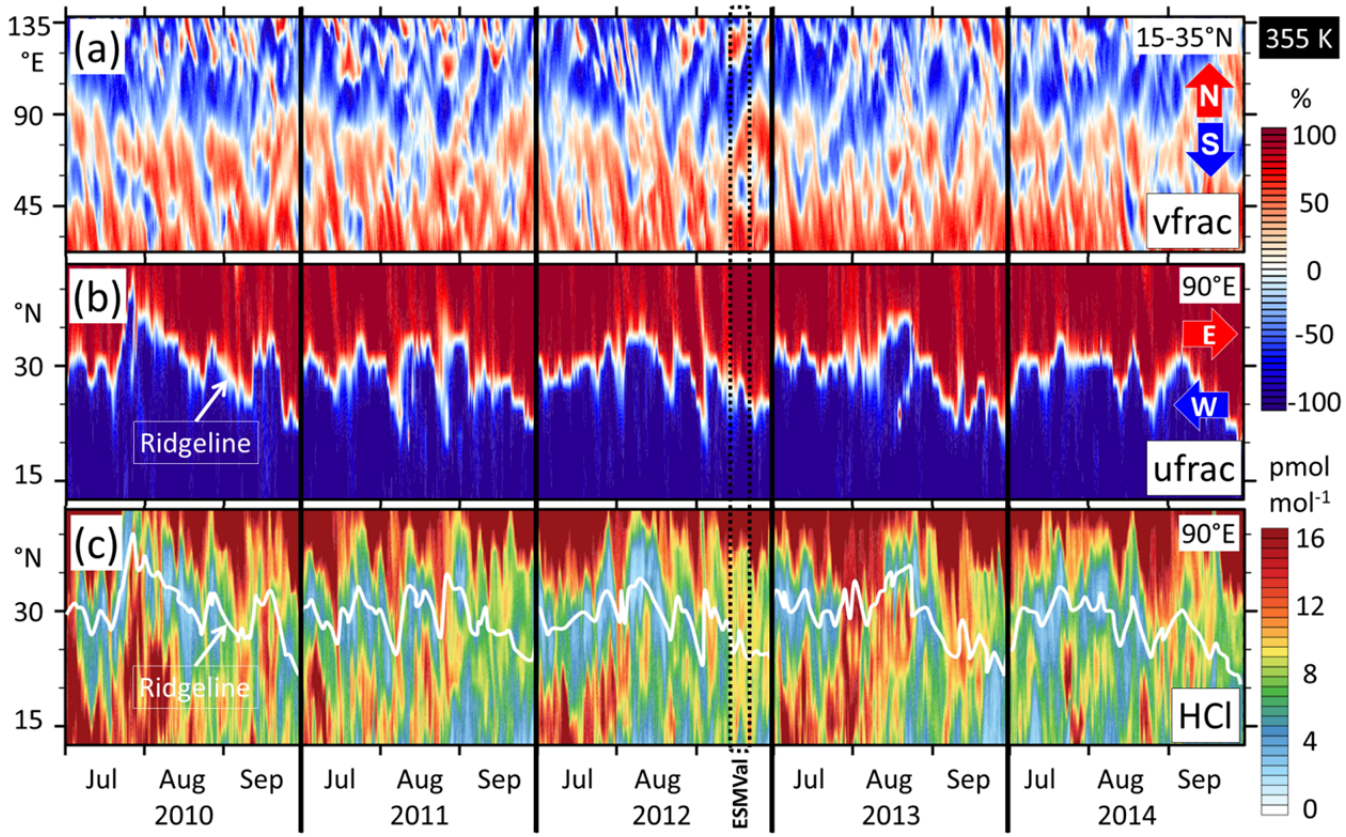

Figure 3. Exploratory analyses of the frequency of occurrence of (i) dynamical instabilities of the ASMA and (ii) transport of TL air in the free troposphere along the southern ASMA fringe. All panels show 10-hourly EMAC simulation results at the 355 K isentropic level, for the summer monsoon months in the ASMA region. (a) Meridional wind fraction (calculated as $v/\sqrt{u^2+v^2}$, with meridional velocity v, and zonal velocity u) along a wide zonal transect, averaged with dry grid cell mass weighting at each longitude from 15°N to 35°N. Blue shades indicate southward and red shades northward winds. Each red-blue pair (from west to east) at a given time marks an anticyclone or a smaller eddy. (b) As panel (a), but for zonal wind fraction ($u/\sqrt{u^2+v^2}$) along a meridional transect at 90°E. Blue shades indicate westward and red eastward winds. (c) Time evolution of HCl mixing ratios. At any given time, locally increased HCl south of the ridgeline is a proxy for air from the TL or the stratosphere.

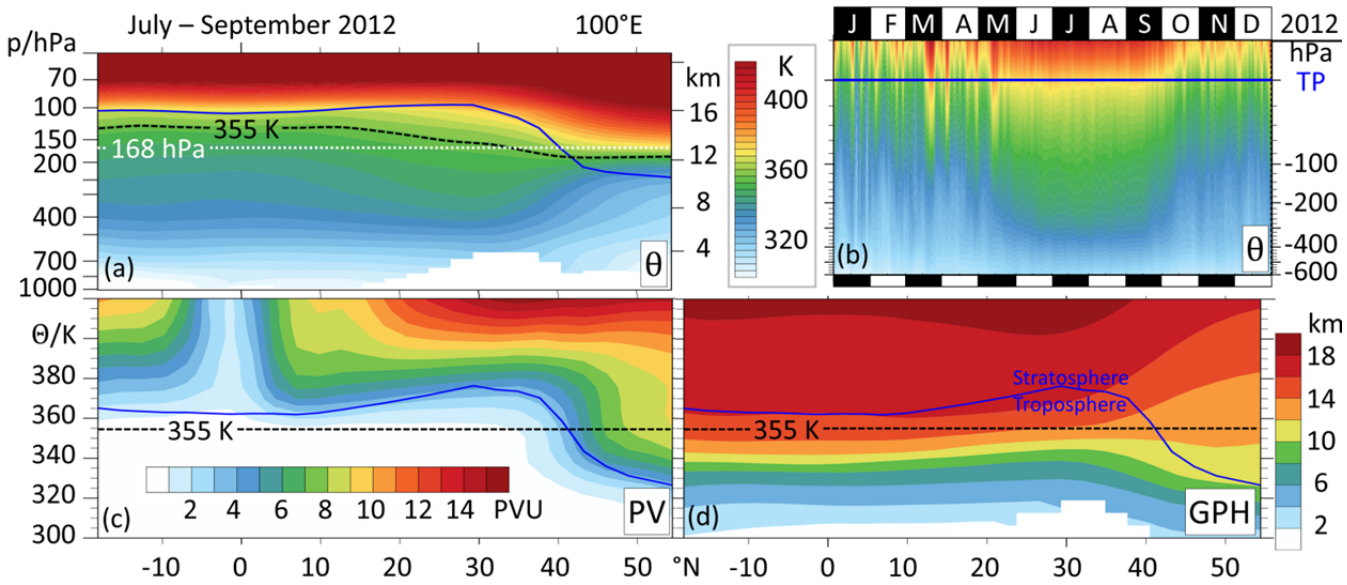

Figure 4. EMAC simulated relations between different parameters of the stratification of the atmosphere in the Tibetan region. Potential temperature (θ), potential vorticity (PV) and geopotential height (GPH) in curtains at 100°E. The levels of θ = 355 K and p = 168 hPa are chosen for horizontal slices in the paper. Panels (a), (c), (d) show time averages for the monsoon months of 2012. Panel (b) shows the evolution of θ profiles (grid-cell dry air mass weighted averages from 15 - 35°N, 65 – 100°E) throughout 2012 in pressure coordinates relative to tropopause (TP). Note the steeply inclining TP over the Tibetan plateau, which marks the transition from the extratropics (dominated by baroclinic wave activity and downward stratospheric circulation) to the tropics (dominated by radiative-convective balance and upward stratospheric circulation). Heating of the Tibetan plateau in summer brings UT isentropes closer to the surface (panel b), leading to intersections between the inclined TP and a range of isentropes (panel a).

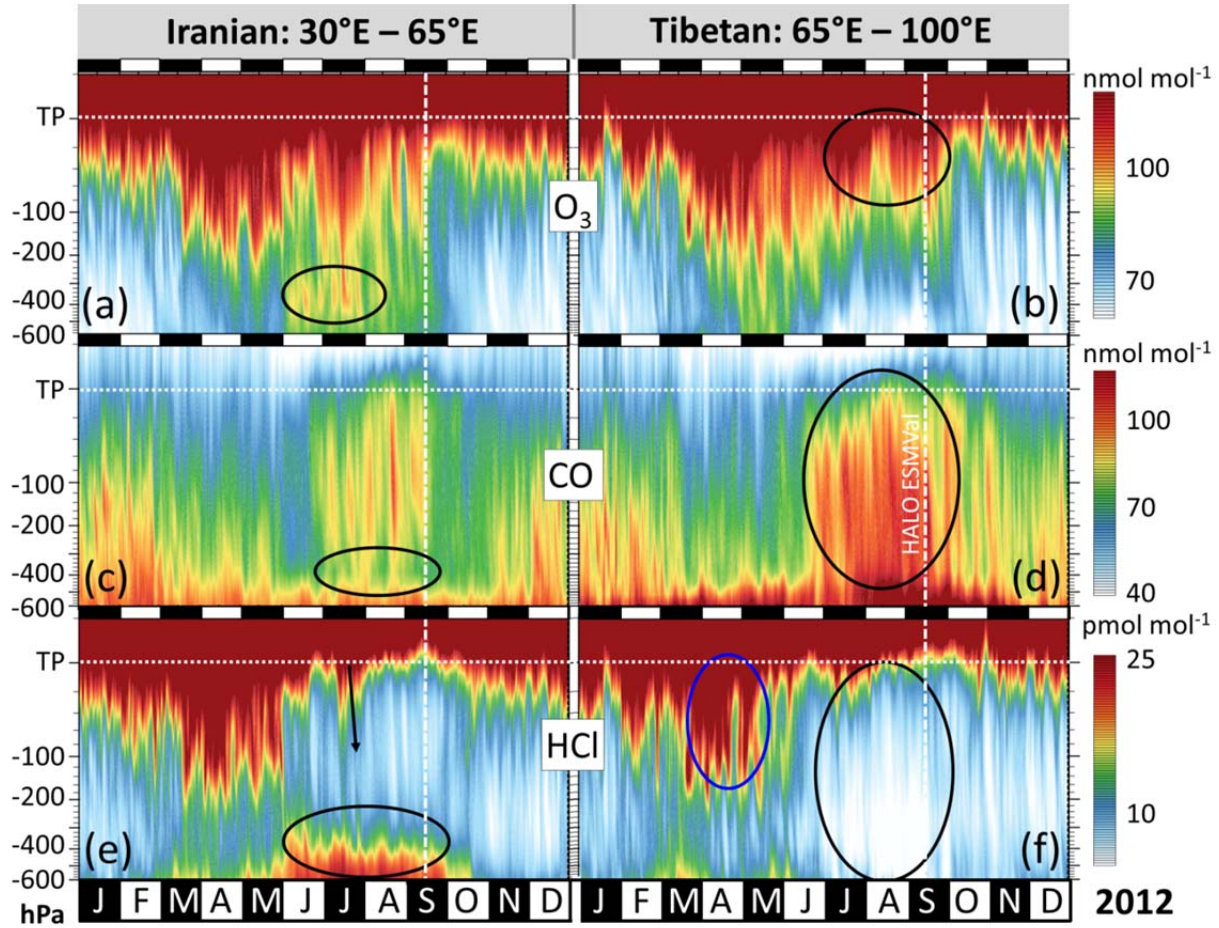

Figure 5. **Evolution of simulated trace gas profiles in the western and eastern ASMA regions throughout 2012. The time of the HALO ESMVal measurements is indicated by a dashed line. Vertical coordinates are given as pressure distance to the tropopause ("TP"), whose altitude depends on time and location. All values are grid-cell dry air mass weighted averages from 15°N to 35°N (see Fig. 2). Marked features are discussed in the text.**

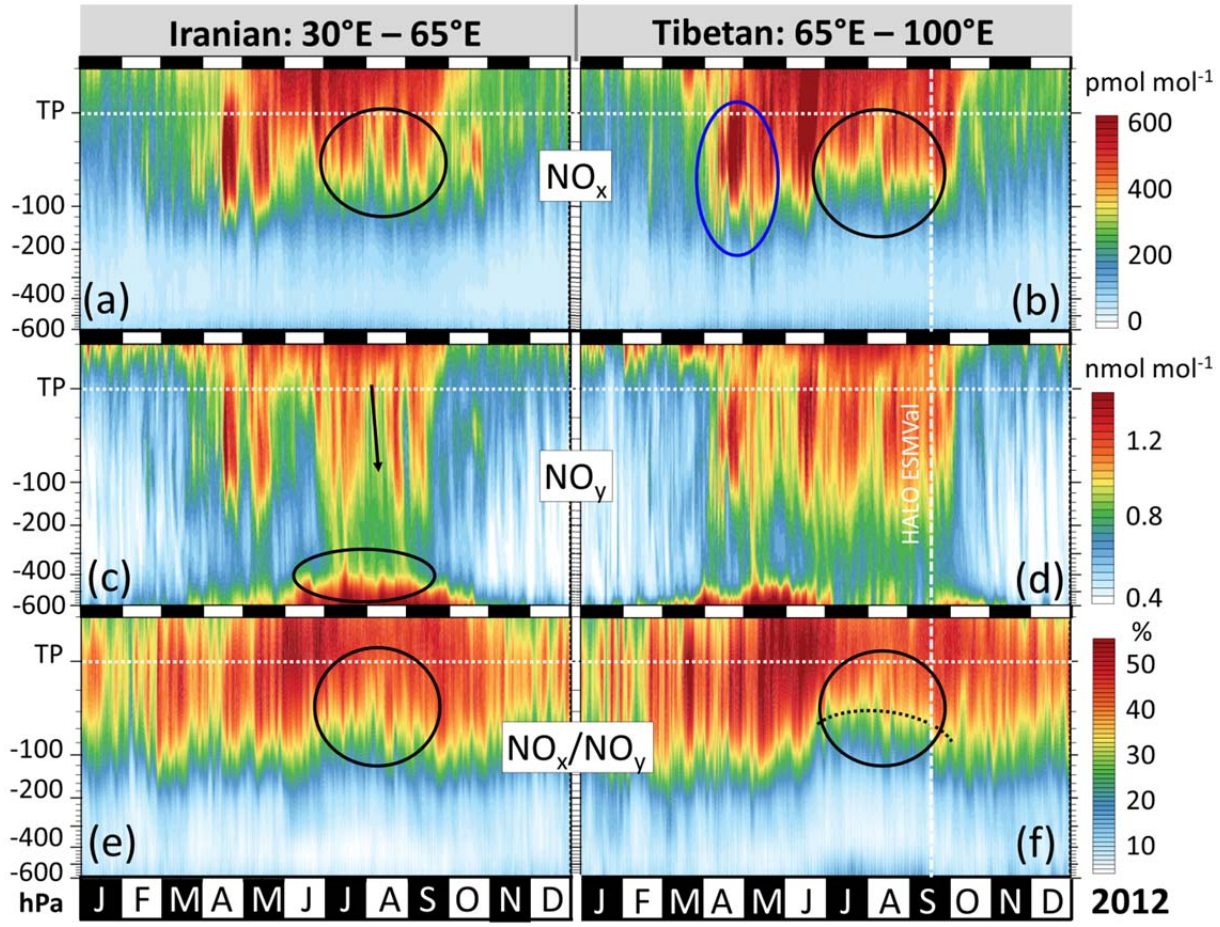

Figure 6. As Fig. 5, but focussing on reactive nitrogen. Examples of individual profiles from panels (c) and (d) are given in the supplement.

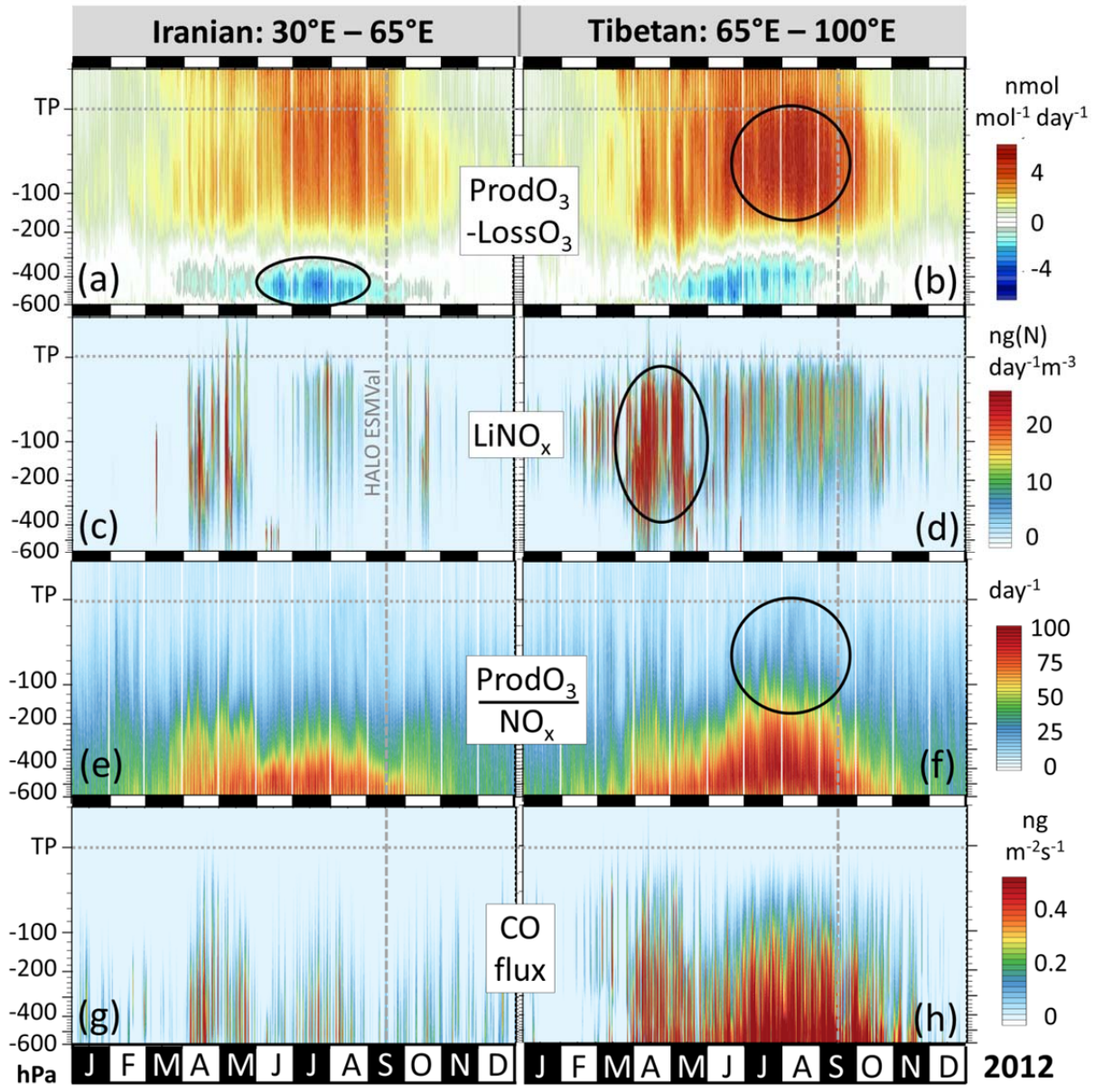

Figure 7. **As Fig. 5, but for different parameters related to net photochemical O_3 production ($ProdO_3$-$LossO_3$). Lightning NO_x ($LiNO_x$) emissions in the model are determined by parameterizations for convection, lightning and NO_x emissions per flash. "CO flux" reflects the concurrence of deep convective mass flux and CO mixing ratio, but as simple product of both does not account for entrainment and detrainment of convection. Panels (e) and (f) highlight the non-linear dependence of O_3 production on NO_x mixing ratios. Strong gradients indicate the transition between NO_x-limited and NO_x-saturated photochemical regimes, but are superimposed by the effects of other O_3 precursors. Individual profiles from panels (a) and (b) are shown in the supplement.**

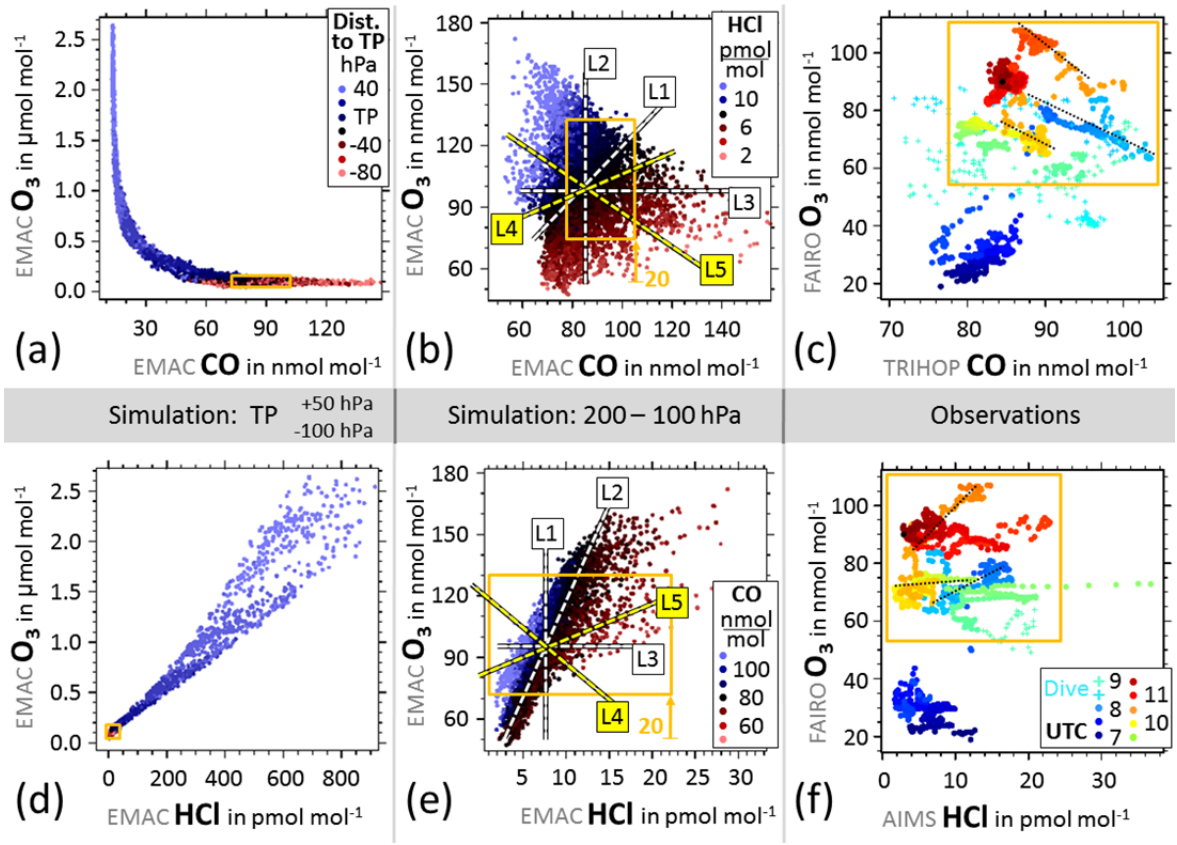

Figure 8. Tracer-tracer relations as simulated by EMAC for the entire September 2012 in the ASMA region, and as observed by HALO during the HALO ESMVal campaign on 18 September 2012. (a, d) Simulated samples from the region 15°N – 35°N, 30°E - 100°E. Colour coding corresponds to the pressure distance to the tropopause, from 100 hPa below to 50 hPa above. (b, e) Simulated tracer mixing ratios from the same region, but limited to tropospheric cells in the pressure altitude range 200 – 100 hPa. Colour coding indicates corresponding mixing ratios of HCl. See text for details of hypothetic lines L1 - L5. (c, f) Observed tracer mixing ratios of the HALO flight from Male to Larnaca (without initial and final stages). Colours correspond to the UTC time of measurement, also indicating spatial proximity. The orange boxes show the ranges covered by the measurements from within the ASMA.

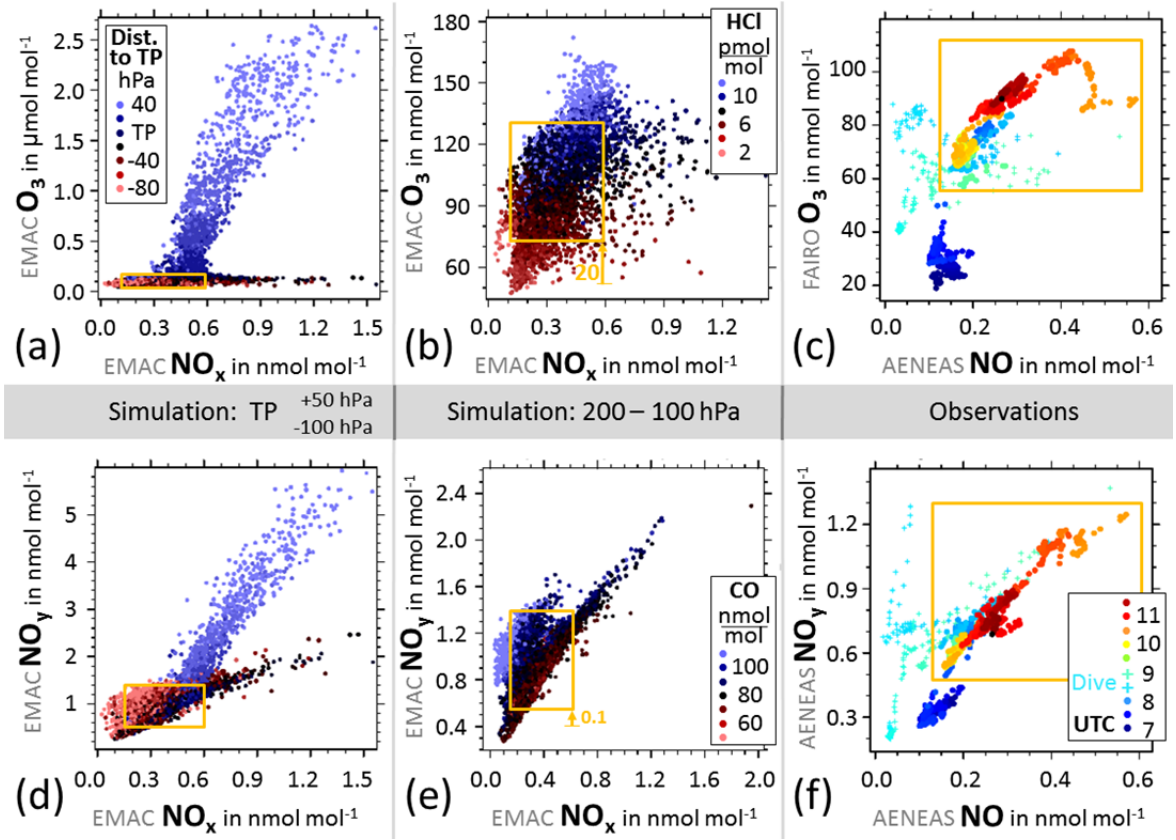

Figure 9. As Fig. 8, but focusing on reactive nitrogen. Panels (c) and (f) show NO instead of NO_x, because only NO was measured. At daytime, i.e. at the time of the measurements, NO is good proxy for NO_x. The legend from panel (a) also applies to (d), and the legend from (f) applies to (c).

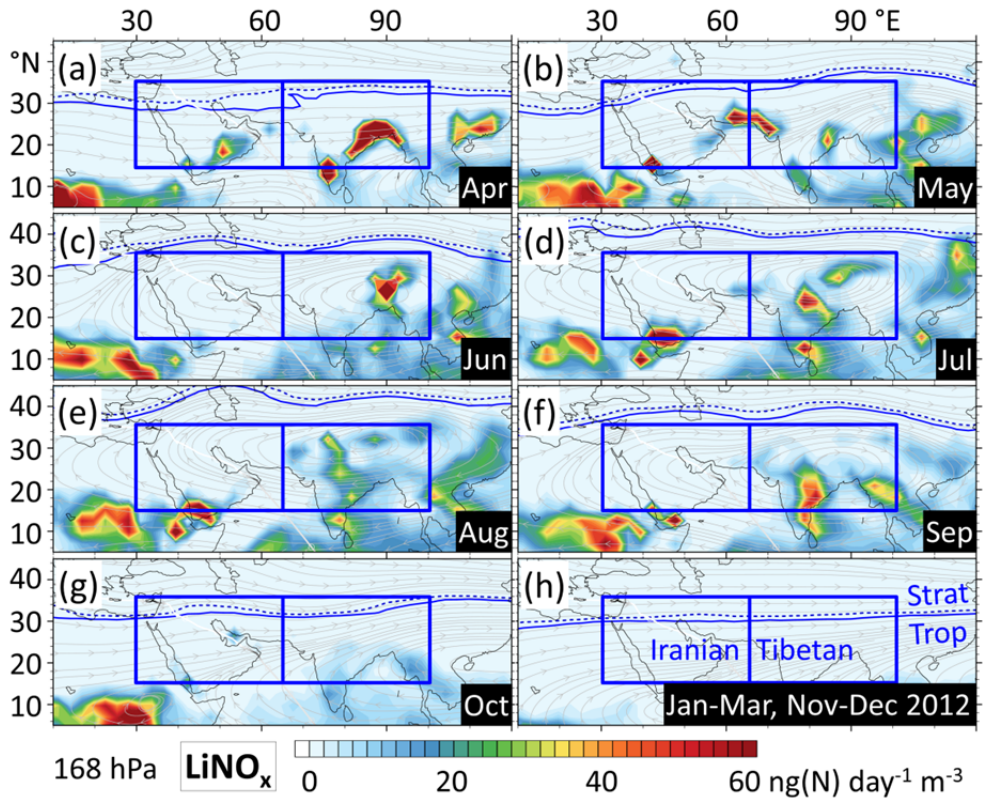

Figure 10. **Simulated monthly mean lightning NO_x emission rates in 2012 at a pressure level corresponding to the HALO ESMVal measurements. Months with almost no emissions are combined in panel (h). The ASMA circulation prints through in the monthly mean wind fields from June to September, as shown by streamlines (grey). There are strong, localised emissions in spring (Apr-May), which in the Iranian part hardly reach the 355 K level. In contrast, LiNOx emissions are distributed throughout the Tibetan region in summer (Jul-Sep). The simulated spatio-temporal emission patterns are similar for 2013 and 2014 (not shown).**

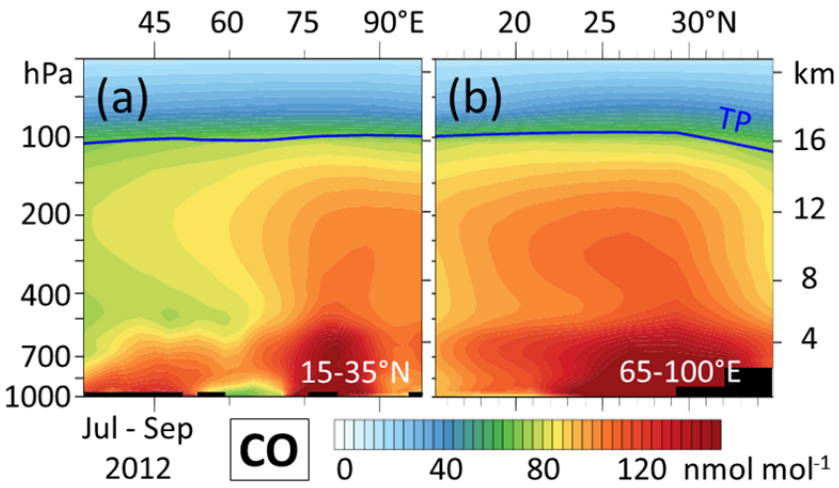

Figure 11. Simulated three-month mean curtains of CO mixing ratios: (a) Covering Iranian and Tibetan parts, meridional mean; (b) Tibetan part, zonal mean. On average, the hotspot of ascending CO in our simulation is located at about 29°N, 80°E, corresponding to the south-western flank of the Himalayas.

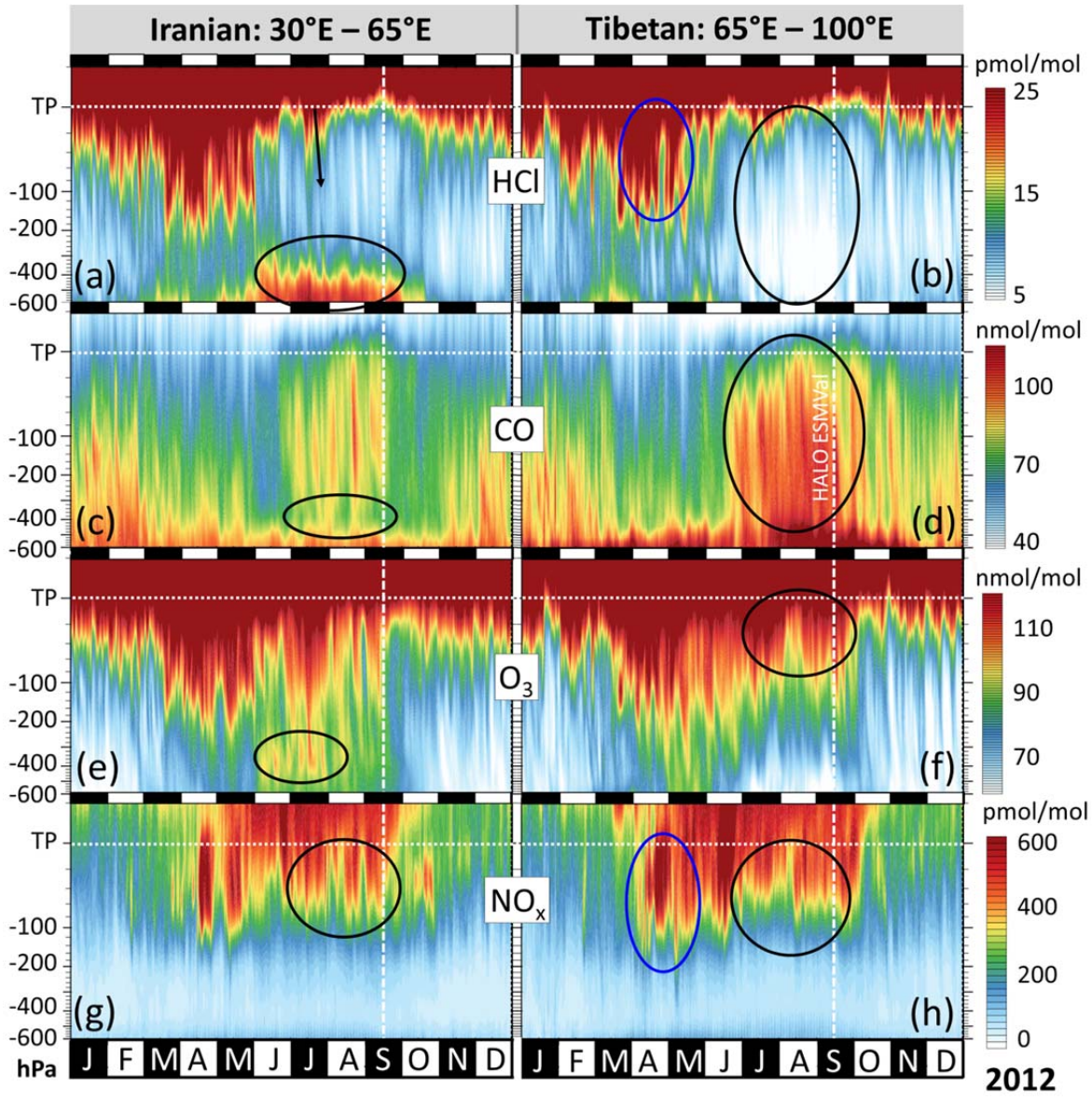

~~Figure #+4 Evolution of simulated trace gas profiles in the western and eastern ASMA regions throughout 2012. The time of the HALO ESMVal measurements is indicated by a dashed line. Vertical coordinates are given as pressure distance to the tropopause ("TP"), whose altitude depends on time and location. All values are grid-cell dry air mass weighted averages from 15°N to 35°N (see Fig. 1). Marked features are discussed in the text.~~

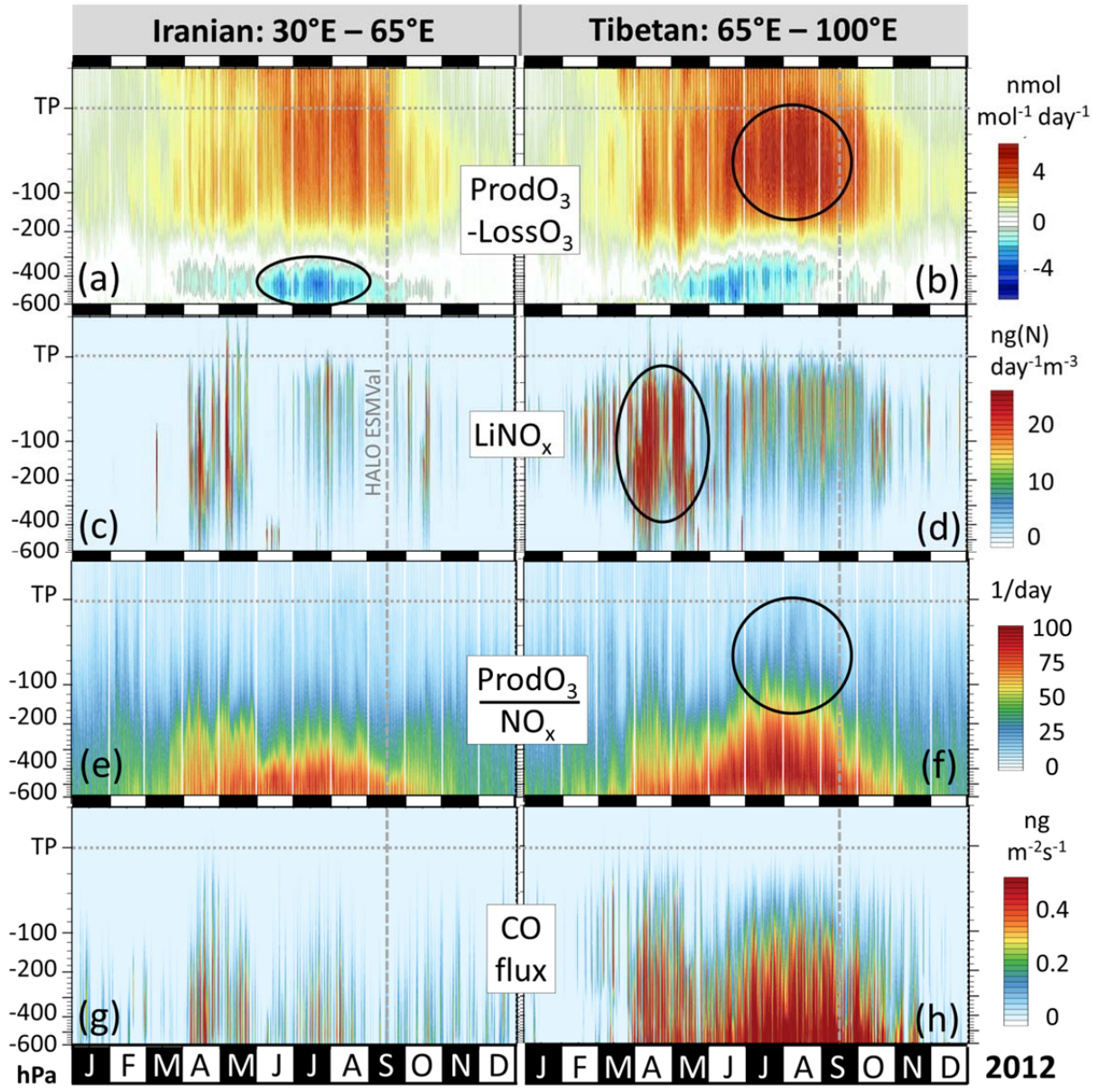

~~Figure 5. As Fig. 4, but for different parameters related to net photochemical O_3 production ($ProdO_3$-$LossO_3$). Lightning NO_x ($LiNO_x$) emissions in the model are determined by parameterizations for convection, lightning and NO_x emissions per flash. "CO flux" reflects the tempo-spatial concurrence of deep convective mass flux and CO mixing ratio, but as simple product of both does not account for entrainment and detrainment of convection. Panels (e) and (f) highlight the non-linear dependence of O_3 production on NO_x mixing ratios. Strong gradients indicate the transition between NO_x-limited and NO_x-saturated photochemical regimes, but are superimposed by the effects of other O_3 precursors. Individual profiles from panels (a) and (b) are shown in the supplement (Fig. S8).~~

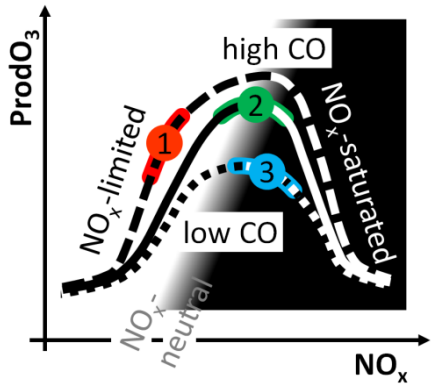

Figure 12. Schematic of the dependence of photochemical O_3 production ($ProdO_3$) on NO_x and CO mixing ratios (after Grooß et al. (1998). Red, green and blue highlight photochemical conditions that are discussed in the text. Approximate numbers (Ehhalt and Rohrer, 1994; Jaeglé et al., 1998; Grooß et al., 1998): For UT conditions at northern mid latitudes the point of maximum O_3 production may vary between 200 and 700 ~~n~~pmol ~~/~~mol^{-1} NO_x. The maximum net O_3 production varies by a factor of about 4, depending on ambient conditions.

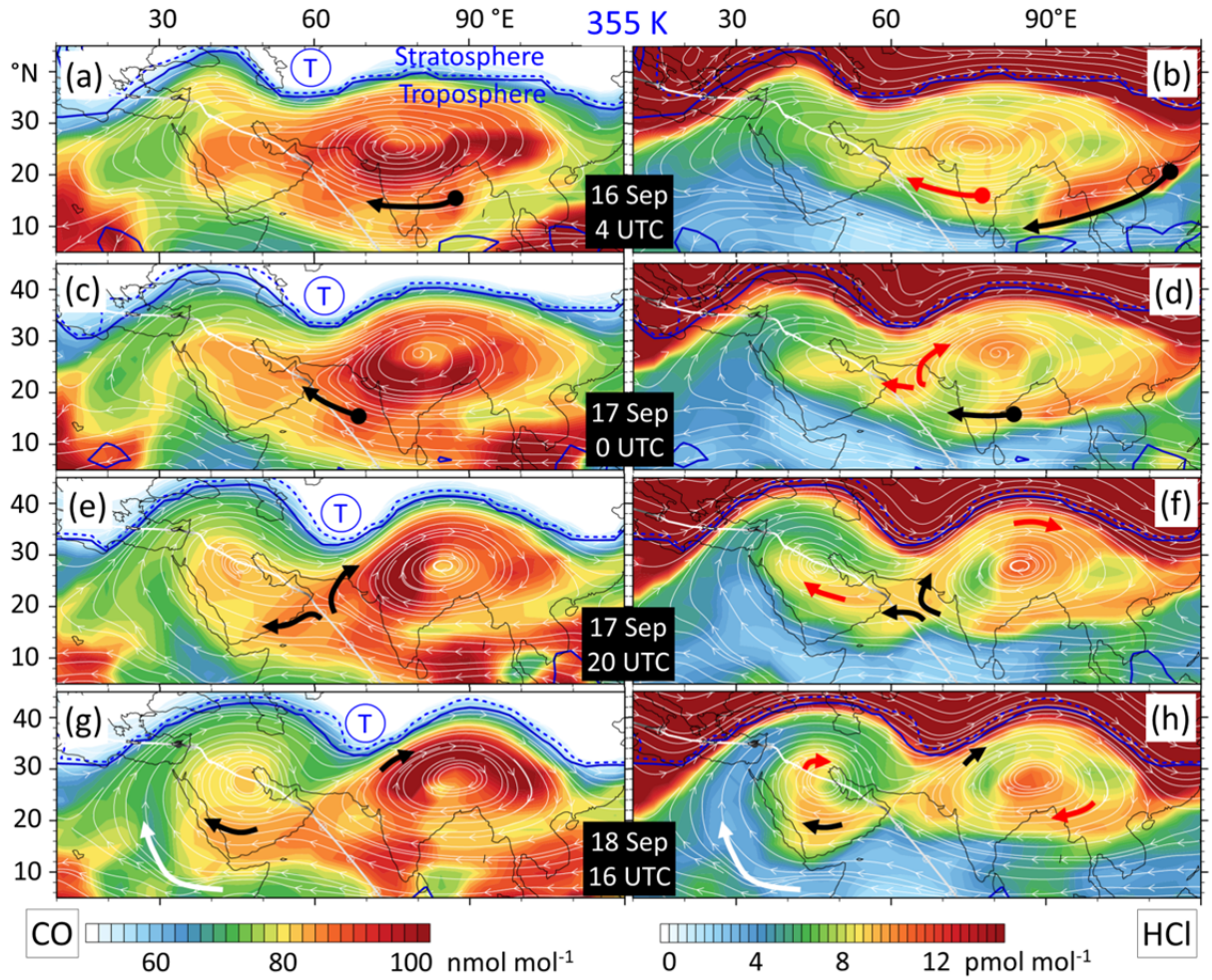

Figure 13. Sequence of simulated tracer fields at 355 K, illustrating the stirring associated with the splitting-up event of the ASMA that occurred during the HALO ESMVal campaign in September 2012. Streamlines represent instantaneous wind fields, and arrows highlight the redistribution of selected air masses. CO mainly originates in the ASMA interior and HCl serves as a proxy to track the ASMA fringe. The sequence starts with an elongated anticyclone on 16 September 2012. Then a tropopause trough (T) evolves from the west along the northern ASMA flank. The anticyclone succumbs to the perturbation and splits up into a Tibetan and an Iranian part, shortly after the HALO flight from Male to Larnaca had passed through. A part of the increased CO interior region is entrained by the outer streamlines of the Iranian part, while the rest of the patch is diverted into the interior of the Tibetan anticyclone (black arrows in the left panels). The evolution of freshly entrained HCl (black arrows) and an older patch (red arrows) are shown in the right panels. We also note entrainment of tropospheric air by southerly winds at the western flank (white arrows).

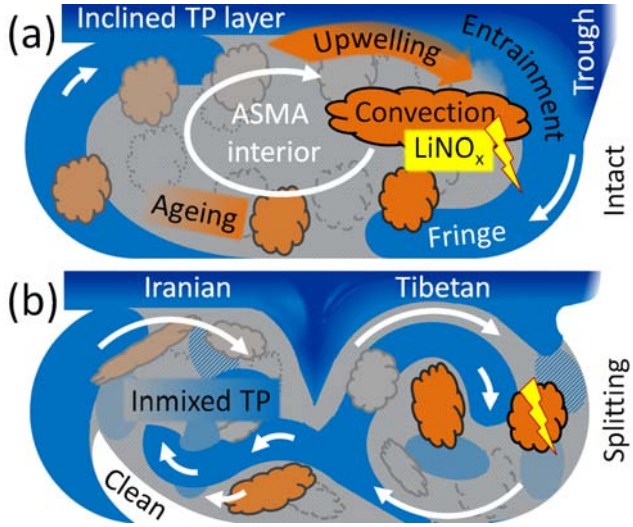

Figure 14. Schematics of processes determining trace gas distributions in the ASMA at an UT level: (a) One undisturbed anticyclone, encompassing the Tibetan and Iranian regions; (b) Splitting into an Iranian and a Tibetan part. See text for details.

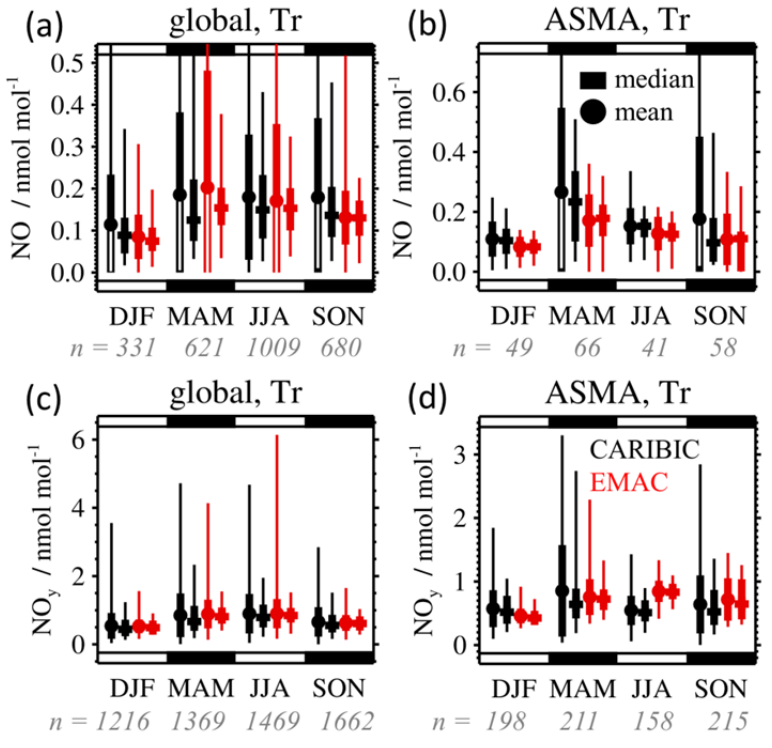

~~**Figure A2. Comparison of IAGOS-CARIBIC (black) measurements in the altitude range between 300 hPa and the TP ("Tr") with corresponding results of the EMAC RC1SD-base-10a simulation (red) for (a) NO globally, (b) NO in the ASMA region (15-35°N, 30-100°E), (c) NO_y globally, (d) NO_y in the ASMA region. All data stem from the period May 2005 to April 2014. The simulation was sampled along the IAGOS-CARIBIC flight tracks with a resolution of 12 min, and IAGOS-CARIBIC observations were subsequently interpolated (interval mean) to a resolution of 12 min. Numbers n below the plots show the number of the remaining data pairs (after interpolation and filtering) available for the respective seasons. Dots represent mean values, whiskers indicate standard deviation, min & max values. Rectangles represent the median, and whiskers the percentiles 5, 25, 75, 95.**~~

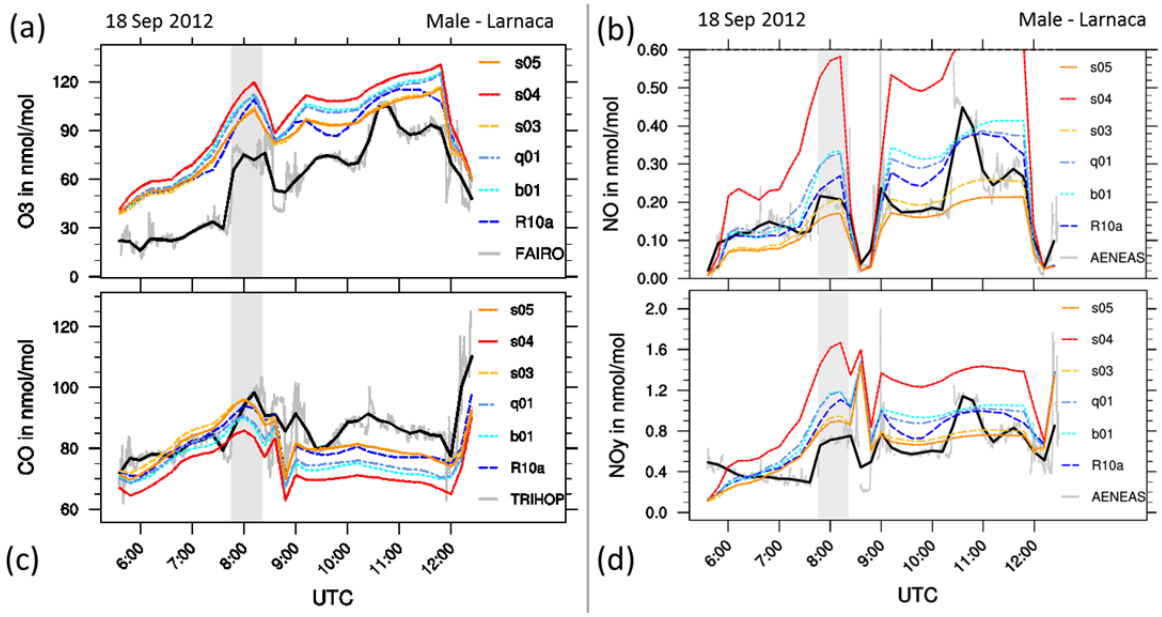

~~**Figure A3. Mixing ratios of O_3, CO, NO and NO_y along the HALO flight track from Male to Larnaca, on 18 September 2012. Grey shading marks the first flight section in ASMA air. Grey line: in situ measurements in 10 s resolution, black: in situ averaged to 12 min simulation time steps, R10a: EMAC simulation RC1SD-base-10a. Sensitivity simulations are based on the almost identical RC1SD-base-10 simulation of (Jöckel et al., 2016), feature daily instead of monthly biomass burning emissions, and were performed in quasi chemistry transport model mode (Deckert et al., 2011) to facilitate isolating the effects of modified emissions.**~~

~~**b01: as R10a, but with different traffic and different biomass burning emissions;**~~

~~**q01: as b01, but QCTM;**~~

~~**s03: as q01, but halved $LiNO_x$ emissions;**~~

~~**s04: as q01, but doubled $LiNO_x$ emissions;**~~

~~**s05: as s03, but with a different vertical emission profile of $LiNO_x$ (emission factors not decreased in the mid-troposphere, i.e. no C-shape)**~~

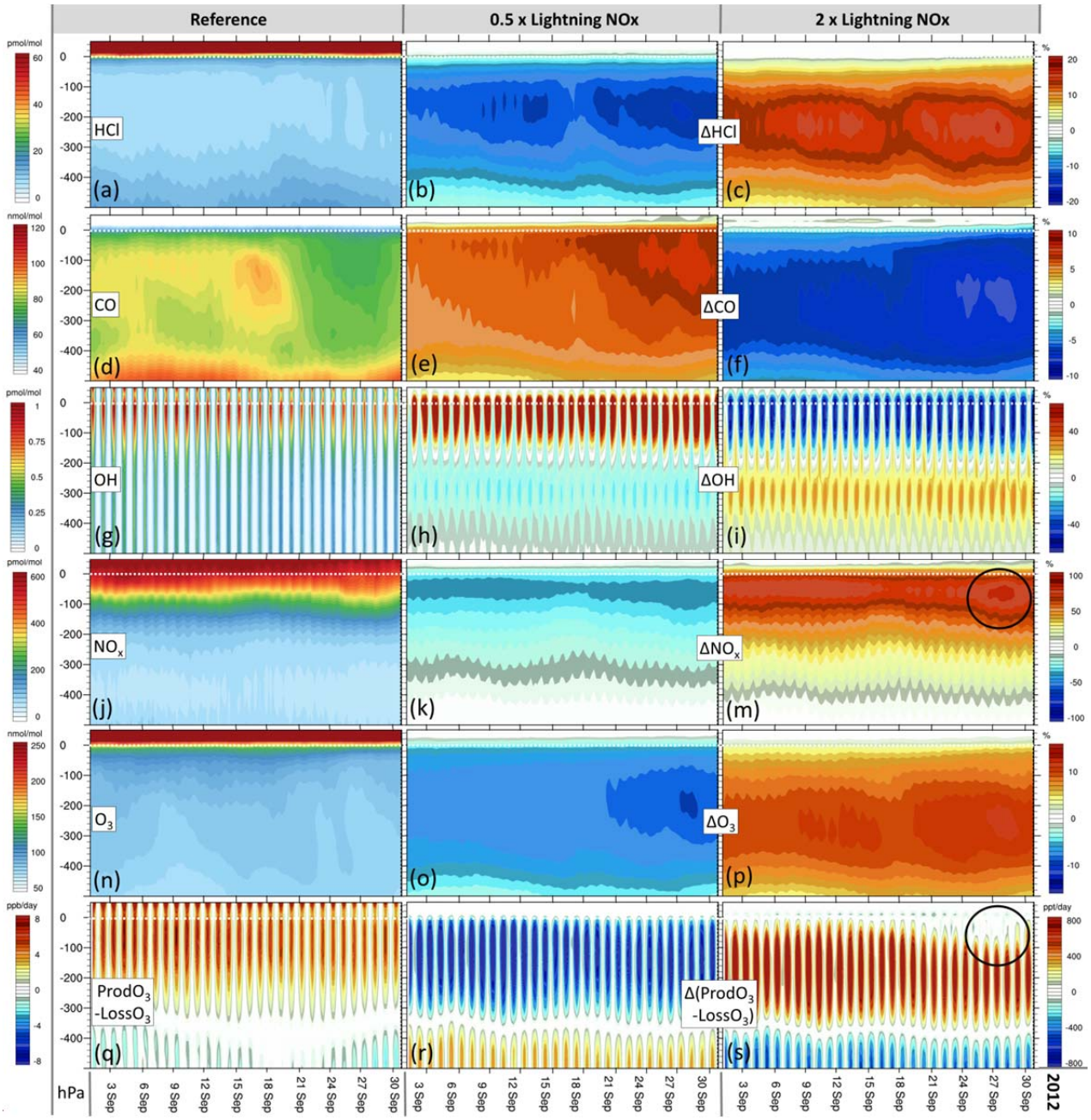

~~Figure A4. Evolution of simulated trace gas profiles and related diagnostics during September 2012 in the ASMA region (15° N – 35° N, 30° E – 100° E), and their sensitivity to LiNO$_x$ emissions. The vertical axes cover the UTLS and middle troposphere, and their coordinates are given as pressure distance to the tropopause. Left column: QCTM reference simulation (q01). Middle column: s03 – q01, relative deviation of sensitivity simulation s03 wrt. q01 for trace gases, absolute deviation for net O$_3$ production. Right column: s04 – q01.~~

~~Figure 14. S~~

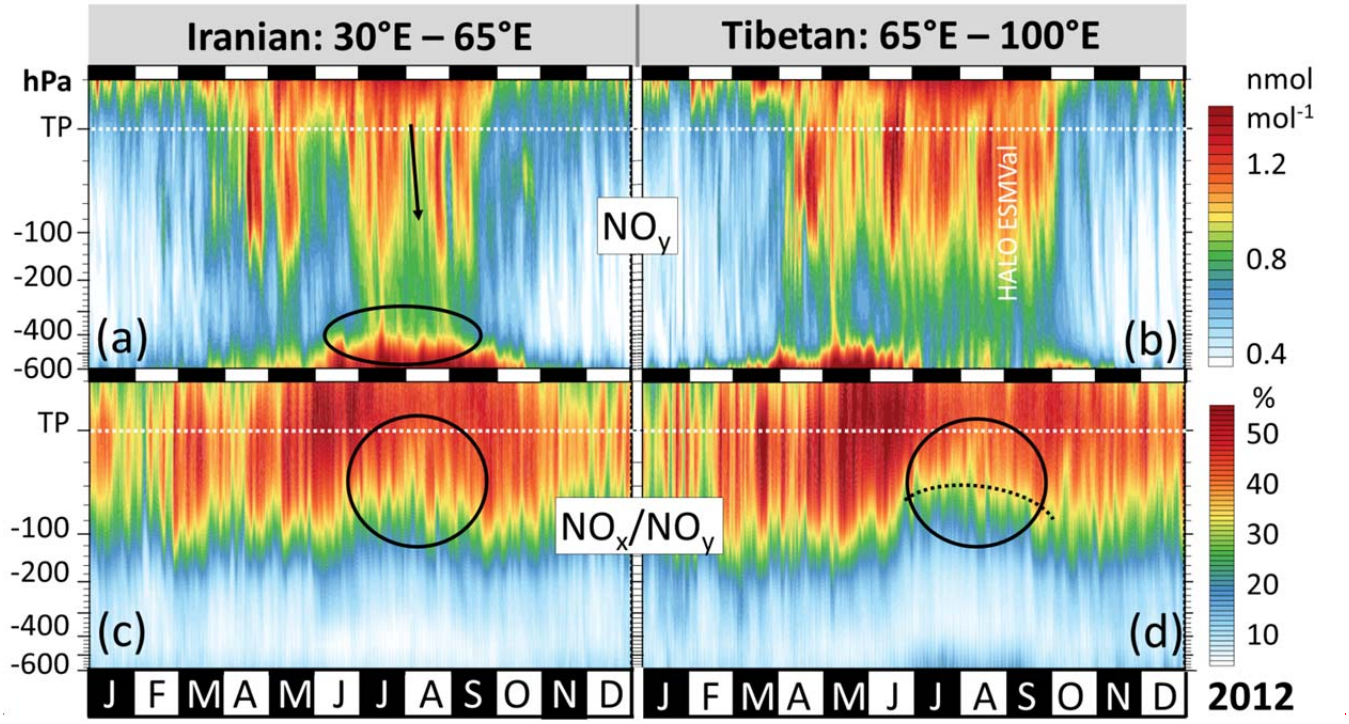

~~Figure B1. As Fig. 4, but focussing on reactive nitrogen.~~

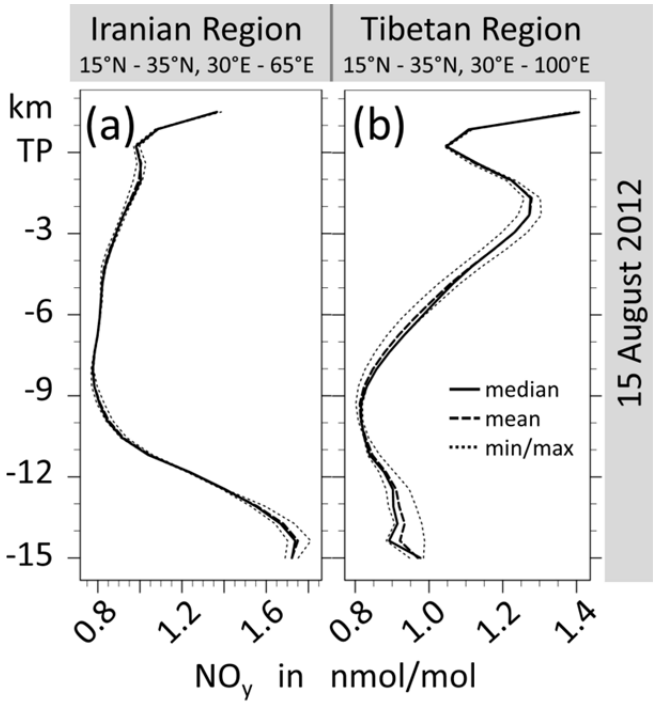

Figure B2. Simulated profiles of NO_y as simulated for 15 August 2012. These are examples of a C-shaped profile in the Iranian region (a) and an E-shaped profile in the Tibetan region (b).

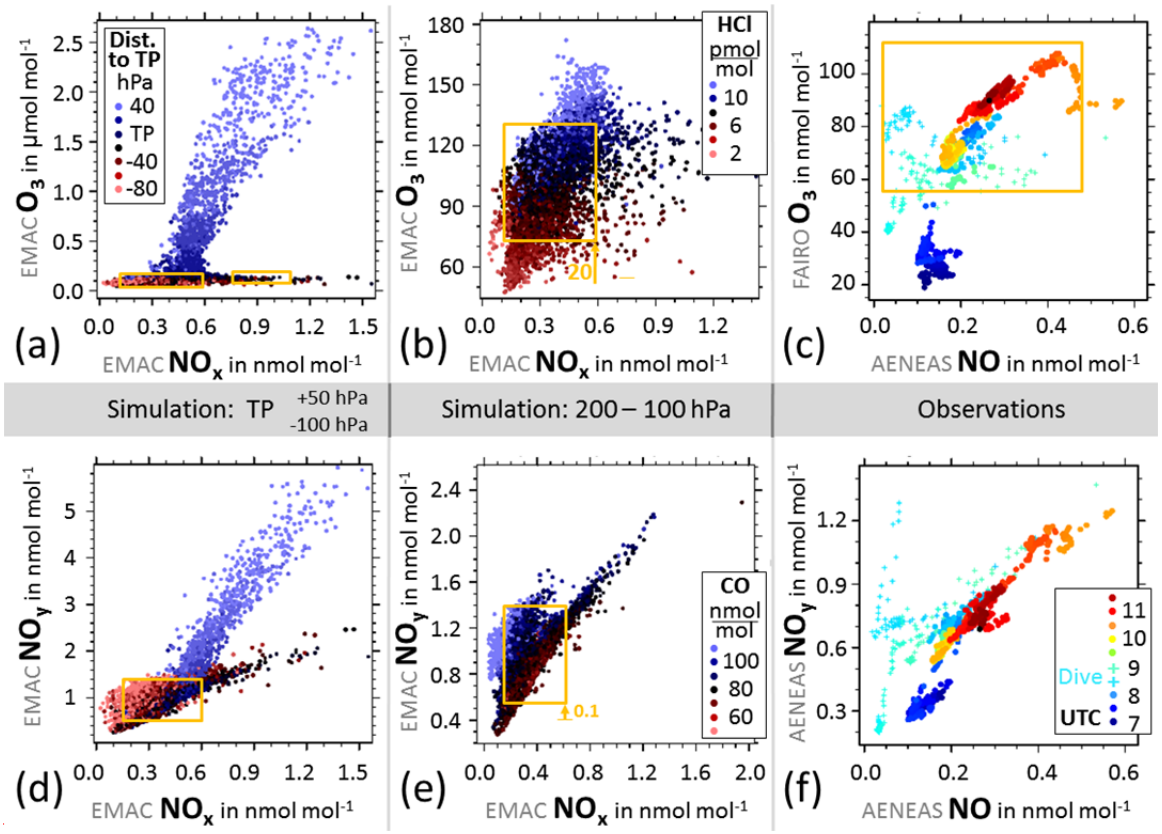

~~**Figure B3. As Fig. 3, but focusing on reactive nitrogen. Panels (c) and (f) show NO instead of NO_x, because only NO was measured. At daytime, i.e. at the time of the measurements, NO is good proxy for NO_x.**~~

Contents

S1 Tracer-tracer diagrams

S1.1 Primer

Tracer-tracer diagrams show mixing ratios of two species encountered simultaneously and are a standard method for analyzing mixing processes in the UTLS region (e.g. Zahn et al., 2000; Vogel et al., 2011). Sampling of two different air masses that are in the process of mixing is indicated by a mixing line in the tracer-tracer diagram. The slope of the mixing line provides additional clues about the origin of the original air parcels ("end-members"). If the ratios of the end members remain constant over time, the slope of the mixing line is conserved, as long as the mixing process continues. If the mixing processes stops, the mixing lines converge to a single point in the tracer-tracer diagram. If the reservoir of one end-member is bigger than the other, points in the tracer-tracer diagram will be close to the dominating end-member. However, the relative size of the reservoirs does not affect the slope of mixing lines, thus allowing detection of even small entrainments. Slopes change in case of mixing ratio changes over time (e.g. via in situ production or loss) of one or both reservoirs. Different effects may lead to similar tracer-tracer relations, resulting in ambiguity when trying to reconstruct end-members or disentangling mixing and chemical effects. Furthermore, mixing lines in general exist in a multi-dimensional tracer space, and thus lines in a tracer-tracer plot need to be considered as projections onto 2d space. They might also be the result of mixing between more than two reservoirs. Additional dimensions (tracers) need to be considered to reduce ambiguities.

S1.2 Potential temperatures of the observations

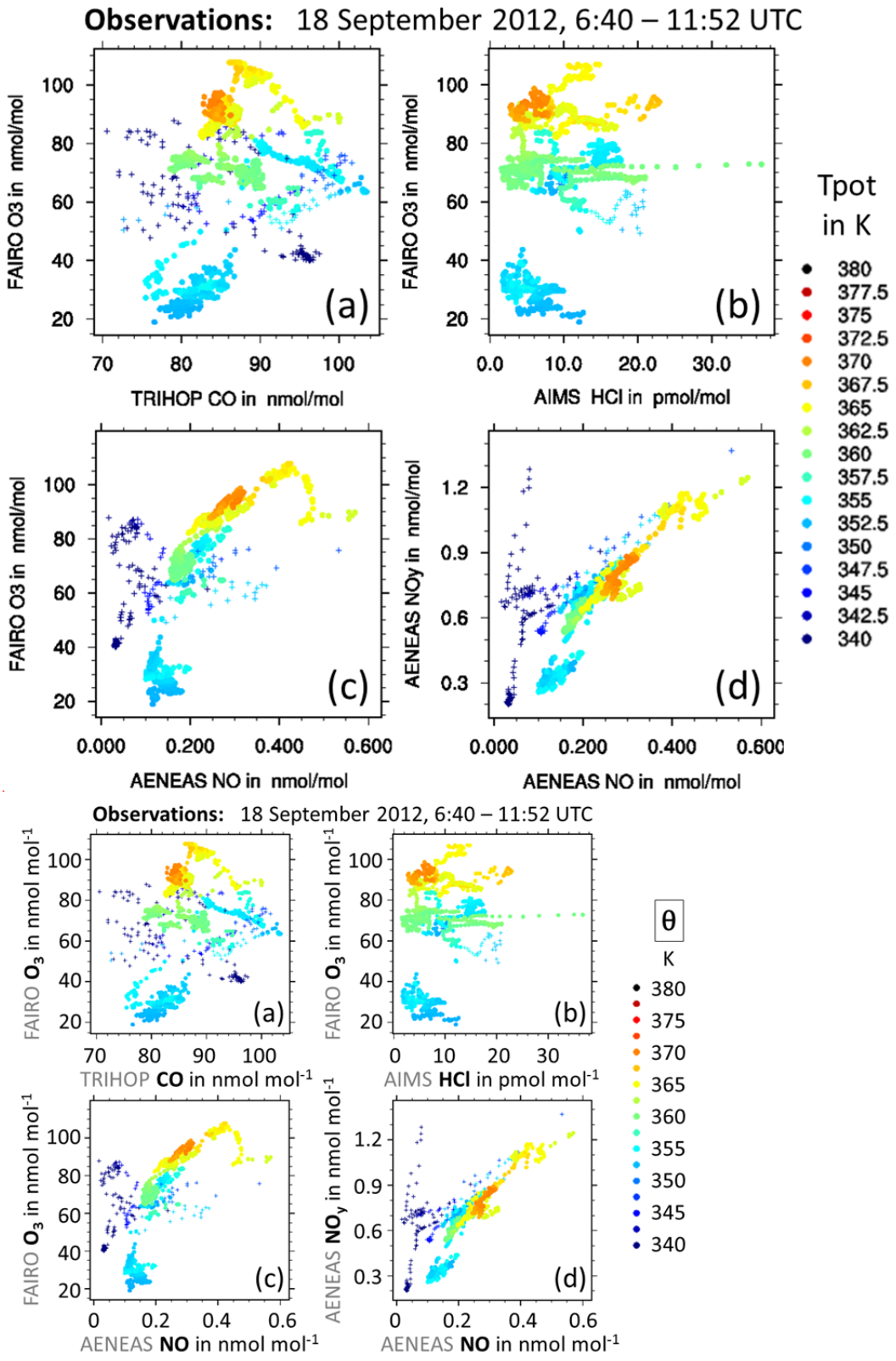

Figure S1. Measured data from the HALO ESMVal flight from Male to Larnaca. In contrast to Figs. 8cf, 9cf the samples here are color coded by their potential temperatures. During the dive (HALO descended from the upper to the lower troposphere and back to obtain profiles; indicated by crosses) potential temperatures were lower than shown, but the color scale is cut off at 340 K.

S2 Observations and model evaluation

S2.1 Simulated versus observed lightning activity

Convection is not explicitly resolved in the simulation, and the parameterizations for convection and lightning both introduce uncertainties to the simulation results for lightning. Uncertainties in the observations are due to a space- and time-dependent detection limit of 69% to 88%, and the application of a 3 month smoothing. Considering those uncertainties, the match between simulated and observed global distribution and frequency of lightning activity is reasonable (Fig. S2). In particular we note that also the observations over South Asia show stronger lightning activity during spring than during the monsoon season. The observed maximum of lightning activity over the coastal areas of Western Bengal and Bangladesh in April also shows up in the simulation.

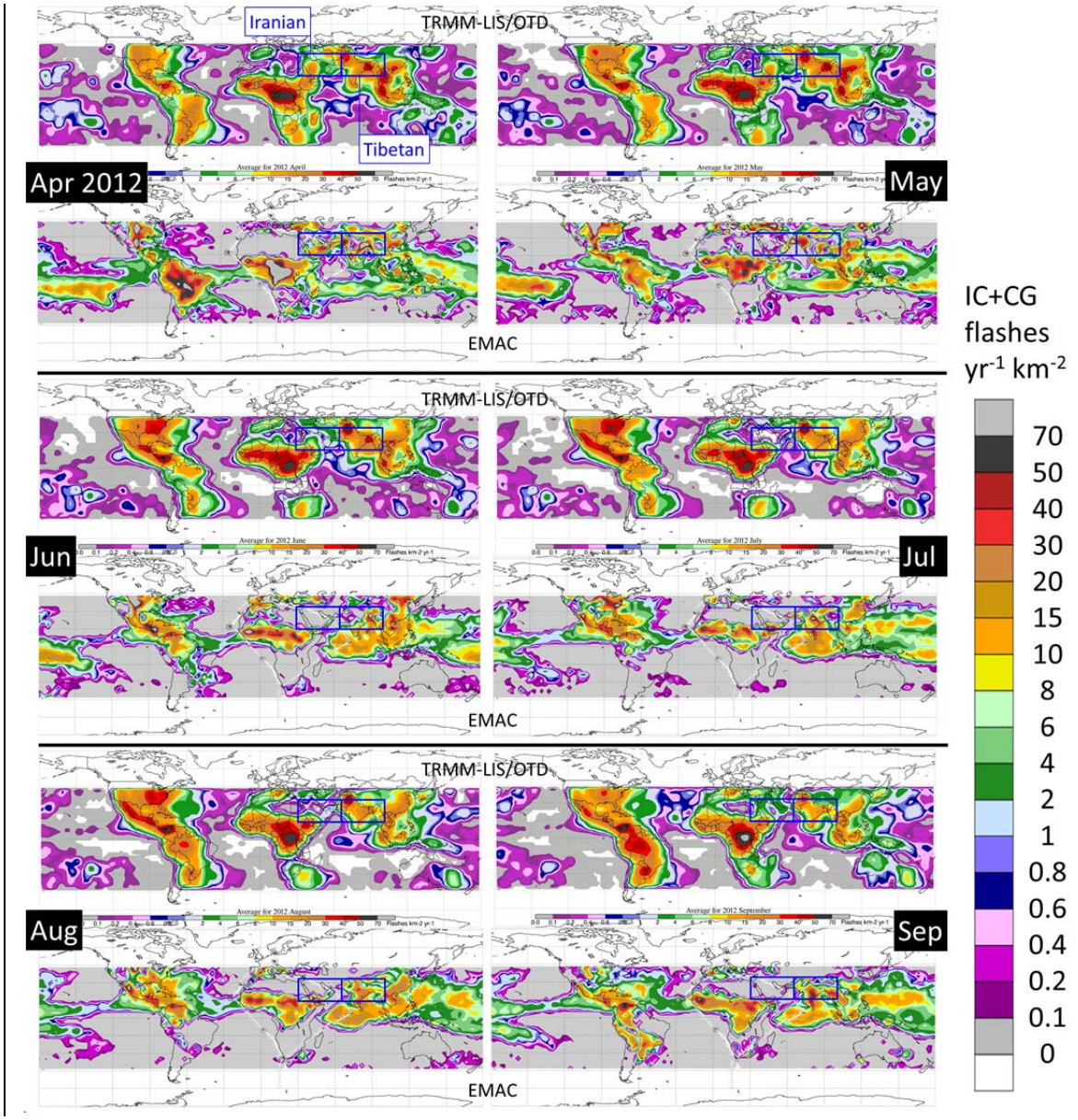
Iranian
Tibetan
TRMM-LIS/OTD
Apr 2012
May
EMAC
TRMM-LIS/OTD
Jun
Jul
EMAC
TRMM-LIS/OTD
Aug
Sep
EMAC
IC+CG
flashes
yr-1 km-2
70
50
40
30
20
15
10
8
6
4
2
1
0.8
0.6
0.4
0.2
0.1
0

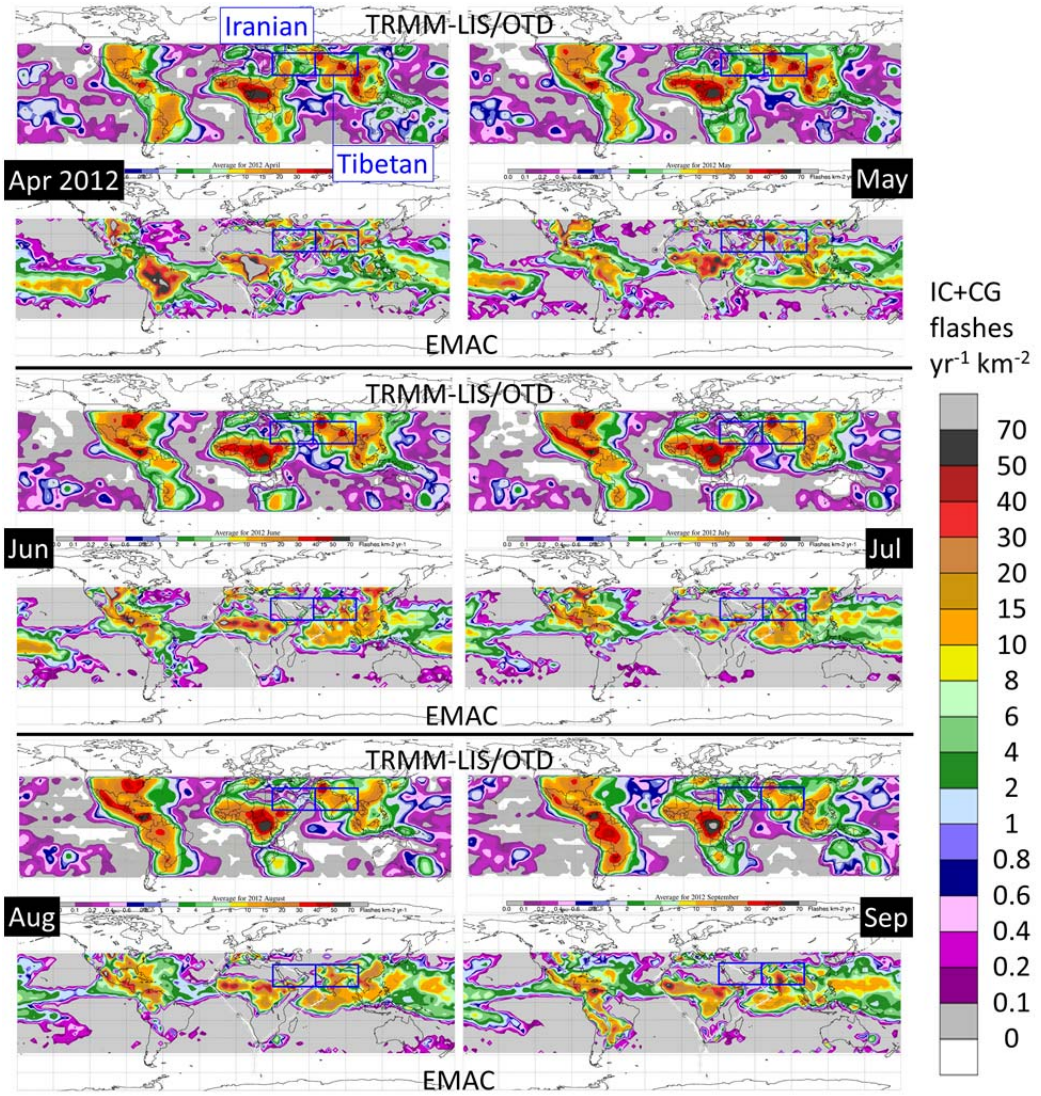

Figure S2. EMAC-simulated monthly mean lightning activity (intra-cloud + cloud-to-ground flash frequency) compared to the corresponding TRMM-LIS/OTD observations (Cecil, 2006). Data coverage and color scale are determined by the observations. Simulated lightning appears to be more localized, and thus exceeds the scale more often.

~~Convection is not explicitly resolved in the simulation, and the parameterizations for convection and lightning both introduce uncertainties to the simulation results for lightning. Uncertainties in the observations are due to a space- and time-dependent detection limit of 69% to 88%, and the application of a 3-month smoothing. Considering those uncertainties, the match between simulated and observed global distribution and frequency of lightning activity is reasonable.~~

S2.2 Comparison of simulated NO and NO_y to IAGOS-CARIBIC observations

As noted in section 2, we compare simulated NO and NO_y to the corresponding IAGOS-CARIBIC observations (Fig. S3). Commercial airliners do not fly as high as HALO and the tracks hardly reach the southern ASMA fringe, but the northern ASMA edge and the center of the monsoon region have been sampled multiple times. We evaluated all 345 IAGOS-CARIBIC flights between 19 May 2005 and 9 April 2014, considering the respective latest data versions as of 10 November 2017. In total 86 flights between Frankfurt (IATA code: FRA) and Chennai (MAA) or Guangzhou (CAN) or Bangkok (BKK) transected the ASMA region. 32 of these flights provide NO data there, and 66 flights provide NO_y. Neglecting data below 300 hPa and subsampling to the time resolution of the simulation yields the numbers of comparable data that are given in Figs. S3bd. Given the above uncertainties related to the representation of $LiNO_x$ in the simulation, NO matches the corresponding IAGOS-CARIBIC observations surprisingly well (Fig. S3b). This holds also for the more robust (more data) global comparison (Fig. S3a). Increased $LiNO_x$ emissions in the ASMA region in spring are also consistent to IAGOS-CARIBIC, and the simulation might even slightly underestimate those emissions (Fig. S3b: MAM).

The simulation matches IAGOS-CARIBIC NO_y almost perfectly on the global scale (Fig. S3c), and only moderately overestimates it during summer in the ASMA region (Fig. S3d: JJA).

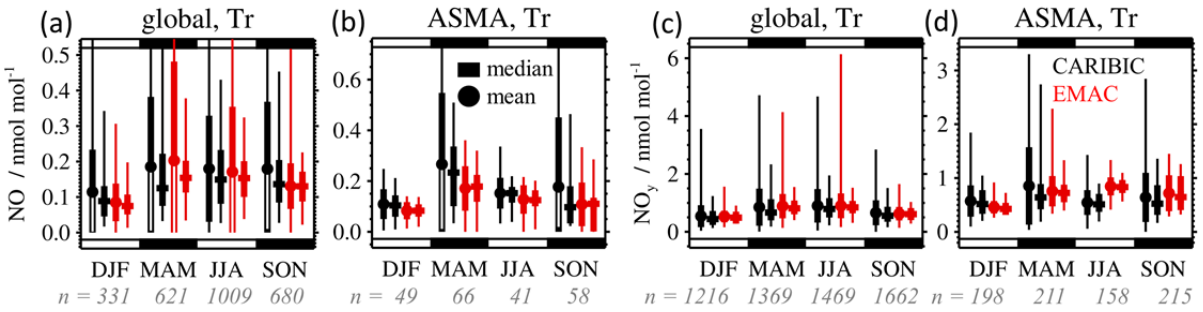

Figure S3. Comparison of IAGOS-CARIBIC (black) measurements in the altitude range between 300 hPa and the TP ("Tr") with corresponding results of the EMAC RC1SD-base-10a simulation (red) for (a) NO globally, (b) NO in the ASMA region (15-35°N, 30-100°E), (c) NO_y globally, (d) NO_y in the ASMA region. All data stem from the period May 2005 to April 2014. The simulation was sampled along the IAGOS-CARIBIC flight tracks with a resolution of 12 min, and IAGOS-CARIBIC observations were subsequently interpolated (interval mean) to a resolution of 12 min. Numbers n below the plots show the number of the remaining data pairs (after interpolation and filtering) available for the respective seasons. Dots represent mean values, whiskers indicate standard deviation, min & max values. Rectangles represent the median, and whiskers the percentiles 5, 25, 75, 95.

S3 Inter-annual variability

S3.1 Evolution of trace gas profiles in the Tibetan region 2010-2014

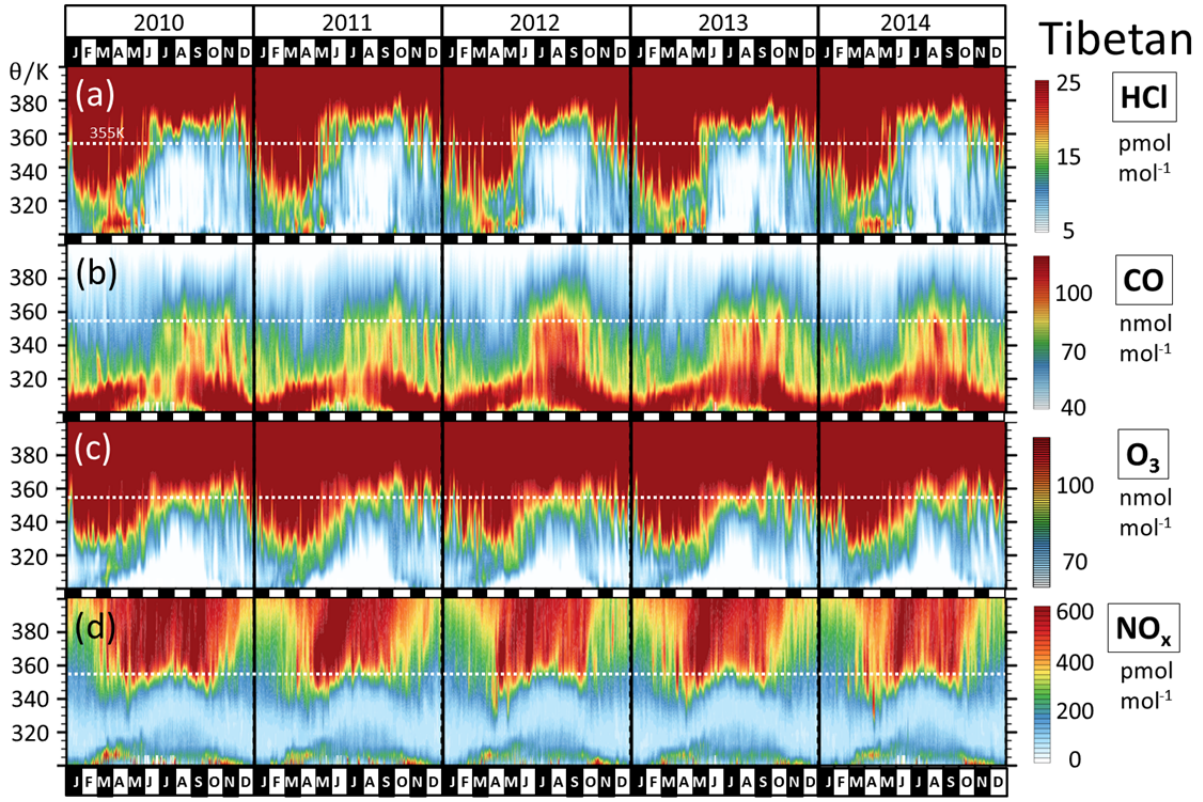

Figure S4. Evolution of simulated trace gas profiles and related diagnostics for the years 2010 - 2014 in the Tibetan ASMA region (15°N to 35°N , 65° - 100°E). Vertical coordinates are given as distance to the tropopause ("TP"), whose altitude depends on time and location. All values are grid-cell dry air mass weighted averages. The column for 2012 corresponds to **Figs. 5, 6, 7,** showing that the trace gas evolution in 2012 was largely similar to other years.

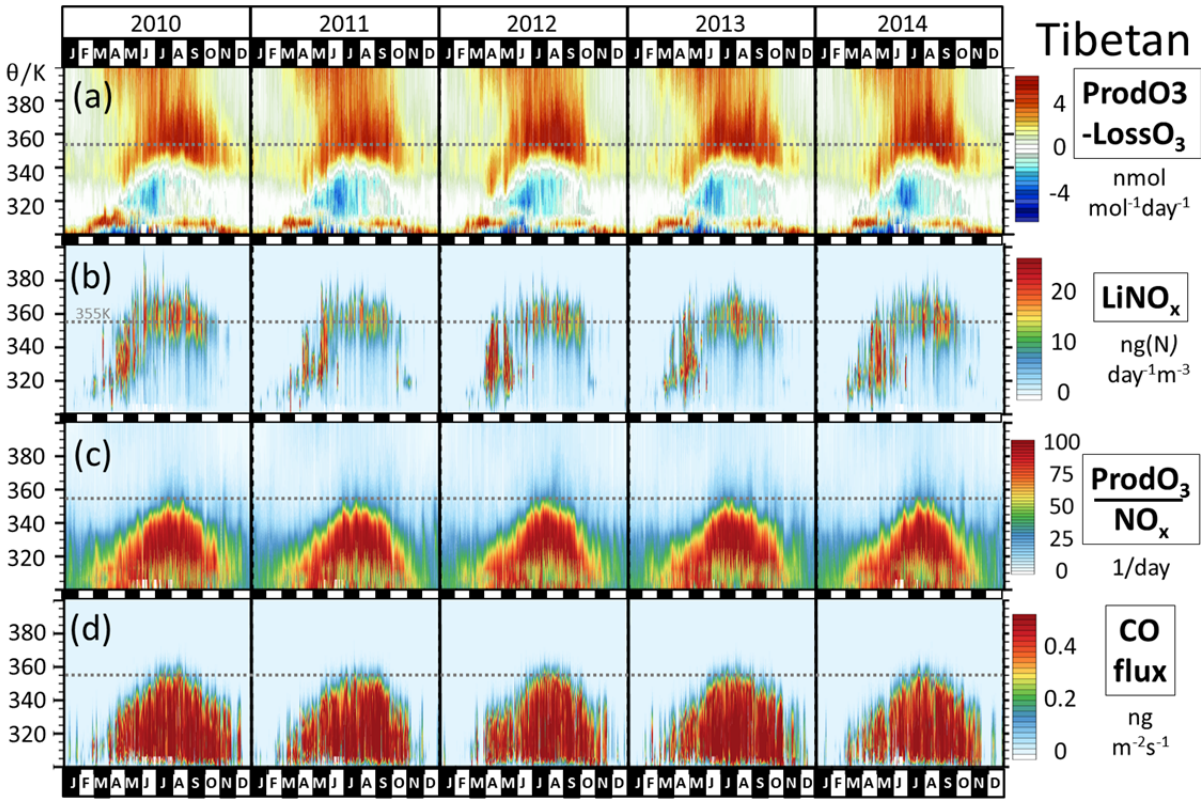

Figure S5. As Fig. S4, but putting Fig. 7 in a multi-annual perspective. Regarding the shown parameters, 2012 was a normal year.

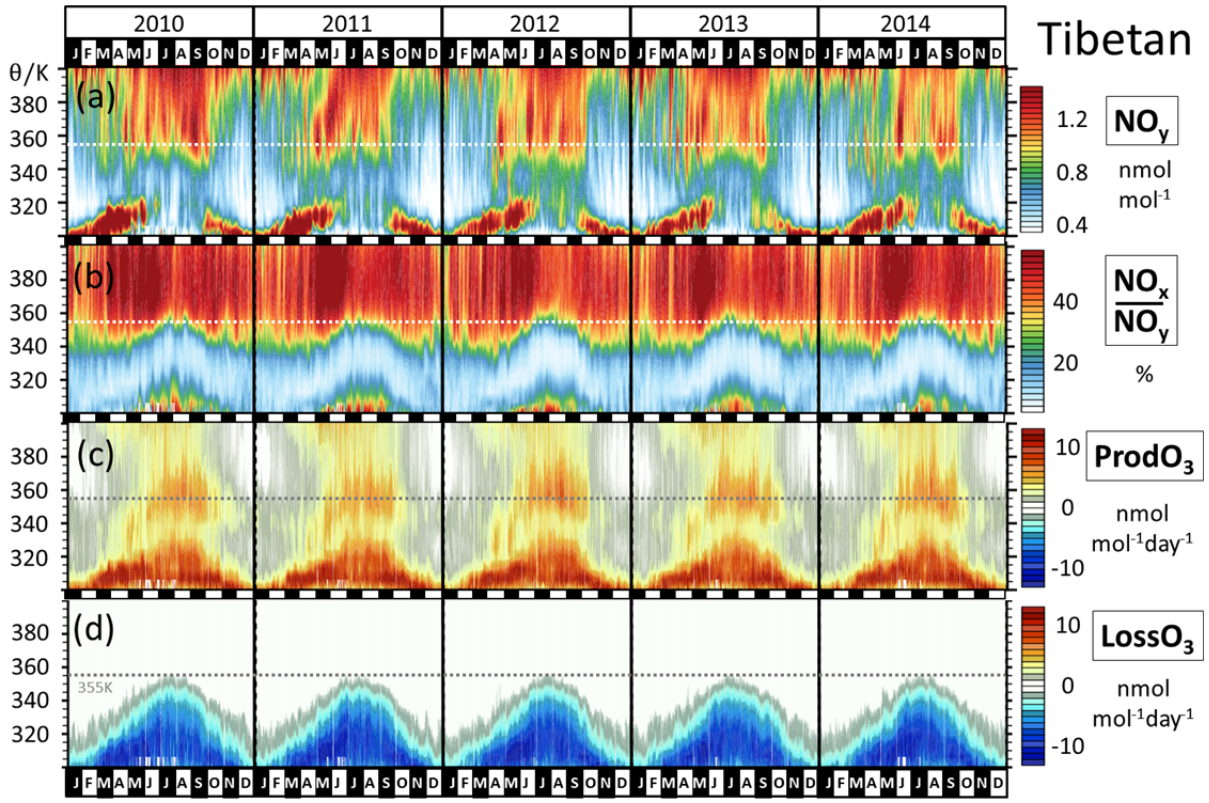

Figure S6. As Fig. S4, but putting Fig. 6 in a multi-annual perspective (Panels a and b). There is no noteworthy anomaly for 2012. Panels (c) and (d) show simulated photochemical O_3 production and destruction separately. LossO_3 is negligible at and above 355 K, thus the photochemical regime (NO_x-limited or NO_x–saturated) is determined mainly by ProdO_3.

S3.2 Evolution of trace gas profiles in the Iranian region 2010-2014

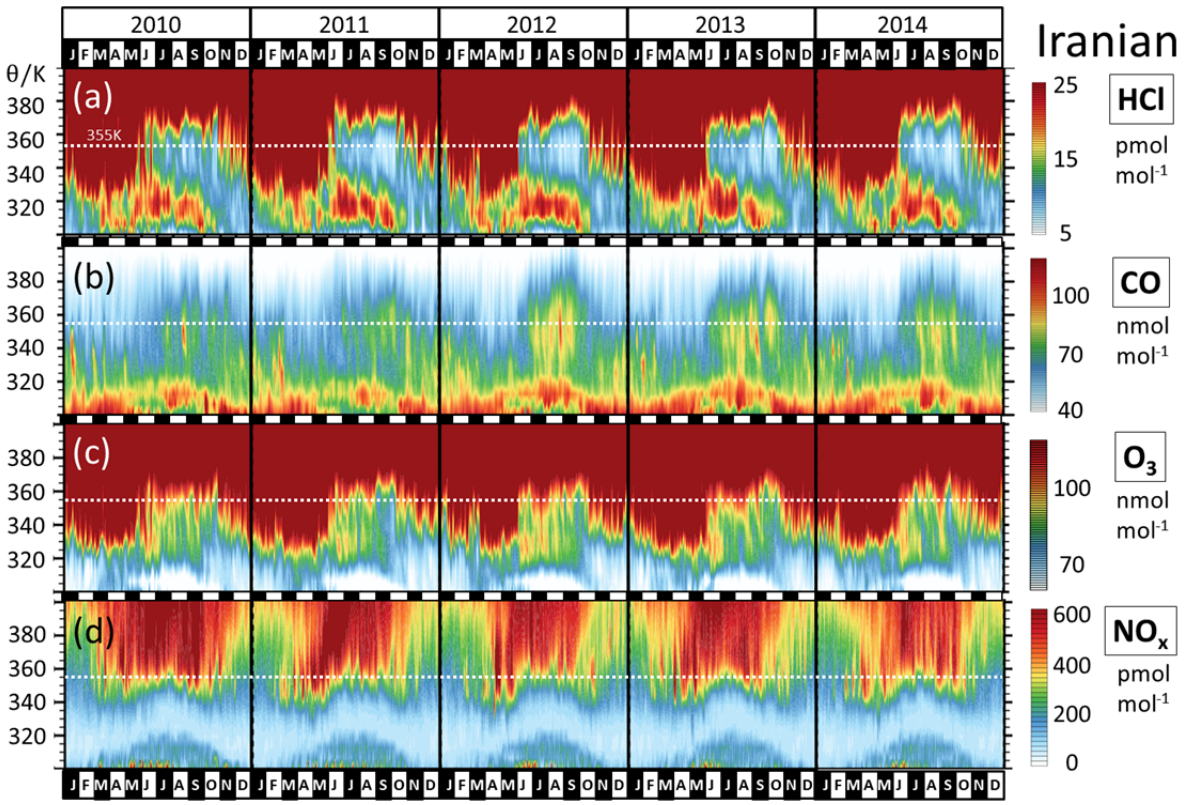

Figure S7. As Fig. S4, but for the Iranian ASMA region. Of the parameters shown, CO is the most variable one in the UTLS.

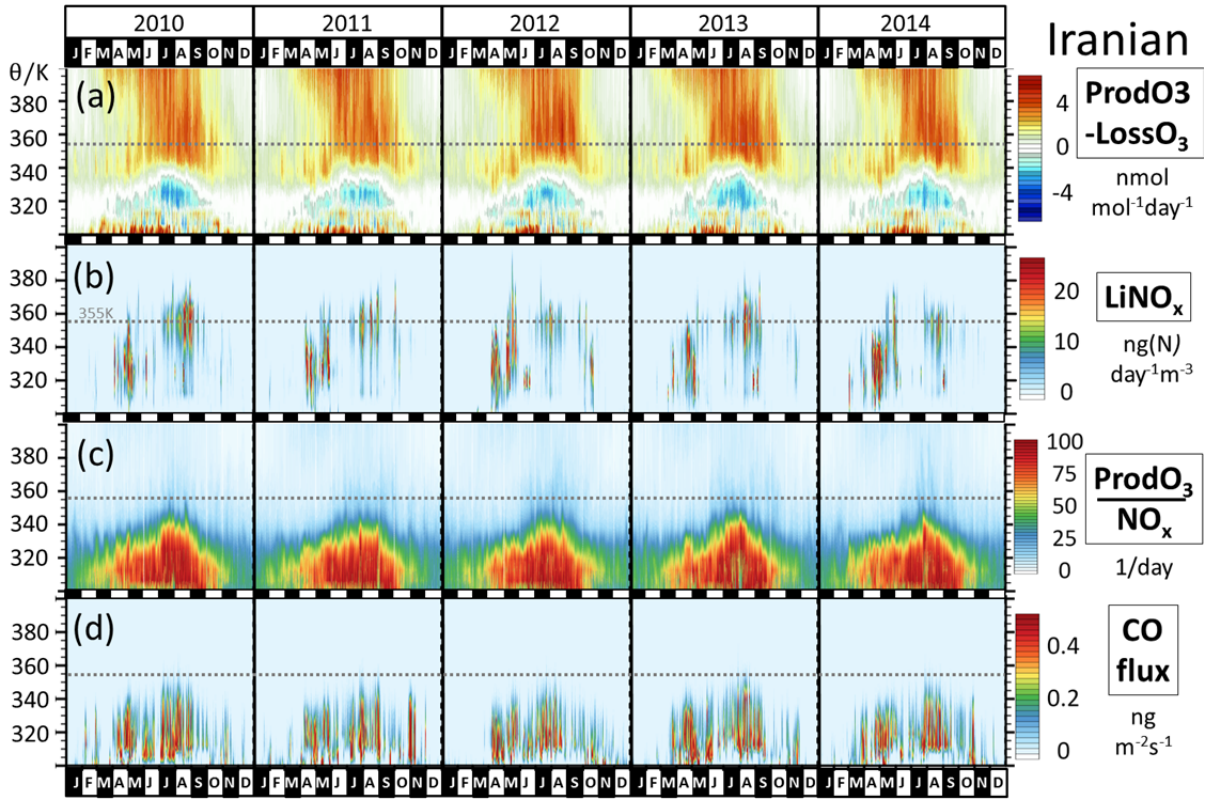

Figure S8. As Fig. S5, but for the Iranian region.

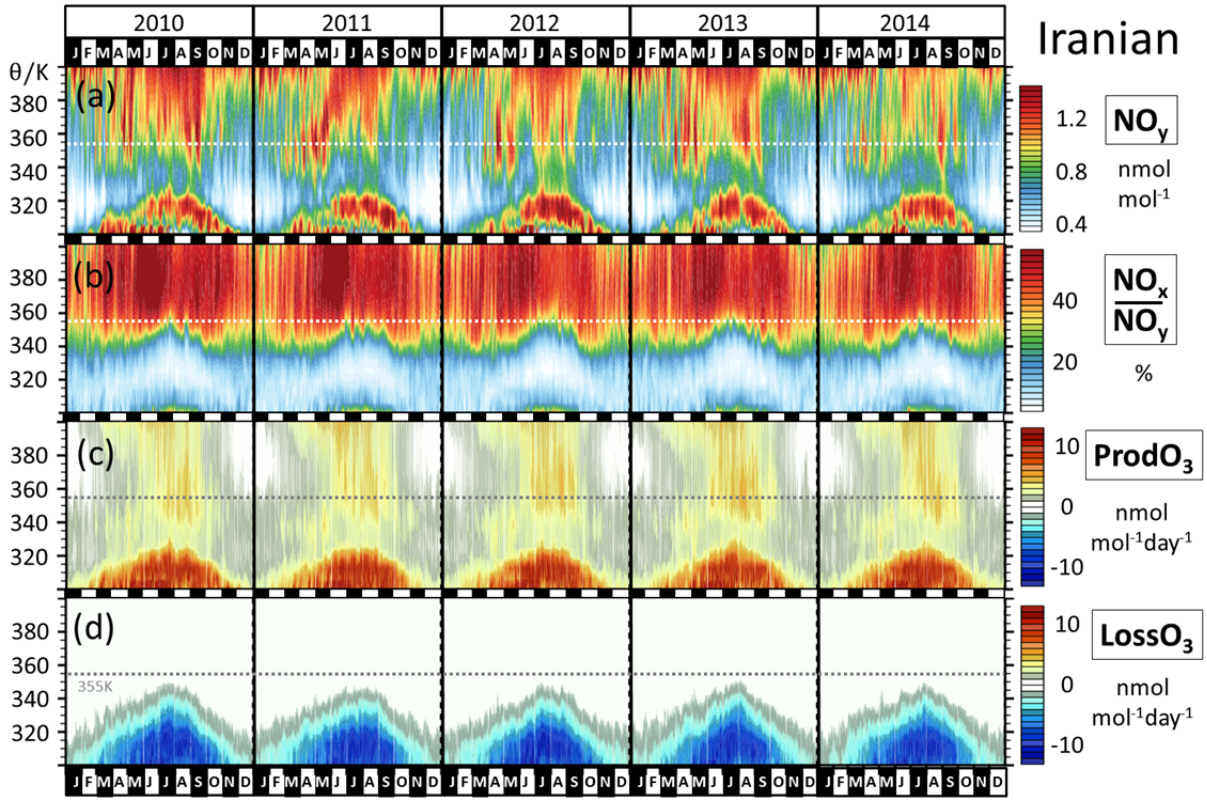

Figure S9. As Fig. S6, but for the Iranian region.

S3.3 TL entrainment 2010-2014

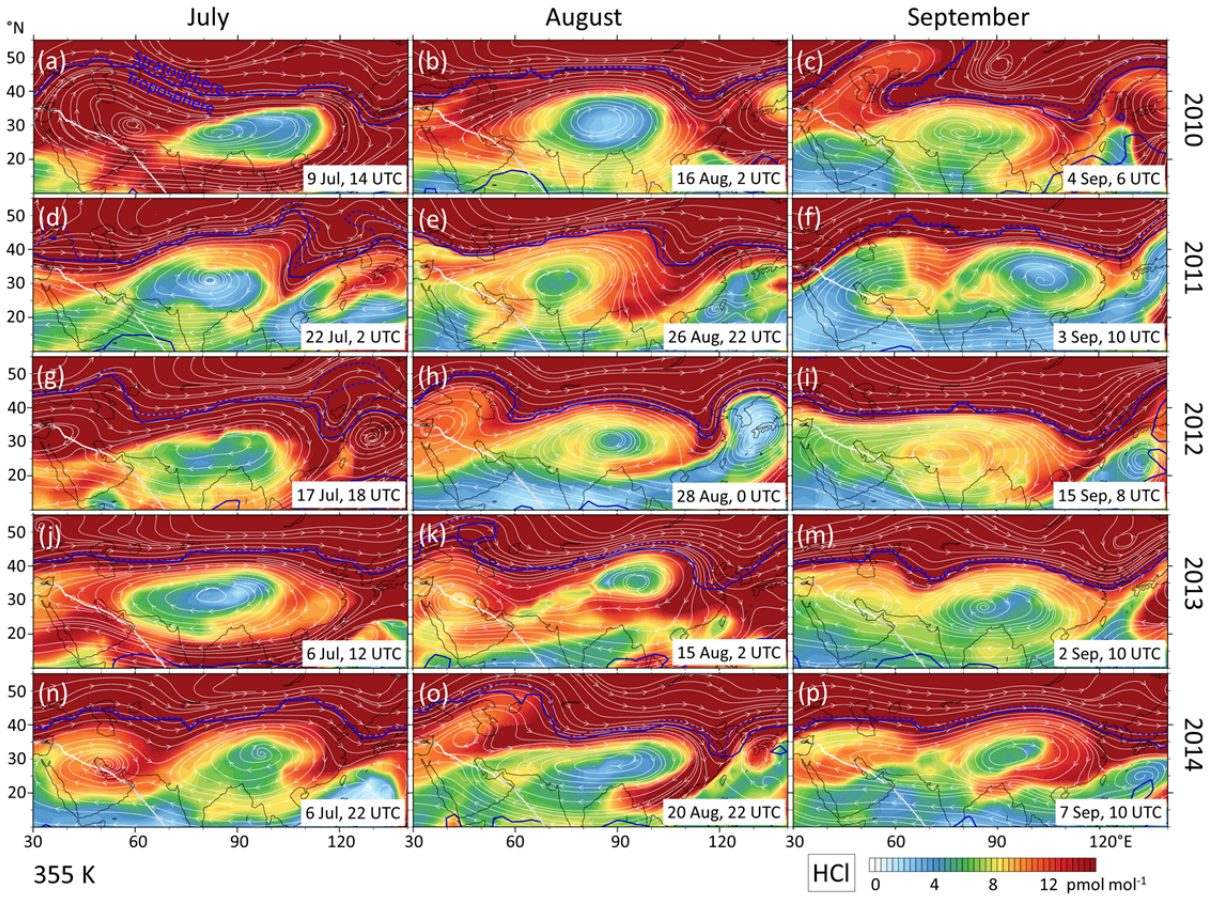

Figure S10. EMAC simulated HCl mixing ratios at 168 hPa in the ASMA region, complementing Fig. 3. The snapshots were selected to represent independent situations, where the southern ASMA fringe is marked by a filament of enhanced HCl. The filaments are often associated with a TP trough at the eastern ASMA flank. Enhanced HCl serves as a proxy for TL or stratospheric air.

S4 Trace gas profiles

S4.1. Simulated NO_y profiles

NO_y-profiles with maxima in the lower troposphere, in the UT and in the lower stratosphere dominate the Tibetan part (Fig. S11b). E-shaped NO_y-profiles in northern mid-latitudes (Grewe et al., 2001) were in part attributed to aviation NO_x emissions (Rogers et al., 2002), but aviation effects are much smaller in the tropics (Gottschaldt et al., 2013). Instead of aviation emissions, in situ production of lightning NO_x in the prevalent thunderstorms of the monsoon season increases NO_y in the UT over South Asia (Figs. 6d, 7d).

Photochemical production of HNO_3 and thus NO_y mixing ratios also increase with altitude above the tropopause (Seinfeld and Pandis, 2006). However, NO_y mixing ratios in the region between the tropopause and 15 hPa above the tropopause are often smaller than in the adjacent altitudes. There is little in situ production and not much transport from above or below. The maximum in the lower troposphere can be attributed to boundary layer pollution, but at about 400 hPa below the tropopause mostly non-solvable components (e.g. NO_x) are left.

Profiles in the Iranian ASMA part (Fig. 6c) have a different history of origins, and with just one minimum in the mid-troposphere are mostly C-shaped (Fig. S11a). During summer the Arabian Peninsula is dry. Deep convection (as indicated by lightning NO_x emissions in Fig. 7c) is mainly localised in the south-western Yemen region (Fig. 10), i.e. at the edge of the region we defined for calculating profiles of the Iranian part of the ASMA. Washing out is negligible throughout most of the Iranian region, and therefore NO_y can rise to about 400 hPa below the tropopause (circled in Fig. 6c).

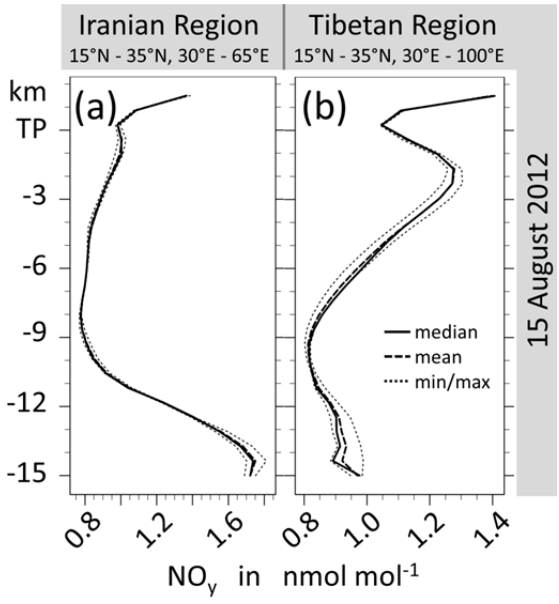

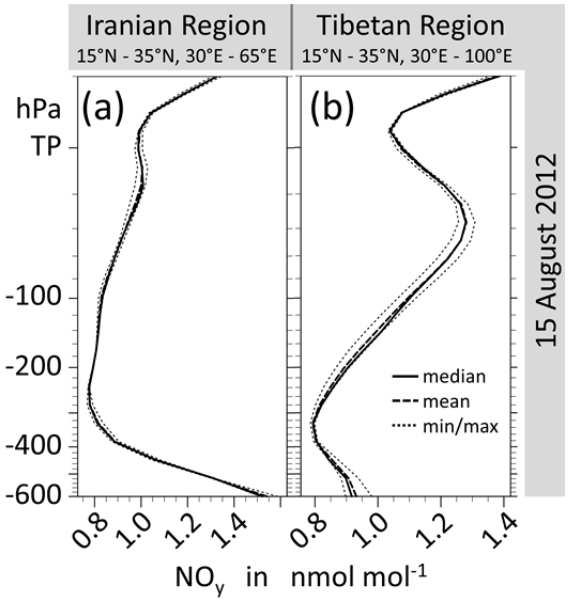

Figure S11. Simulated profiles of NO_y as simulated for 15 August 2012. These are examples of a C-shaped profile in the Iranian region (a) and an E-shaped profile in the Tibetan region (b).

S5 Processes

S5.1 Lightning NO_x sensitivity simulations

In order to link the $LiNO_x$ emissions to the NO_x burden in the ASMA region, a suite of EMAC sensitivity simulations with modified emission factors was conducted (Figs. S12, S13). All EMAC analyses in the main text are based on simulation RC1SD-base-10a (Jöckel et al., 2016), which is given in Fig. S12 just for comparison. The other simulations discussed in the context of Figs. S12 and S13 here are derived from EMAC simulation RC1SD-base-10, which differs in road traffic emissions and optical properties of stratospheric aerosol (Jöckel et al., 2016) from RC1SD-base-10a. Total $LiNO_x$ emissions in RC1SD-base-10 are 4.6 Tg(N) in 2012 (Jöckel et al., 2016), which is in the realistic range of 2 – 8 Tg(N) yr^{-1} (Schumann and Huntrieser, 2007). RC1SD-base-10 and our base simulation for the $LiNO_x$ sensitivity analysis (b01) are both operated in chemistry-climate model (CCM) mode, i.e. including interactive chemistry with feedback on dynamics. Simulation b01 differs only in the usage of daily (Kaiser et al., 2012) instead of monthly biomass burning emissions and 5 h instead of 10 h output intervals. Feedbacks from chemistry on dynamics in all quasi chemistry-transport model mode (QCTM) (Deckert et al., 2011) simulations are based on identical trace gas time series from b01. The same dynamics incl. convection is simulated in all QCTM simulations. Differences between a QCTM reference simulation (q01) and sensitivity simulations (s*) are thus exclusively due to chemical perturbations. All QCTM simulations cover June – September 2012, but the first 3 months were discarded for spin-up.

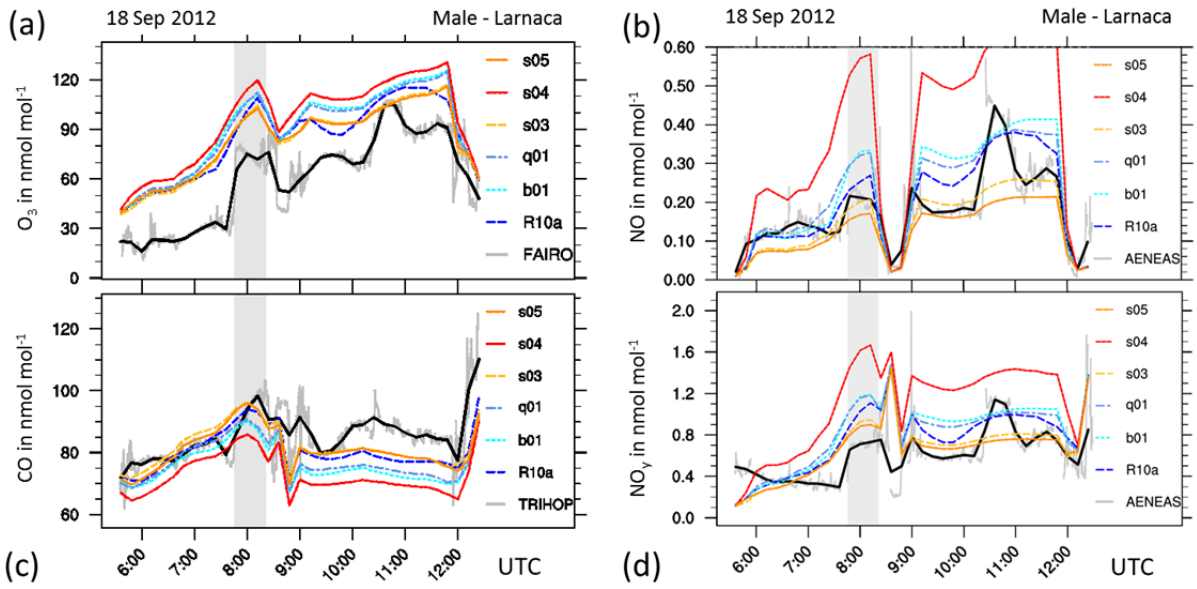

Figure S12. Mixing ratios of O_3, CO, NO and NO_y along the HALO flight track from Male to Larnaca, on 18 September 2012. Grey shading marks the first flight section in ASMA air. Grey line: in situ measurements in 10 s resolution, black: in situ averaged to 12 min simulation time steps, R10a: EMAC simulation RC1SD-base-10a. Sensitivity simulations are based on the almost identical RC1SD-base-10 simulation of (Jöckel et al., 2016), feature daily instead of monthly biomass burning emissions, and were performed in quasi chemistry transport model mode (Deckert et al., 2011) to facilitate isolating the effects of modified emissions.

b01: as R10a, but with different traffic and different biomass burning emissions; q01: as b01, but QCTM; s03: as q01, but halved $LiNO_x$ emissions; s04: as q01, but doubled $LiNO_x$ emissions; s05: as s03, but with a different vertical emission profile of $LiNO_x$ (emission factors not decreased in the mid-troposphere, i.e. no C-shape)

Figure S12 shows that RC1SD-base-10a captures observed O_3, CO, NO and NO_y along the HALO ESMVal flight path slightly better than b01 and q01. We are yet confident that the overall agreement is good enough for the analysis of chemical perturbations. For the QCTM sensitivity analyses it is more important to note that differences between b01 and q01 are negligible.

Figure S13k shows that halving $LiNO_x$ emission factors results in almost halved NO_x in the uppermost troposphere. Doubling of $LiNO_x$ emissions leads to almost doubled NO_x just below the tropopause (Fig. S13m). The biggest relative sensitivity in Fig. S13km almost coincides with the altitude range of the largest NO_x mixing ratios just below the tropopause (Fig. S13j). Thus, in our simulations $LiNO_x$ clearly dominates the NO_x budget from the tropopause to 100 hPa below it. The impact of LiNOx fades out at lower altitude, and almost vanishes at 400 hPa below the tropopause. This is consistent with the profiles of $LiNO_x$ emissions in September 2012, which mainly occur in the Tibetan part of the ASMA (Fig. 7d).

Modifications of NO_x print through on other O_3 precursors mainly via changes to the atmospheric oxidizing capacity (OH: Figs. S13ghi). In response to halved $LiNO_x$, OH decreases 200 hPa below the tropopause and lower, and increases above (Fig. S13h). The effects are reversed for doubled $LiNO_x$ (Fig. S13i). The largest relative effects coincide with largest absolute OH mixing ratios.

CO decreases throughout the shown altitude range for halved $LiNO_x$ (Fig. S13e). Without major production terms in the UT, modifications to CO mixing ratios are dominated by the loss reaction $CO + OH \rightarrow H + CO_2$. The rate coefficient of this reaction is proportional to pressure, and otherwise depends only on constants (supplement to Jöckel et al. (2016)). Laterally averaged CO mixing ratios vary little from 50 to 400 hPa below the tropopause (Fig. S13d), but are affected by decreased and increased OH (Figs. S13fg). Decreased OH in the lower half of the domain dominates the overall CO response. CO rises through this region with higher pressures before reaching the UT in the Tibetan part of the ASMA (Fig. 5d), which obviously outweighs the CO response to increased OH in the UT of Tibetan and Iranian part combined. Increased OH 200 – 500 hPa below the tropopause consequently leads to an overall decrease of CO in response to doubled $LiNO_x$ (Fig. S13f). The O_3 precursors NO_x and CO display opposite trends in response to $\Delta LiNO_x$.

Curiously, HCl shows the opposite response to modified $LiNO_x$ (Figs. S13abc). There is no chemical production of HCl in the UT, and the only loss term in the simulations is $HCl + OH \rightarrow Cl + H_2O$. The rate coefficient of this reaction is 1.7E-12 * EXP(-230/Temperature), see supplement to Jöckel et al. (2016). However, the tropospheric response of HCl to ΔOH is dominated rather by the vertical profile of HCl mixing ratios than by lower temperatures towards the tropopause. Almost all HCl in the UT is of stratospheric origin, and HCl mixing ratios steeply increase across the tropopause. Thus the UT response of HCl is dominated by ΔOH near the tropopause: increased OH for halved $LiNO_x$ increases HCl losses, and vice versa for doubled $LiNO_x$.

The response of UT net O_3 production to $\Delta LiNO_x$ (Figs. S13qrs) has mostly the same sign as ΔNO_x. As noted already in the context of Fig. 5 and Fig. 6, opposite gradients of O_3 precursors NO_x and CO in the UT lead to a broad altitude range of enhanced net O_3 production in the ASMA, centred about 100 hPa below the tropopause. O_3 production is limited by NO_x in lower altitudes and by CO (and other volatile organic compounds) towards the tropopause. NO_x and CO display opposite trends in response to $\Delta LiNO_x$, but relative changes to NO_x are larger and dominate the overall response of net O_3 production. We note, however, that the largest increase of

NO_x at the end of September (circled in Fig. S13m) decreases net O_3 production to zero or even net loss (circled in Fig. S13s), indicative of the NO_x-limited photochemical regime.

O_3 mixing ratios respond to $\Delta LiNO_x$ essentially like net O_3 production in the UT (Figs. S13nop). The altitude of maximum relative ΔO_3 is slightly lower than the altitude of maximum absolute changes to net O_3 production. We attribute this effect to upwards increasing absolute O_3 mixing ratios.

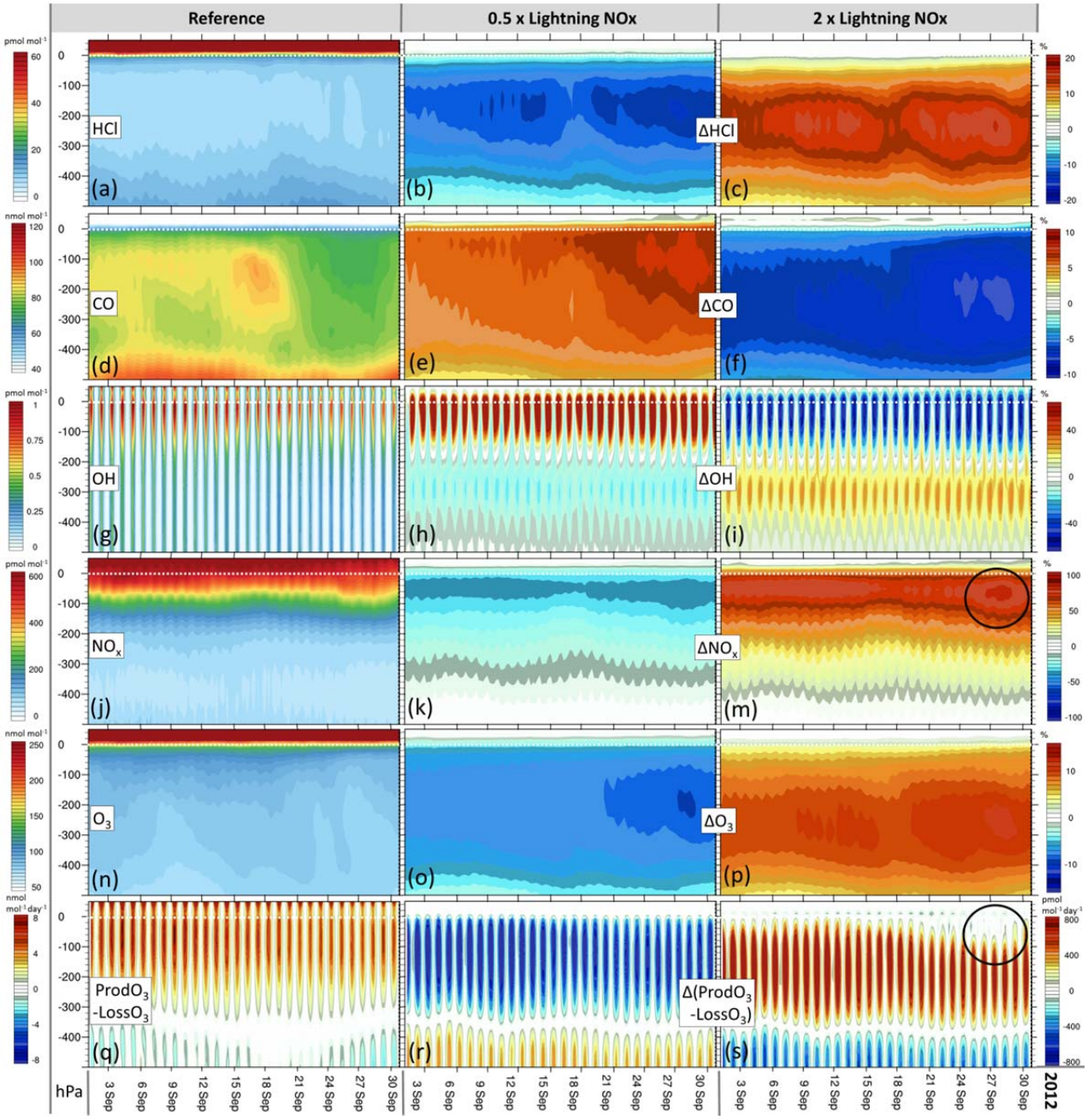

Figure S13. Evolution of simulated trace gas profiles and related diagnostics during September 2012 in the ASMA region (15° N – 35° N, 30° E – 100° E), and their sensitivity to $LiNO_x$ emissions. The vertical axes cover the UTLS and middle troposphere, and their coordinates are given as pressure distance to the tropopause. Left column: QCTM reference simulation (q01). Middle column: s03 – q01, relative deviation of sensitivity simulation s03 with respect to q01 for trace gases, absolute deviation for net O_3 production. Right column: s04 – q01.

S5.2 Entrainment of lower tropospheric air

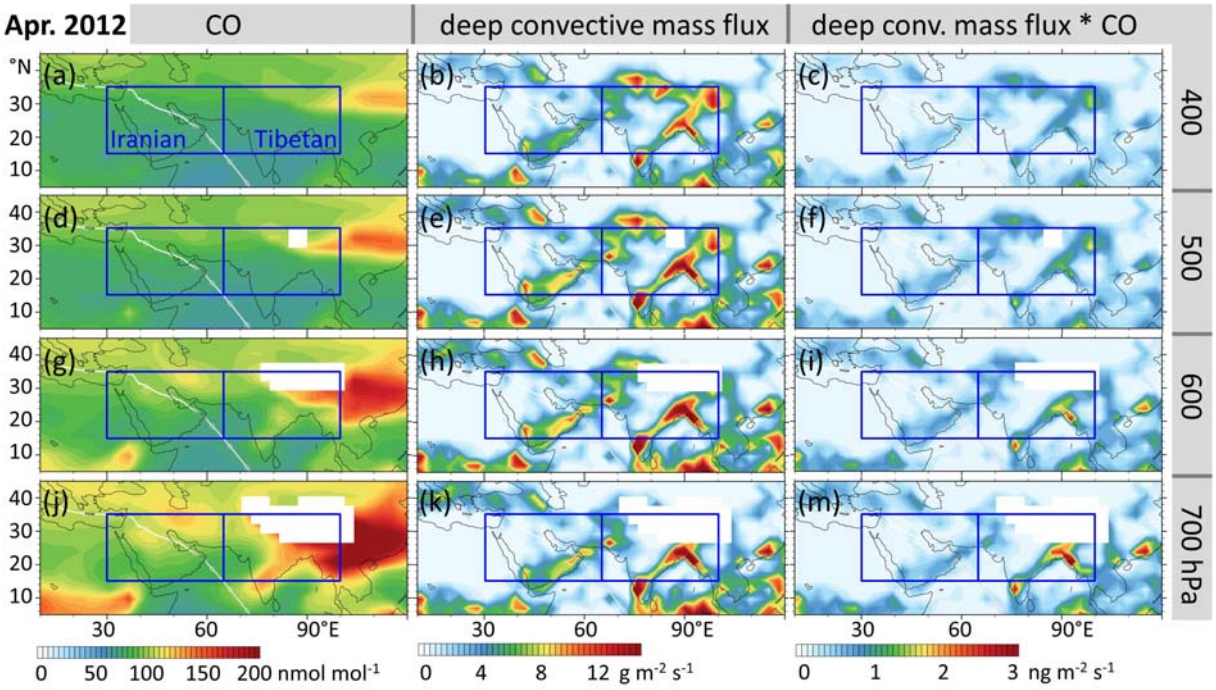

Figure S14. EMAC-simulated monthly mean distributions of CO (left) and deep convective mass flux (middle) in different pressure altitudes during spring (April 2012). The right column shows the deep convective mass flux of CO based on individual output steps. Blue rectangles mark the outline of the regions used to produce Figs. 5, 6, 7.

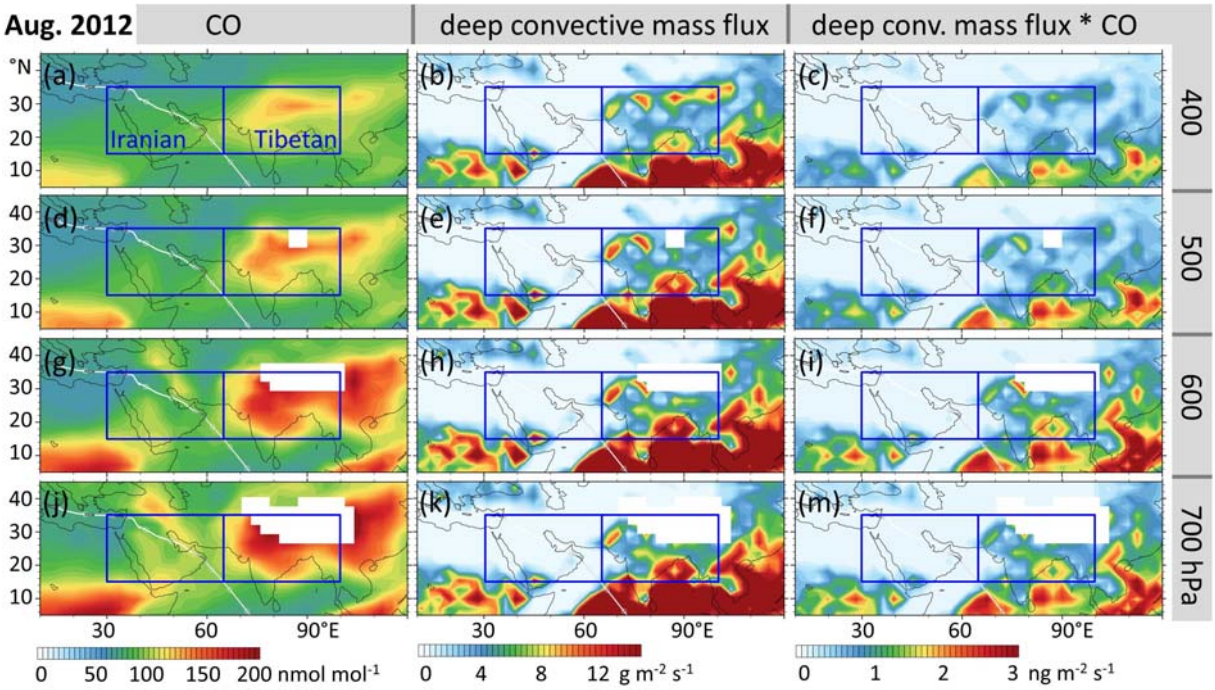

Figure S15. As Fig. S14, but for August 2012, i.e. during the monsoon season.

S5.3 Photochemical O_3 production

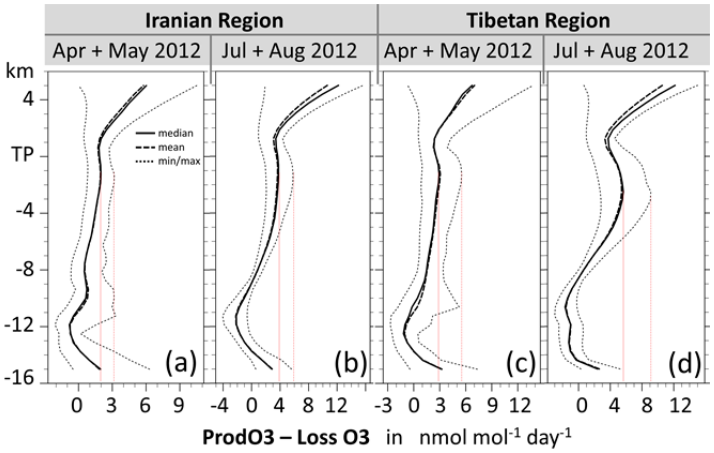

Figure S16. Simulated profiles of net O_3 production in the Tibetan region. Auxiliary red lines indicate the mean and maximum net O_3 production in the UT, which are both higher in summer than in spring.

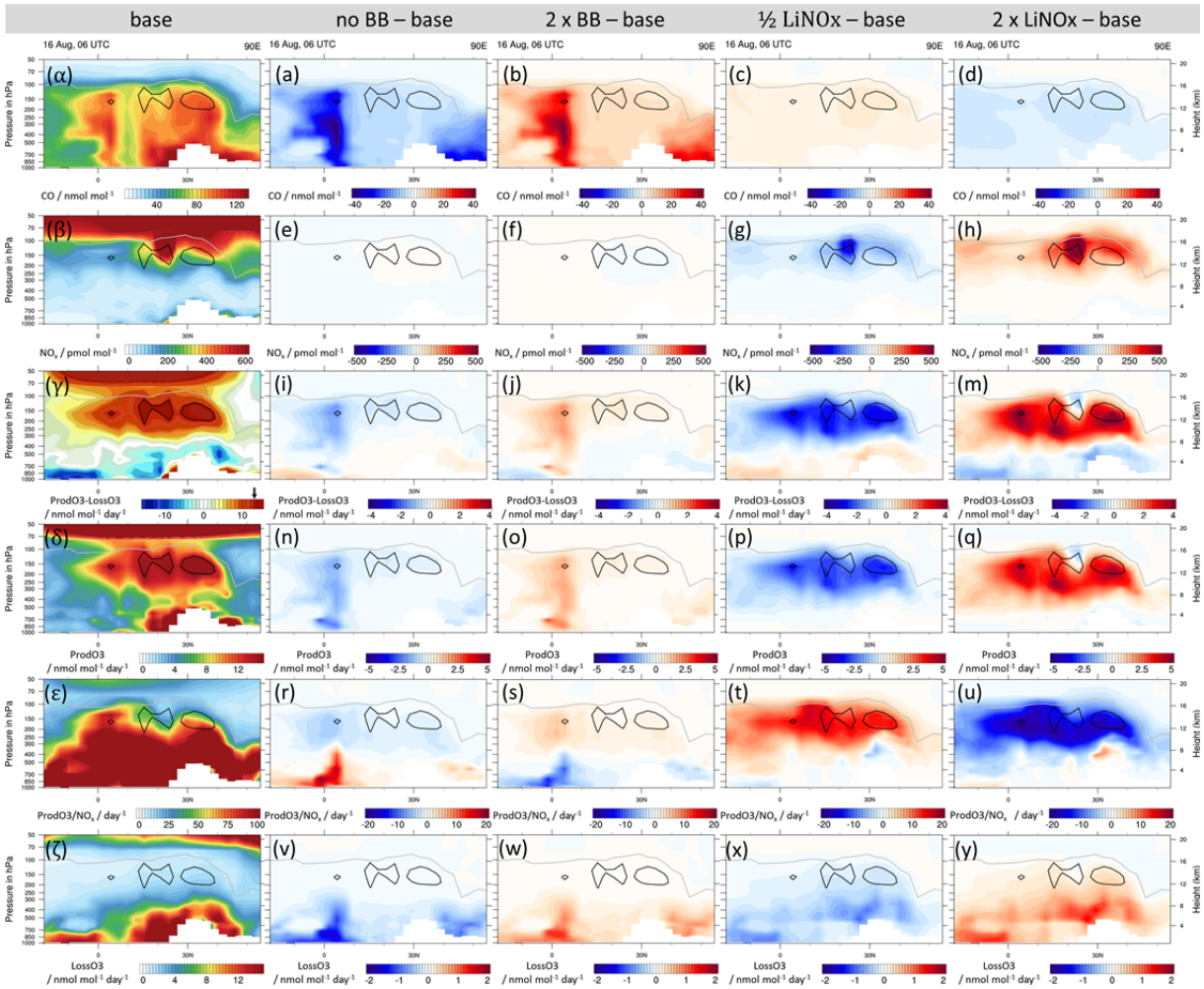

Figure S17. Selection of parameters related to photochemical O_3 production in a meridional curtain through the Tibetan part of the ASMA in a snapshot taken mid August 2012. The left column shows the results of the EMAC QCTM simulation that has been introduced in appendix A. The other columns show the difference of that reference to sensitivity simulations, which feature identical dynamics but differ in biomass burning (BB) and lightning NO_x (LiNOx) emissions. The black lines represent the 13 nmol mol^{-1} day^{-1} isocontour of net O_3 production (taken from panel γ), the grey line denotes the tropopause.

S5.4 Splitting-up and stirring

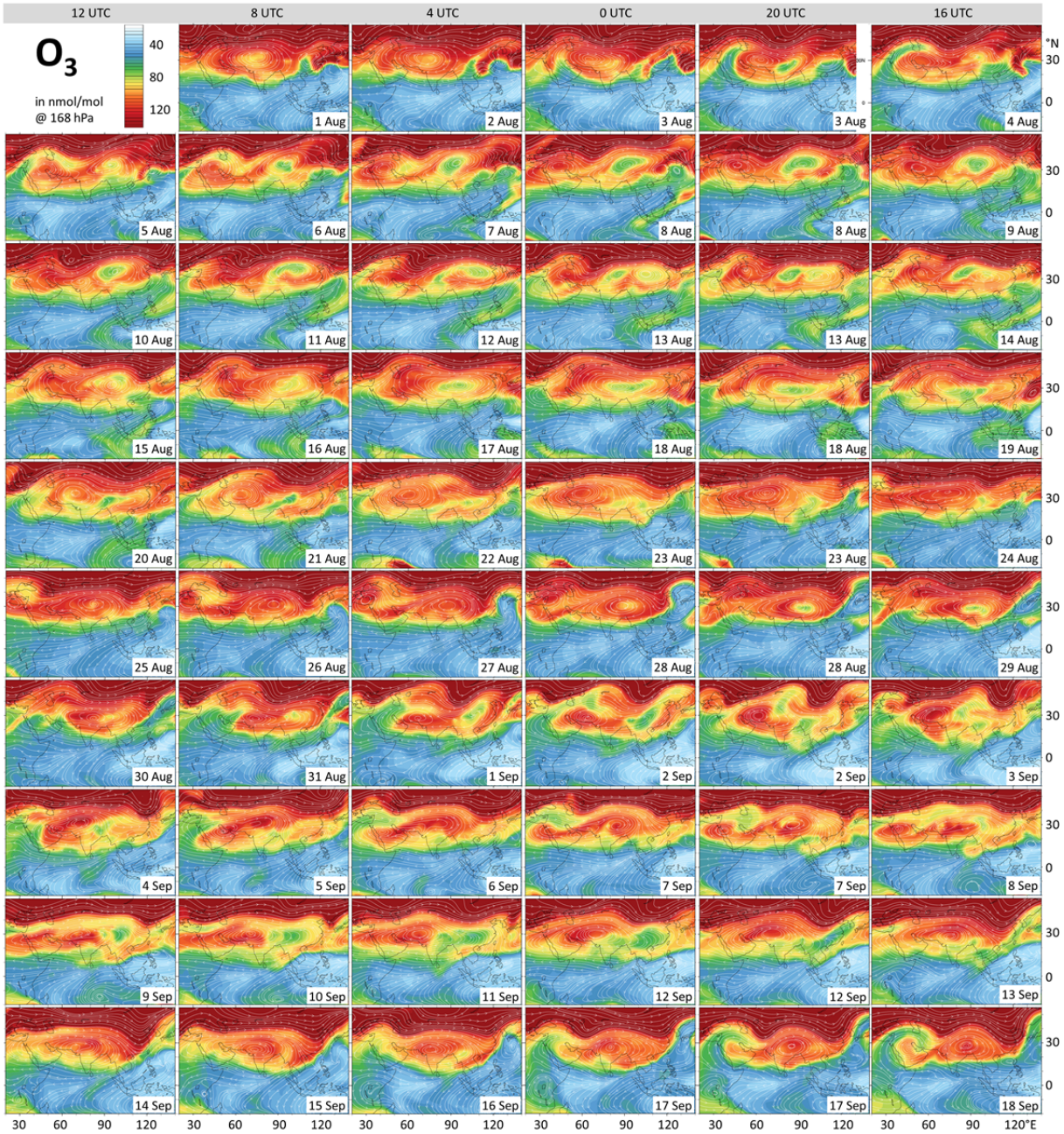

Figure S18. EMAC simulated O_3 mixing ratios and streamlines at 168 hPa in the ASMA region. The snapshots are 20 hours apart and cover the period from 1 August to 18 September 2012.

Larger fractions of the O_3-rich fringe were entrained during splitting up events. The sequence of snapshots (Fig. S18) covers almost half a monsoon season and episodic O_3-poor upwellings over the Tibetan plateau are smaller and shorter lived than O_3-rich regions at 168 hPa. This is consistent to the long-term average at a corresponding isentropic level (Fig. 1i).

References

Cecil, D. J.: LIS/OTD 2.5 Degree Low Resolution Monthly Climatology Time Series (LRMTS): Data set available online from the NASA Global Hydrology Resource Center DAAC, Huntsville, Alabama, U.S.A. doi: http://dx.doi.org/10.5067/LIS/LIS-OTD/DATA311, access: https://lightning.nsstc.nasa.gov/data/data_lis-otd-climatology.htm, 18. September 2017, 2006.

Deckert, R., Jöckel, P., Grewe, V., Gottschaldt, K., and Hoor, P.: A quasi chemistry-transport model mode for EMAC, Geoscientific Model Development, 4, 195-206, 10.5194/gmd-4-195-2011, 2011.

Gottschaldt, K., Voigt, C., Jöckel, P., Righi, M., Deckert, R., and Dietmüller, S.: Global sensitivity of aviation NOx effects to the HNO3-forming channel of the HO2 + NO reaction, Atmospheric Chemistry and Physics, 13, 3003-3025, 10.5194/acp-13-3003-2013, 2013.

Grewe, V., Brunner, D., Dameris, M., Grenfell, J. L., Hein, R., Shindell, D., and Staehelin, J.: Origin and variability of upper tropospheric nitrogen oxides and ozone at northern mid-latitudes, Atmospheric Environment, 35, 3421-3433, 2001.

Jöckel, P., Tost, H., Pozzer, A., Kunze, M., Kirner, O., Brenninkmeijer, C. A. M., Brinkop, S., Cai, D. S., Dyroff, C., Eckstein, J., Frank, F., Garny, H., Gottschaldt, K.-D., Graf, P., Grewe, V., Kerkweg, A., Kern, B., Matthes, S., Mertens, M., Meul, S., Neumaier, M., Nützel, M., Oberländer-Hayn, S., Ruhnke, R., Runde, T., Sander, R., Scharffe, D., and Zahn, A.: Earth System Chemistry integrated Modelling (ESCiMo) with the Modular Earth Submodel System (MESSy) version 2.51, Geoscientific Model Development, 9, 1153-1200, 10.5194/gmd-9-1153-2016, 2016.

Kaiser, J. W., Heil, A., Andreae, M. O., Benedetti, A., Chubarova, N., Jones, L., Morcrette, J. J., Razinger, M., Schultz, M. G., Suttie, M., and van der Werf, G. R.: Biomass burning emissions estimated with a global fire assimilation system based on observed fire radiative power, Biogeosciences, 9, 527-554, 10.5194/bg-9-527-2012, 2012.

Rogers, H., Teyssedre, H., Pitari, G., Grewe, V., van Velthoven, P., and Sundet, J.: Model intercomparison of the transport of aircraft-like emissions from sub- and supersonic aircraft, Meteorologische Zeitschrift, 11, 151-159, 10.1127/0941-2948/2002/0011-0151, 2002.

Schumann, U., and Huntrieser, H.: The global lightning-induced nitrogen oxides source, Atmos. Chem. Phys., 7, 3823-3907, 2007.

Seinfeld, J. H., and Pandis, S. N.: Atmospheric chemistry and physics : from air pollution to climate change, 2nd edition ed., John Wiley & Sons, Inc., Hoboken, New Jersey, 2006.

Vogel, B., Pan, L. L., Konopka, P., Günther, G., Müller, R., Hall, W., Campos, T., Pollack, I., Weinheimer, A., Wei, J., Atlas, E. L., and Bowman, K. P.: Transport pathways and signatures of mixing in the extratropical tropopause region derived from Lagrangian model simulations, Journal of Geophysical Research, 116, 10.1029/2010jd014876, 2011.

Zahn, A., Brenninkmeijer, C. A. M., Maiss, M., Scharffe, D. H., Crutzen, P. J., Hermann, M., Heintzenberg, J., Wiedensohler, A., Güsten, H., Heinrich, G., Fischer, H., Cuijpers, J. W. M., and van Velthoven, P. F. J.: Identification of extratropical two-way troposphere-stratosphere mixing based on CARIBIC measurements of O3, CO, and ultrafine particles, Journal of Geophysical Research: Atmospheres, 105, 1527-1535, 10.1029/1999jd900759, 2000.